



Measurements and Analysis of The Losses for Fabricated SOI Slot Waveguides

A Thesis

**Submitted to the Institute of Laser for Postgraduate
Studies, University of Baghdad in Partial Fulfillments
for the Requirements for the Degree of Doctor of
Philosophy in Laser / Electronics and Communication
Engineering**

By

Maithem Naeem Salih

B.Sc. Laser and Optoelectronics Engineering 2005

M.Sc. Laser and Optoelectronics Engineering 2009

Supervised by

Prof. Mazin M. Elias

1436 AH

2015 AD

Certification

I certify that this thesis was prepared under my supervision at the institute of laser for postgraduate studies, university of Baghdad as a partial requirement for the Degree of a Doctor of Philosophy in Laser / Electronics and Communication Engineering.

Signature 

Name: Dr. Mazin M. Elias

Title: Professor

Address: Institute of Laser for Postgraduate Studies,
University of Baghdad

Date: / / 2015

(Supervisor)

In view of an available recommendation, I forward this thesis for debate by the examination committee.

Signature: 

Name: Dr. Shelan Khasro Tawfeeq

Title: Asst. Professor


Address: Head of Scientific Committee


Institute of Laser for Postgraduate Studies,
University of Baghdad

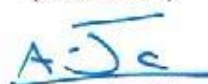
Date: 17/ 6/ 2015

Examination Committee Certificate


We certify that we have read this thesis "Measurements and analysis of the losses for fabricated SOI slot waveguides" and as examination committee we examined the student in its content and in our opinion it is adequate with standards as a thesis for the degree of Doctor of Philosophy in Laser \ Electronics and Communication Engineering


Signature 
Name: Dr. Abdul Hadi M. Al-Janabi
Title: Professor
Address: Institute of Laser for
Postgraduate Studies,
University of Baghdad
Date: / / 2015
(Chairman)

Signature 
Name: Dr. Raad Sami Fyath
Title: Professor
Address: College of Engineering,
University of Al-Nahrain
Date: 17 / 6 / 2015
(Member)


Signature 
Name: Dr. Adaweya J. Haider
Title: Professor
Address: Center of Nanotechnology,
University of Technology
Date: / / 2015
(Member)

Signature 
Name: Dr. Hussien A. Jawad
Title: Assistant Professor
Address: Institute of Laser for
Postgraduate Studies,
University of Baghdad
Date: / / 2015
(Member)

Signature 
Name: Dr. Shelan Khasro Tawfeeq
Title: Assistant Professor
Address: Institute of Laser for
Postgraduate Studies,
University of Baghdad
Date: 17 / 6 / 2015
(Member)

Signature 
Name: Dr. Mazin M. Elias
Title: Professor
Address: Institute of Laser for
Postgraduate Studies,
University of Baghdad
Date: / / 2015
(Supervisor)

Approved by the deanship of Institute of Laser for Postgraduate Studies, University of Baghdad,

Signature 
Name: Dr. Abdul Hadi M. Al-Janabi
Title: Dean of Institute of Laser for
Postgraduate Studies,
University of Baghdad
Date: 18 / 6 / 2015

Dedication

To my parents and family

Acknowledgement

I would like to express my deep gratitude to my supervisor, **Prof. Mazin M. Elias** for his valuable contribution, continuous help and encouragement during the research period. My thanks go to all the faculty members of Institute of Laser for Postgraduate Studies, University of Baghdad, especially to the Dean, **Prof. Abdul Hadi M. Al-Janabi**, and to **Dr. Hussein A. Jawad**, and **Prof. Khelil I. Hajim** for their valuable suggestions and advices. I acknowledge the supported research fellowship given to me from the Ministry of Higher Education and Scientific Research.

Special thanks to **Prof. Raad S. Fyath**, College of Engineering, Al-Nahrain University, **Dr. Shelan Kh. Tawfeeq**, Institute of Laser for Postgraduate Studies, and **Dr. Ziad A. Taha**, Head of the Engineering and Industrial Applications Dept. ILPS for their support during my research work.

I am indebted to The Guided Wave Optics Lab (GWOL), University of Colorado at Boulder, for their approval to register me as a visiting scholar. Especially, I would like to express my deep appreciation to **Prof. Alan Mickelson**, for the outstanding effort that he made to provide me with whatever was needed to finish this work; his support and guidance was extraordinary. I would like also to thank the other group members **Dr. Xi Chen**, **Keyon Janani**, **Eric Jacobson**, **Sarita Gautam**, **Aaron Trebing**, **Cristian Mendoza**, and **John Drumheller**; they were great colleagues.

I would like to extend my gratitude to all my friends and colleagues in the Institute of laser for postgraduate studies. Finally I am indebted to my family who were very patient and encouraging during all the period of my study.

Maithem

Abstract

An interesting silicon photonics component is the slot waveguide. The discontinuity of the normal component of the displacement vector can be used to affect guiding of the majority of the electric field energy in a narrow low index gap when the field is polarized parallel to the silicon surface, that is, perpendicular to the silicon confining walls. By infiltrating nonlinear material into such a gap, one can simultaneously confine electric and optical fields achieving a high efficient optical modulation or switching that is becoming more desirable on optical communication.

An array of 200 Silicon-on-Insulator (SOI) slot waveguide devices of varying slot widths, ribs widths, taper lengths and slot lengths are fabricated in each cell of a wafer fabricated at a commercial foundry. The cells are cleaved into individual chips after fabrication. Some chips are coated with thin films of polymers that fully infiltrated the slots. Measurements that consisted on spectral loss are made on the grating coupler waveguide devices of both coated and uncoated chips. Individual devices exhibited insertion losses varying from several dB up to values so great that the response is below the noise floor of the optical spectrum analyzer employed as a receiver. The chips that failed in the transmission test are primarily uncoated ones. Nominally identical devices on different chips exhibited nominally identical behavior.

A commercial software program is used to simulate each of the structures that is included in the 200 devices test. The simulations are seen to show a degree of qualitative agreement with the experimental results. Comparison of the experimental measurements and the simulation results indicates that the loss inherent in a slot waveguide is quite low. Near loss free couplers from ridges to slots are achievable in case of coated devices, whereas the situation is different in case of uncoated

devices where a lot of energy is dissipated through the substrate. Use of a surface roughness model indicates that the excess loss that slots exhibit with respect to a ridge mode counterpart arise almost solely from surface scattering off the surface roughness. The increased loss in the case of the slot guide arises from the higher electromagnetic energy density at the surface of the guide due to the electric field discontinuity that is employed as a guidance mechanism in slot modes in contradistinction to ridge modes that are index-guided.

Conclusions include some speculation as to the limits on the loss that can be achieved by variation the design of slot guides without any improvement in surface roughness over what is now available with fabrication in commercial foundries.

List of Contents

List of Contents	I
List of Symbols	IV
List of Abbreviations	VII
List of Figures	VIII
List of Tables	XII
Chapter One: Introduction	1
1.1 Overview	1
1.2 Silicon Photonics Waveguides	2
1.3 Slot Devices	3
1.4 Literature Survey	6
1.6 Aim of Work	11
Chapter Two: Theoretical Background of Optical Waveguiding and Coupling	12
2.1 Introduction	12
2.2 The Concepts of Electromagnetic Wave Theory	13
2.2.1 Maxwell's Equations	13
2.2.2 Wave Equations	15
2.2.3 Boundary Condition for Electromagnetic Waves	16
2.3 Basics of Optical Waveguides	17
2.3.1 The Basic Waveguide's Structure	17
2.3.2 Optical Propagating in Asymmetric Waveguides	19
2.3.3 The Cutoff Conditions	24
2.3.4 Polarization	24

2.3.5 Modes in a Three-Layer Slab Waveguide.....	26
2.3.6 The Confinement Factor	29
2.3.7 Waveguides Geometries	30
2.3.8 Silicon-on-Insulator (SOI) Waveguides.....	31
2.4 Slot Waveguides.....	32
2.4.1 Principle of The Operation	33
2.4.2 Analysis of The Operation	33
2.4.3 SOI Slot Waveguides	36
2.5 Propagation Losses in Optical Waveguides	38
I. Scattering Surface Loss	38
II. Absorption Loss	40
III. Radiation Loss	41
2.6 Waveguide Input and Output Couplers	42
2.6.1 Grating Couplers	43
2.6.2 The Taper Coupler	45
2.6.3 The Coupling Efficiency	48
Chapter Three: Practice and Simulation in Silicon-on-Insulator Slot Devices	50
3.1 Introduction.....	50
3.2 Structures Layouts.....	51
3.3 Fabrication	53
3.4 Measuring setup.....	54
3.5 De-embedding Measurements.....	58
3.5 Simulation method	60
3.5.1 Mode Solving.....	60
3.5.2 Optical wave propagation.....	63
Chapter Four: Measurements, Results, and Discussion	65

4.1 Introduction.....	65
4.2 Effects of The Coating Layer.....	66
4.3 Effects of The Slot Width	74
4.4 Effects of Si Rib Width.....	81
4.5 Effects of Taper Length.....	84
4.6 Conclusions.....	85
4.7 Suggestions for Future Works	86
References.....	88
Publications.....	96

List of Symbols

σ	<i>Amount of the surface roughness at sidewalls of ribs</i>
θ	<i>Angle of incidence</i>
$A, B, \text{ and } C$	<i>Arbitrary constants</i>
L_B	<i>Beat length</i>
$\Delta\alpha$	<i>Change in the absorption in semiconductors</i>
Γ	<i>Confinement factor</i>
Δn	<i>Contrast index</i>
η_{cm}	<i>Coupling mode efficiency</i>
$loss_{cm}$	<i>Coupling mode loss</i>
ω_c	<i>Cutoff radian frequency</i>
λ_c	<i>Cutoff wavelength</i>
$x, y, \text{ and } z$	<i>Directions</i>
a	<i>Distance from the center of the slot to the inner wall of ribs</i>
b	<i>Distance from the center of the slot to the outer wall of ribs</i>
n_{eff}	<i>Effective Index</i>
\mathbf{D}	<i>Electric displacement vector</i>
\mathbf{E}	<i>Electric field</i>
E_s	<i>Electric field at the sidewalls surface of the rib</i>
E_x	<i>Electric field, x-component</i>
E_y	<i>Electric field, y-component</i>
E_z	<i>Electric field, z-component</i>
ϵ_0	<i>Electric permittivity</i>
E	<i>Electron charge</i>
μ_e	<i>Electron mobility</i>
h	<i>Height of the rib waveguide</i>
μ_h	<i>Hole mobility</i>
n	<i>Index of refraction</i>
ρ	<i>Initial half width of the taper</i>

P_{in}	<i>Input power</i>
m and i	<i>Integer</i>
$\mathcal{L}_{grating}$	<i>Loss of a grating coupler</i>
\mathcal{L}_{ridge}	<i>Loss of a ridge device</i>
\mathcal{L}_{slot}	<i>Loss of a slot device</i>
\mathbf{H}	<i>Magnetic field</i>
H_x	<i>Magnetic field, x-component</i>
H_y	<i>Magnetic field, y-component</i>
H_z	<i>Magnetic field, z-component</i>
\mathbf{B}	<i>Magnetic flux density</i>
μ_0	<i>Magnetic permeability</i>
\mathbf{M}	<i>Magnetization density</i>
λ	<i>Operating wavelength</i>
P'_{out}	<i>Output power of a ridge device</i>
P_{out}	<i>Output power of a slot device</i>
Λ	<i>Periodic distance between groves in grating coupler</i>
φ	<i>Phase shift</i>
\mathbf{P}	<i>Polarization density</i>
β	<i>Propagation constant</i>
ω	<i>Radian frequency</i>
K	<i>Radian periodic distance</i>
\mathbf{r}	<i>Radius vector</i>
μ_r	<i>Relative permeability</i>
ϵ_r	<i>Relative permittivity</i>
$\alpha_{scatt.}$	<i>Scattering attenuation coefficient</i>
$\mathcal{L}_{scattering}$	<i>Scattering loss</i>
α_{abs}	<i>Silicon absorption loss per centimeter</i>
L_s	<i>Slot length</i>
c	<i>Speed of light in vacuum</i>
Φ	<i>Taper angle</i>
L_T	<i>Taper length</i>
m_{cc}^*	<i>The effective mass of electrons</i>
m_{ch}^*	<i>The effective mass of holes</i>
N_e	<i>The free hole concentration</i>

d	<i>Thickness of the core</i>
t	<i>Time</i>
w_t	<i>Tip width</i>
γ_2	<i>Transverse propagation constant in the core</i>
K_H	<i>Transverse propagation constant in the rib waveguides</i>
γ_c	<i>Transverse propagation constant in the side cladding</i>
γ_s	<i>Transverse propagation constant in the slot</i>
γ_3	<i>Transverse propagation constant in the substrate</i>
γ_1	<i>Transverse propagation constant in the upper cladding</i>
k_o	<i>Wave number in vacuum</i>
λ_{eff}	<i>Wavelength in the waveguide</i>
λ_o	<i>Wavelength in vacuum</i>
w_r	<i>Width of the rib waveguide</i>
w_s	<i>Width of the slot</i>

List of Abbreviations

1D	One dimension
2D	Two dimensions
3D	Three dimensions
EM	Electromagnetic
EME	Eigen Mode Expansion
FEM	Finite Element Method
FMM	Finite Mode Matching
GWOL	Guided Wave Optics Lab
MMI	Multimode Interference
MMM	Mode Matching Method
MOS	Metal-Oxide-Semiconductor
OSA	Optical Spectrum Analyzer
PIC	Photonic Integrated Circuit
PI	Polyimide
SEM	Scanning Electron Microscopic
Si	Silicon
SiO ₂	Silicon dioxide
SLED	Super Luminescent light Emitting Diode
SMW	Strip-Multimode-Waveguide
SOI	Silicon-on-Insulator
TE	Transverse Electric
TM	Transverse Magnetic
UV	ultra-violet

List of Figures

Fig. no.	Fig. Title	Page
Fig. 1.1	SEM images of silicon photonics devices from GWOL (a) a grating coupler (b) a strip-slot taper coupler as a part of slot device, (c) one-to-all directional optical antenna, and (d) a ring filter.	3
Fig. 1.2	Layout of slot device (a) between strip waveguides (b) between single mode fibers.	4
Fig. 1.3	a) a grating coupler between fiber and strip waveguide (b) a strip-slot taper coupler.	5
Fig. 2.1	Boundary conditions at the interface between two dielectric media.	16
Fig. 2.2	Index profiles of an asymmetric (a) step-index planar waveguide and (b) graded-index planar waveguide..	18
Fig. 2.3	(a) A planar waveguide and (b) a rectangular waveguide.	19
Fig. 2.4	Modes of an asymmetric planar step-index waveguide.	22
Fig. 2.5	(a)TE field and (b) TM field of propagating light.	25
Fig. 2.6	Diagram of a planar waveguide structure.	26
Fig. 2.7	Cross-section image of different waveguide geometries.	31
Fig. 2.8	SOI planar waveguide.	32
Fig. 2.9	Schematic diagram of the slot waveguide geometry.	32
Fig. 2.10	The planar slot waveguide layout.	34
Fig. 2.11	(a)Schematic cross section of a silicon-on-insulator (SOI) slot waveguide(b) Dominant electric field component (E_y) of the fundamental TE mode field cross a slot waveguide.	37
Fig. 2.12	Various methods of coupling light from the fiber to waveguides.	43

Fig. 2.13	Light from a semi-vertical optical fiber is diffracted by a grating coupler into an optical waveguide.	43
Fig. 2.14	Operational principle of a grating coupler. (a) Phase fronts in real space and (b) k-vector diagram.	44
Fig. 2.15	A strip-slot waveguide taper coupler.	46
Fig. 2.16	E-field distribution (V/m) of the TE fundamental mode propagating through the SOI inverted taper.	48
Fig. 3.1	(a)The layout of the slot device from the input grating coupler to the output one and cross sections for the structure at different points (b) geometry of strip-slot taper coupler.	52
Fig. 3.2	The layout of the ridge device from the input grating coupler to the output one and cross sections for the structure at different points.	53
Fig. 3.3	SEM images for (a) a slot waveguide (b) a ridge waveguide (c) strip-slot taper coupling region (d) a tip of taper in face of a slot waveguide.	54
Fig. 3.4	Schematic of the in-house measurement setup.	55
Fig. 3.5	Image of experimental setup.	56
Fig. 3.7	An image of the experimental setup with more focus on the sample stage, coupling fibers, and monitor camera.	57
Fig. 3.8	Slot (up) and ridge (down) devices with their losses regions.	58
Fig. 3.9	The measured transmission of three ridge waveguide devices with cross section $0.45 \times 0.22 \mu\text{m}^2$ and ridge length $L_r = 1500$ (blue), 1900 (red), and 2400 μm (green).	59
Fig. 3.10	The electric field profile of (a) the fundamental quasi-TE mode (b) the fundamental quasi-TM mode across SOI slot waveguide with $w_s = 0.13 \mu\text{m}$, $h = 0.22 \mu\text{m}$, $w_r = 0.2 \mu\text{m}$ at 1550 nm.	61
Fig. 3.11	The electric field norm profile of a quasi-TE mode along a strip-slot coupling regions at 1550 nm wavelength.	62
Fig. 3.12	Electric field norm, of quasi-TE mode, distribution along width of the structure across strip-slot coupling regions at 1550 nm.	62

Fig. 3.13	Simulation of optical wave propagation through a strip-slot-strip coupler with different slot width w_s ; 0.13, 0.2, and 0.25 μm , at 1550 nm wavelength and TE polarization.	63,64
Fig. 4.1	The measured output optical power over 100 nm spectral width of coated (red), and uncoated (green), slot devices with 100 μm slot length, 0.12 μm slot width, and 0.12 μm each of Si ribs width.	67
Fig. 4.2	The simulated scattering losses (Dash), and coupling losses (Solid), for coated (red) and uncoated (blue) slot devices over 100 nm spectral width, 100 μm slot length, 0.12 μm slot width, and 0.12 μm each of Si ribs width.	68
Fig. 4.3	The normalized (a) transverse electric field component (b) electric field intensity of the quasi-TE fundamental mode, for coated (red) and uncoated (blue) slot devices with slot width, $w_s=0.12 \mu\text{m}$ and Si rib width, $w_r=0.12 \mu\text{m}$, at 1550 nm wavelength.	69
Fig. 4.4	The effective index of the quasi-TE fundamental mode vs. operation wavelength in slot waveguide with slot width, $w_s=0.2 \mu\text{m}$, Si rib width, $w_r=0.25 \mu\text{m}$ and thin film of polymer.	70
Fig. 4.5	The normalized magnetic field normal component of the quasi-TE fundamental mode, for coated (red) and uncoated (blue) slot devices with slot width, $w_s=0.12 \mu\text{m}$ and Si rib width, $w_r=0.12 \mu\text{m}$, at 1550 nm wavelength.	71
Fig. 4.6	The optical power intensity ($\text{W}/\mu\text{m}^2$) of quasi-TE mode, at 1550 nm wavelength, through a strip-slot taper coupler between a strip waveguide, $0.45 \times 0.22 \mu\text{m}^2$, and a slot waveguide, $0.22 \times (0.12 + 0.12 + 0.12) \mu\text{m}^2$, in both (a) coated, and (b) uncoated cases.	72
Fig. 4.7	The input and output optical power intensity distribution of the quasi-TE mode at 1550 nm wavelength along the width of (a) coated strip-slot coupler device, and (b) uncoated strip-slot coupler device.	73
Fig. 4.8	The measured output optical power of slot devices with different slot width, $w_s=0.13, 0.2$, and $0.25 \mu\text{m}$, with Si rib width, $w_r=0.2 \mu\text{m}$, slot length $L_s=1868 \mu\text{m}$ and taper length, $L_T=5 \mu\text{m}$, all slots are coated with 500 nm thickness of polymer ($n=1.7$). Also the measured output optical power of ridge waveguide $0.45 \times 0.22 \mu\text{m}^2$ and 1868 μm length.	74
Fig. 4.9	The measured de-embedded losses of the three slot devices in (4.8) and the simulated losses of these devices, which include;	75

	coupling loss and scattering loss, at 1550 nm wavelength.	
Fig. 4.10	The effective index of the quasi-TE fundamental mode vs. the slot width with Si rib width, $w_r=0.2\mu\text{m}$ at 1550 nm wavelength.	76
Fig. 4.11	(a)Electric field, transverse-component of the TE-quasi mode across coated slot waveguide with three different slot width, $w_s=0.13(\text{red})$, $0.2(\text{green})$, and $0.25\mu\text{m}(\text{blue})$, rib width $w_r=0.2\mu\text{m}$ and (b) intensity profiles.	77
Fig. 4.12	(a)Electric field, transverse-component of the TE-quasi mode across coated slot waveguide with three different slot width, $w_s=0.13(\text{red})$, $0.2(\text{green})$, and $0.25\mu\text{m}(\text{blue})$, rib width $w_r=0.2\mu\text{m}$ (b) magnetic field, normal-component, and (c) intensity profiles.	78,79
Fig. 4.13	The simulated strip-slot coupler structures with different slot width, w_s ; a) $0.25\mu\text{m}$, b) $0.2\mu\text{m}$, and c) $0.13\mu\text{m}$ with Si rib width, $w_r=0.2\mu\text{m}$ and taper length $L_T=5\mu\text{m}$, at 1550 nm wavelength and TE-polarization.	79,80
Fig. 4.14	Effective Index vs. Si rib width for three different slot width; 0.13 , 0.2 , and $0.25\mu\text{m}$. Electric field profile for quasi-TE mode at 1550 wavelength for three different rib width; 0.1 , 0.2 , and $0.3\mu\text{m}$ and slot width $0.13\mu\text{m}$.	82
Fig. 4.15	The measured output optical power of two coated slot devices with different rib widths; $w_r=0.2\mu\text{m}$ (green), and $0.13\mu\text{m}$ (red), slot width $w_s=0.2\mu\text{m}$, slot length $L_s=1854\mu\text{m}$, and height $h=0.22\mu\text{m}$.	83
Fig. 4.16	The confinement factor vs. Si rib width for three different slot width; 0.13 , 0.2 , and $0.25\mu\text{m}$. Electric field profile for quasi-TE mode at 1550 wavelength for three different rib width; 0.1 , 0.2 , and $0.3\mu\text{m}$ and slot width $0.13\mu\text{m}$.	84
Fig. 4.17	The transmission measurements of slot devices with three different taper length, L_T ; 5 , 10 , and $20\mu\text{m}$, and with different slot width, w_s ; 0.13 , 0.2 , and $0.25\mu\text{m}$. The simulated coupling loss (red line) of strip-slot taper coupler vs. taper length, all at wavelength 1550 nm and TE-polarization.	85

List of Tables

Table no.	Table Title	Page
Table 4.1	The measured output optical power, simulated coupling, and simulated scattering loss for coated and uncoated slot devices in Figs. 2.1 and 2, at 1550 nm wavelength.	68
Table 4.2	The measured de-embedded transmission and simulated coupling and scattering loss of the three slot devices in Fig. 4.9 with different slot width, at 1550 nm wavelength.	76

Chapter One:

Introduction

1.1 Overview

A lot of attempts seek to shrink photonic blocks building in order to realize massive integration as in electronics. The first and most important target that will close these attempts more toward the photonic integrated circuit (PIC) is the subwavelength light confinement [1]. A novel waveguide structure which was demonstrated in [2,3] and termed as a slot waveguide is considered recently as a promising solution for all optical systems in which processing (logic) functions work in tandem with interconnections to carry out processing without electrical conversion [4]. Slot waveguides property of high confining light in nanoscale region of low refractive index makes it as a primary block building for such systems, like; all-optical signal processing [5,6]. Furthermore, it could be proposed as interconnection element with ultra-low propagation loss [7]. For all these applications, the investigation of the total losses which are expected to be expired by a slot mode device is vital and important step in order to find the ability of this device to achieve the required functions. While the losses which arise from coupling into and from slot waveguide have been overcome by using the strip-slot taper coupler [8], other works were made to measure and find the propagation loss of the slot waveguide regardless the coupling approach. These measurements and attempts were

verified between high absorption material [9] or high absorption wavelength band [10]. The measuring , analyzing, and finding the effective factors of the losses, coupling and propagation, in slot waveguides become so necessary, whatever this slot waveguide is a guiding device or a functionalizing waveguide. The amount of these losses, their kinds, by what factors they can be affected, and the ways to overcome these losses will specify the conditions under which the slot device can be used as guiding device. Furthermore, these issues are very important to evaluate the nonlinear losses of the slot device in order to use it for nonlinear optics. In this work, the transmission of slot devices with different characteristics are measured and simulated. Several indications are deduced by comparing the experimental and simulation results, like; ultra-low inherent loss in any slot waveguide, a high coupling loss through a strip-slot taper coupler in uncoated case, and the influence of several parameters on the dominated scattering loss and the possibility of reducing this loss without improving the surface roughness of the sidewalls.

1.2 Silicon Photonics Waveguides

Fiber optics had made a high jump in communications technology, much as Kao and Hockham [11] had predicted before the first low loss fiber was fabricated at Corning in 1970 by Kapron, Keck and Maurer [12]. The low loss optical fiber is based on the concept of weak guidance, where the maximum change in the index of refraction (index contrast) between the core and cladding is kept small. The concept is that if the materials at the interface are similar in structure and lattice constant, the loss can be kept small. The converse that high index contrast is

accompanied by high propagation loss is not necessarily true. Silicon (Si) has a native oxide, namely, silicon dioxide SiO_2 . In diffusion of oxygen into a silicon lattice can, with minimal distortion to the lattice, form a similar material with greatly different optical properties. The index of refraction of Si, is roughly $n=3.45$ in near infrared and that of fused silica (one form of silicon dioxide), is $n=1.45$. The combination is strongly guiding in that the index change is 60% of the average whereas weakly guiding would require that the difference be significantly less than 10% of the mean [4]. The silicon-insulator combination was not originally low loss. In fact, the motivation behind the original silicon photonics work was ubiquity of silicon as an electronic material rather than its desirability as an optical material [13]. Soref's original work on wave guiding [13], electro-optic effect in silicon [14] and compendium of previous work [15] did stimulate further effort on rib waveguides [16] and devices [17]. Losses remained high [18,19] until the work of Vlasov who in 2004 demonstrated that smooth side walls could lead to loss of a few dB/cm [20], loss values comparable to other waveguiding technologies such as in diffused lithium niobate. With loss values under control, progress on devices progressed rapidly to include new types of waveguide [2,3,21,22], micro-rings [23], modulators [24], splitters [25], switches [26] and nonlinear devices [27]. Here some scanning electron microscope (SEM) micrographs of devices from Guided Wave Optic Lab (GWOL) have been included, as shown in Fig. 1.1.

1.3 Slot Devices

In general, the slot device consists of the slot waveguide itself, input and output coupler due to couple light between strip and slot waveguides. By this whole structure the slot device can be used as an int-

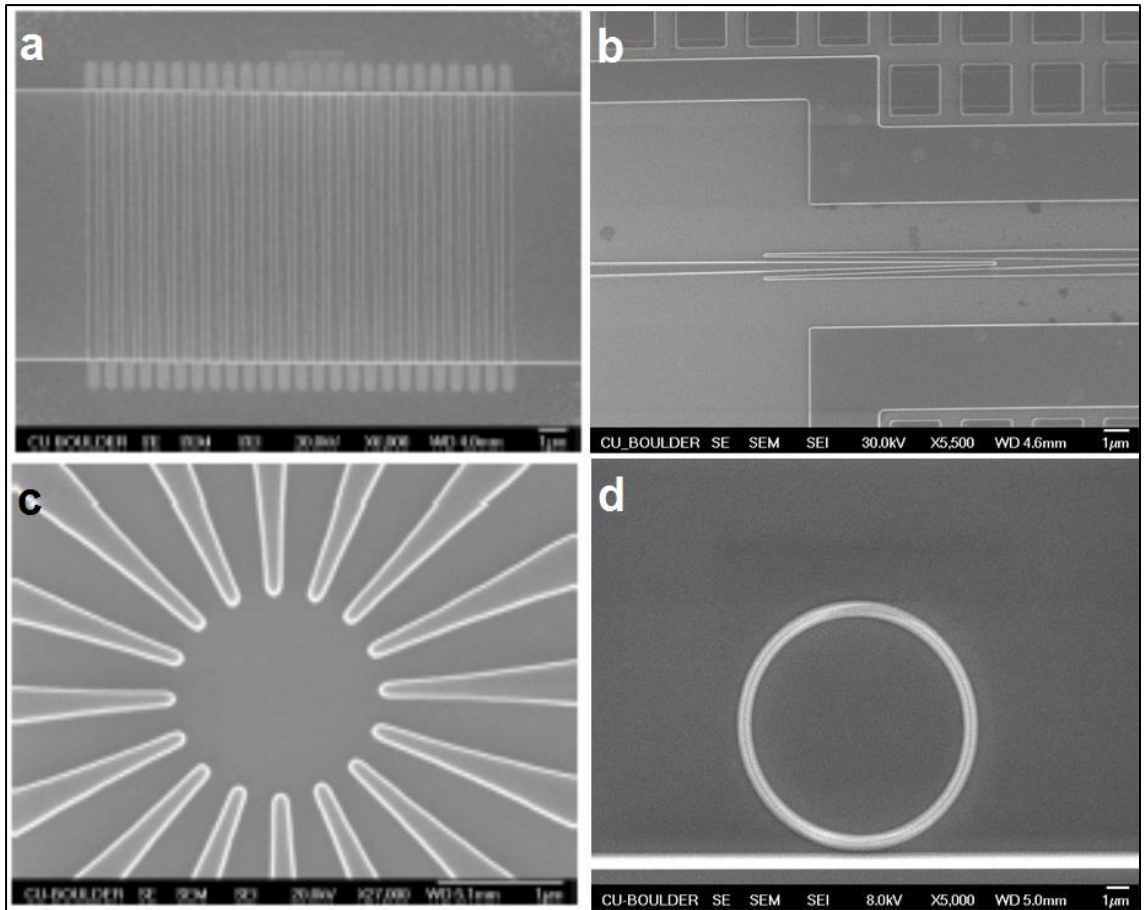


Fig. 1.1 SEM images of silicon photonics devices from GWOL (a) a grating coupler (b) a strip-slot taper coupler as a part of slot device, (c) one-to-all directional optical antenna, and (d) a ring filter [4].

erconnect element or functional device like; modulator or switch in an optical integrated circuit. In case of coupling light between a slot waveguide and a single-mode fiber, definitely, grating couplers and mode convertors are required, as shown in Fig. 1.2. While a grating coupler is used to couple light between single mode fiber and the integrated photonic circuit, the strip-slot trapper coupler [8] will be used here to couple light form and into a slot waveguide, as shown in Fig. 1.3. Although the high efficiency of this type of coupling [8, 28], some issues will be discussed in this work which may make the coupler efficiency at stake.

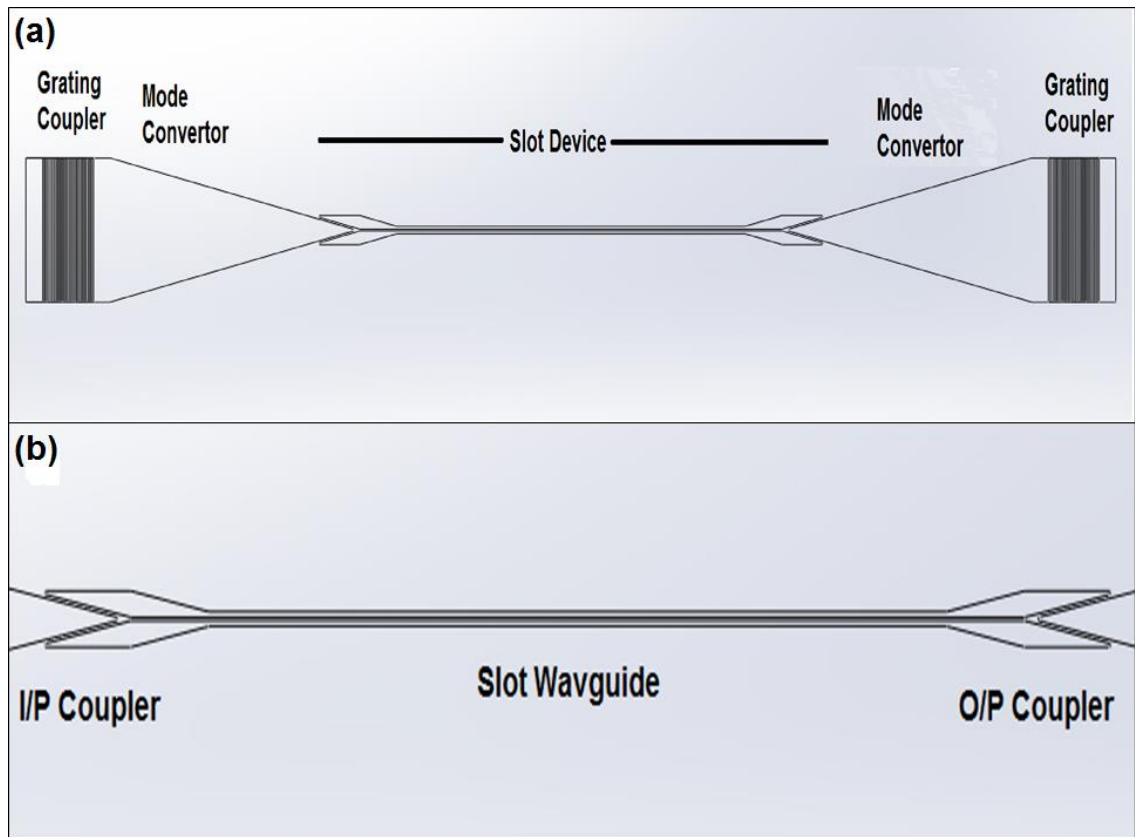


Fig. 1.2 Layout of slot device between (a) grating couplers (b) strip waveguides

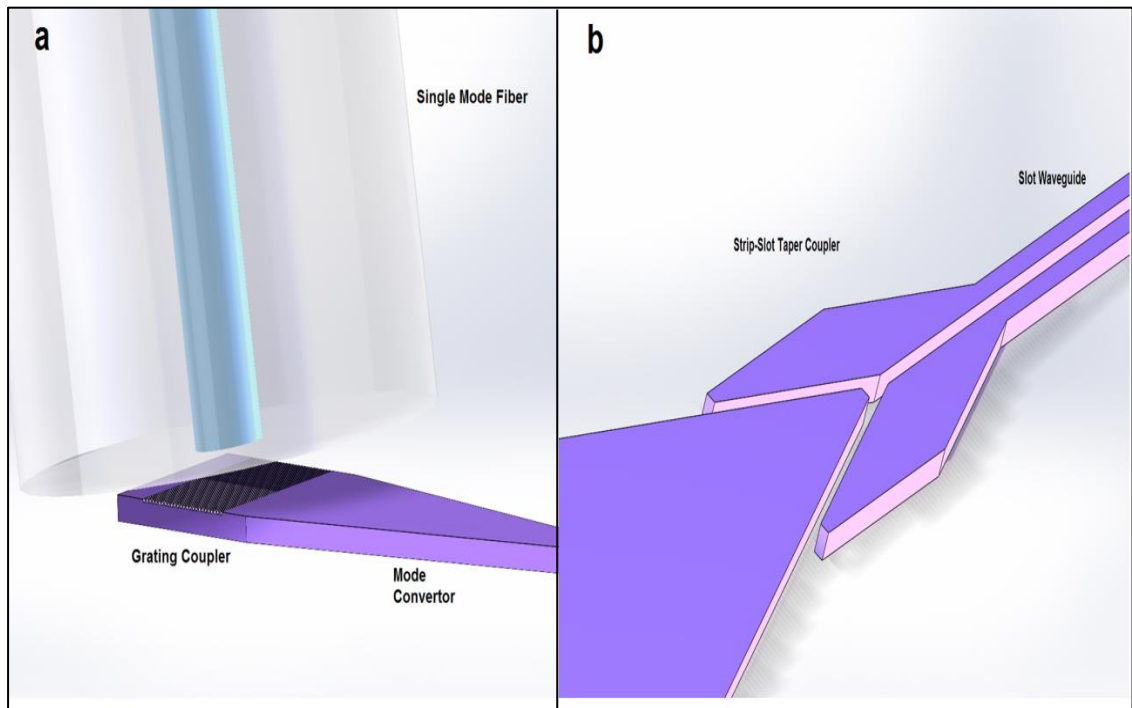


Fig. 1.3 (a) A grating coupler between a single-mode fiber and a strip waveguide (b) a strip-slot taper coupler.

1.4 Literature Survey

The slot waveguide was born in 2003 as an unexpected outcome of theoretical studies on metal-oxide-semiconductor (MOS) electro-optic modulation in high-confinement silicon photonic waveguides by V. de Almeida and C. Barrios. Theoretical analysis [2] and experimental demonstration [3] of the first slot-waveguide implemented in the Si/SiO₂, where SiO₂ is the silicon dioxide. Material system at 1.55 μm operation wavelength were reported by Cornell researchers in 2004. Since these pioneering works, several guided-wave configurations based on the slot-waveguide concept have been proposed and demonstrated. Relevant examples are the following:

In 2004 *Almeida et al.* [2] presented novel waveguide geometry for enhancing and confining light in a nanometer-wide low-index material. Light enhancement and confinement is caused by large discontinuity of the electric field at high index-contrast interfaces. They showed that by use of such a structure the field can be confined in a 50-nm-wide low-index region with a normalized intensity of $20 \mu\text{m}^{-2}$. This intensity is approximately 20 times higher than what can be achieved in SiO₂ with conventional rectangular waveguides.

Also in 2004, *Xu et al.* [3] experiments presented a silicon waveguide structure for guiding and confining light in nanometer-wide low-refractive-index material. The optical field in the low-index material is enhanced because of the discontinuity of the electric field at high-index-contrast interfaces. A 30% reduction of the effective index of light propagating in the novel structure due to the presence of the nanometer-wide low-index region is measured, evidencing the guiding and confinement of light in the low-index material. Ring resonators based on the structure were fabricated and showed that the structure can be implemented in highly integrated photonics.

A method of extracting waveguide slot admittance based on the simulated results of the commercial software High Frequency Structural Simulator (HFSS) was presented by *Mei-Qing et al.* 2005 [29]. The formula of calculating self-admittance of a single slot in waveguide was derived from transmission line theory, and that of calculating active admittance of a slot in array was given, simultaneously. With the proposed method, a waveguide slot antenna array can be designed easily and economically.

Blasco and Barrios, 2005 [30] presented a compact structure for highly efficient optical coupling to/from slot-waveguide from/to channel-waveguide. The mode-converter permits a coupling efficiency as high as 99.3% for a 3 μ m-long coupler.

Grillot et al. 2006 [31] have noticed that silicon-on-insulator (SOI) optical waveguides insure high electromagnetic field confinement but suffer both from sidewall roughness responsible of scattering effects and from leakage toward the silicon substrate. These two mechanisms are the main sources of loss in such optical waveguides. Considering the case of single-mode ultra-small square SOI waveguides, propagation loss was calculated at telecommunication wavelengths taking into account these two loss contributions. Leakage toward the substrate and scattering effects strongly depend on the waveguide size as well as on the operating wavelength.

In 2007, *Sun et al.* [32] measured the optical transmission at 1550 nm of the fundamental slot modes (quasi-TM modes) in horizontal single and multiple slot waveguides and ring resonators consisting of deposited amorphous silicon and silicon dioxide is demonstrated. Also it was demonstrated that the horizontal multiple slot configuration provides enhanced optical confinement in low index slot regions compared to a horizontal single slot structure with the same total SiO₂ layer thickness by

comparing their thermo-optic coefficients for the horizontal slot ring resonators. In these early structures, the horizontal slot waveguides have low propagation loss of 6 ~ 7 dB/cm has been shown. The waveguide loss was mainly due to a-Si material absorption. The addition of a Si/SiO₂ interfaces did not introduce significant scattering loss in a horizontal multiple slot waveguide compared to a horizontal single slot waveguide.

Yijing et al. 2007 [33] published an easy-to-fabricate multi-slot waveguide that is able to confine light in the low refractive index regions was describe. Its application for future silicon light emission device was discussed.

In the work of *Liu et al.* 2008 [34], mode behavior for SOI slot waveguides was modeled and analyzed using a numerical full vectorial method based on the film mode matching method (MMM). Only the quasi-TE mode was investigated. Waveguide heights and slot widths, as well as silicon widths are properly chosen with respect to the single mode behavior in the slot region. Comparison between the effective index method and our side loss method showed that their single mode condition was creditable. The optical power confinement in slot region for the quasi-TE mode was also studied and presented. The maximum achievable optical power confinement and the maximum normalized average optical intensity are 42% and $26 \mu\text{m}^{-2}$, respectively.

Wang et al. 2009 [8] gave both theoretical and experimental results of an ultra-compact waveguide coupler that is capable of highly efficient coupling of light from strip waveguides to slot waveguides, and vice versa were presented. By optimizing the geometrical parameters, it was possible to achieve extremely low-loss coupling. A coupling efficiency of 97% has been obtained experimentally while keeping the overall size down to the range below 10 μm . Further analysis showed that the

proposed coupler has relatively high tolerance to fabrication errors and is wavelength insensitive.

In 2010, *Ding et al.* [35] presented the first measurements of low-loss waveguides that are geometrically suitable for high bandwidth slot waveguide modulators: a strip-loaded slot waveguide were reported. Waveguide loss for undoped waveguides of 6.5 ± 0.2 dB/cm was achieved with 40 nm thick strip-loading, with the full silicon thickness around 220 nm and a slot size of 200 nm, for wavelengths near 1550 nm.

Both computer simulation and experiments have been conducted by *Chen et al.* 2011 [36] to understand the relationship between modulator performance such as modulation efficiency, optical loss and the waveguide design parameters. Techniques to achieve efficient poling of electro-optic polymers in the silicon slot waveguide have been developed. The doping of the silicon to enhance conductivity for efficient poling and the trade-off between conductivity and optical loss were experimentally investigated. Surface passivation of silicon nanophotonic structures has been found to be effective in improving poling efficiency.

In 2013, *Palmer et al.* [37] demonstrated a compact highly efficient broadband strip-to-slot mode converters in silicon was with record-low losses of 0.02 dB and negligible reflections between 1480 nm and 1580 nm. The new strip-to-slot transition is logarithmically tapered, which enables a compact design. The new logarithmic tapers were compared with more conventional linearly tapered converters.

A design scheme for silicon-based slot-waveguide crossing using a slot-to-strip mode converter (at each port) and a strip-multimode-waveguide (SMW) crossing was proposed *Xu et al.* 2013 [38]. The guided modes of the input slot-waveguide were first efficiently transformed into that of the single-mode strip waveguide by using the

mode converter, and then entered into the SMW, where fields converge at the center of the intersection due to the multimode interference effect.

Deng et al. 2014 [28] presented both numerical and experimental results of a strip-slot mode converter based on symmetric multimode interference (MMI) were presented. Strip-slot waveguide coupling through this mode converter had a measured efficiency of 97% (-0.13 dB), and the dimensions are as small as $1.24 \times 6 \mu\text{m}$. Further analysis shows that the proposed converter is highly tolerant to fabrication imperfections, and is wavelength-insensitive.

Silicon slot waveguides that can operate at the wavelength of high silicon absorption were experimentally demonstrated by *Li et al.* 2014 [10] on SOI wafer. The measured transmission loss coefficient could be as low as 2.28 ± 0.03 dB/mm at the wavelength of 1064nm (the slot width of 100nm), which is much lower than the absorption loss of silicon (5dB/mm at 1064nm). According to the simulation, such value is dominated by the surface roughness of sidewalls. The transmission loss is potentially to be reduced to 1 dB/mm if the side wall roughness could be reduced to 5 nm.

Also in 2014, *Li et al.* [39] proposed an ultra-compact and broadband orthogonal coupler between a strip waveguide and a slot waveguide. Numerical simulations showed that a 700 nm wide (full width at half maximum) coupling spectrum can be theoretically achieved and a coupling efficiency as high as 73% around 1500-nm wavelength can be obtained. The coupling length was only about 475 nm which made the coupler very compact. This configuration did not include a tapering section and had a high tolerance to the waveguide height, alleviating the stringent fabrication requirements.

This survey is showing how important the study of the whole losses in a slot waveguide experimentally and analytically.

1.5 Aim of Work

This thesis aims to estimate experimentally and theoretically the losses of the slot device, classify them according to their sources, study the influence of the characteristics of the slot device on these losses, and introduce a comprehensive analysis about the performance of this slot device. The scenario will include test and measure the transmission of about 200 slot devices with different characteristics using an experimental setup which employs a broadband super luminescent light emitting diode (SLED) light source whose wavelength range is 1500-1600 nm, besides de-embedding the effect of the grating couplers which is used to couple light between single mode fibers and slot devices. The work also aims to simulate the slot device and solve their modes using Fimmwave (from PhotonDesign) in order to find the losses and their sources. Finally, compare between the measured and simulated results and analyze them.

Chapter Two

Theoretical Background of Optical Waveguiding and Coupling

2.1 Introduction

In particular, the propagation of light in a photonic component is completely characterized by its wave nature. Since light propagates in the form of two mutually coupled vector waves, an electric field wave and a magnetic field wave, it is studied as electromagnetic waves and described by a vector wave theory. This nature of light is important in the operation of all photonic components but is particularly so for devices used in transmission, modulation, or switching of light [40]. SOI optical waveguides, most important photonic components, are the basic elements for confinement and transmission of light over various distances ranging from a few micrometers to a few millimeters in photonics integrated circuits. They are used to connect various photonic components. In many devices, they form important parts or key structures, such as the waveguides providing optical confinement in semiconductor lasers. Furthermore, they form important active or passive photonic components by themselves, such as waveguide couplers and modulators. In this chapter, the basic concepts and equations of electromagnetic wave theory required for the comprehension of lightwave

propagation in optical waveguides are presented. The light confinement and modes formation in the waveguide are qualitatively explained. As well as, most important waveguide shapes, coupling techniques, and expected losses through coupling and guiding processes are stated.

2.2 The Concepts of Electromagnetic Wave Theory

The study of light is a study of electromagnetic waves. In this section, Maxwell's equations, the wave equation, and boundary conditions of electromagnetic waves will be presented.

2.2.1 Maxwell's Equations

An electromagnetic field is described by two related vector fields that are functions of space and time: the electric field $\mathbf{E}(\mathbf{r},t)$ (V/m) and the magnetic field $\mathbf{H}(\mathbf{r},t)$ (A/m). In general, and according to that, six scalar functions of space and time are required to describe light in free space. Fortunately, these six functions are interrelated since they must satisfy the celebrated set of coupled partial differential equations known as Maxwell's equations. In free space, Maxwell's equations are [41]

$$\nabla \times \mathbf{E} = -\mu_0 \frac{\partial \mathbf{H}}{\partial t} \quad (2-1)$$

$$\nabla \times \mathbf{H} = \varepsilon_0 \frac{\partial \mathbf{E}}{\partial t} \quad (2-2)$$

$$\nabla \cdot \mathbf{E} = 0 \quad (2-3)$$

$$\nabla \cdot \mathbf{H} = 0 \quad (2-4)$$

where ε_0 is the electric permittivity of free space $\approx \frac{1}{36\pi} \times 10^{-9}$ (F/m) or (A.s/V.m) and μ_0 is the magnetic permeability of free space, $4\pi \times 10^{-7}$ (H/m) or (V.s/A.m).

In a medium in which there are no free electric charges or currents, two additional vector fields are required the electric flux density $\mathbf{D}(\mathbf{r}, t)$ (C/m²) and the magnetic flux density $\mathbf{B}(\mathbf{r}, t)$ (A/m²). So Maxwell's equations in a source-free medium are [42]

$$\nabla \times \mathbf{E} = -\frac{\partial \mathbf{B}}{\partial t} \quad (2-5)$$

$$\nabla \times \mathbf{H} = \frac{\partial \mathbf{D}}{\partial t} \quad (2-6)$$

$$\nabla \cdot \mathbf{D} = 0 \quad (2-7)$$

$$\nabla \cdot \mathbf{B} = 0 \quad (2-8)$$

The relationship between the electric flux density \mathbf{D} and the electric field \mathbf{E} depends on the electric properties of the medium, which are characterized by the polarization \mathbf{P} (C/m²). In a dielectric medium, the polarization density is the macroscopic sum of the electric dipole moments induced by the electric field. Similarly, the relation between the magnetic flux density \mathbf{B} and the magnetic field \mathbf{H} depends on the magnetic properties of the medium, embodied in the magnetization \mathbf{M} (A/m), which is defined analogously to the electric polarization. So the flux densities and the fields are related by [43]

$$\mathbf{D}(\mathbf{r}, t) = \varepsilon_0 \mathbf{E}(\mathbf{r}, t) + \mathbf{P}(\mathbf{r}, t) \quad (2-9)$$

$$\mathbf{B}(\mathbf{r}, t) = \mu_0 \mathbf{H}(\mathbf{r}, t) + \mu_0 \mathbf{M}(\mathbf{r}, t) \quad (2-10)$$

The vectors fields $\mathbf{P}(\mathbf{r}, t)$ and $\mathbf{M}(\mathbf{r}, t)$ are in turn related to the externally applied electric and magnetic fields $\mathbf{E}(\mathbf{r}, t)$ and $\mathbf{H}(\mathbf{r}, t)$ by relationships that

depend on the electric and magnetic character of the medium, respectively. Equations relating \mathbf{P} and \mathbf{E} , as well as \mathbf{M} and \mathbf{H} are established once the medium is specified. When these latter equations are substituted into Maxwell's equations in a source-free medium, the flux densities disappear. So the difference here that in free space, $\mathbf{P} = \mathbf{M} = 0$, so that $\mathbf{D}(\mathbf{r}, t) = \epsilon_0 \mathbf{E}(\mathbf{r}, t)$ and $\mathbf{B}(\mathbf{r}, t) = \mu_0 \mathbf{H}(\mathbf{r}, t)$ [44].

2.2.2 Wave Equations

The mathematical definition of an electromagnetic field which is a solution of Maxwell's wave equation [45]

$$\nabla^2 \mathbf{E}(\mathbf{r}, t) = \left[\frac{n^2(\mathbf{r})}{c^2} \right] \frac{\partial^2 \mathbf{E}(\mathbf{r}, t)}{\partial t^2} \quad (2 - 11)$$

\mathbf{r} is the radius vector, $n(\mathbf{r})$ is the index of refraction, and c is the speed of light in a vacuum,

$$c = \frac{1}{\sqrt{\epsilon_0 \mu_0}} \quad (2 - 12)$$

Definitely, that's applicable for magnetic field components. As mentioned in previous section that an optical field is described by two related vector fields that are functions of space and time: the electric field $\mathbf{E}(\mathbf{r}, t)$ and the magnetic field $\mathbf{H}(\mathbf{r}, t)$, which are solutions of the wave equation and for monochromatic electromagnetic wave are expressed as [45]

$$\mathbf{E}(\mathbf{r}, t) = \mathbf{E}(\mathbf{r}) e^{j\omega t} \quad (2 - 13)$$

$$\mathbf{H}(\mathbf{r}, t) = \mathbf{H}(\mathbf{r}) e^{j\omega t} \quad (2 - 14)$$

where $\mathbf{E}(\mathbf{r})$ and $\mathbf{H}(\mathbf{r})$ are the electric and magnetic fields vectors that functions of space only, and ω is the radian frequency. So if one of these

equations is used in Eq. (2-11), this wave equation will be reduced to Helmholtz equation [46]

$$\nabla^2 \mathbf{E}(\mathbf{r}) + k_o^2 n^2(\mathbf{r}) \mathbf{E}(\mathbf{r}) = 0 \quad (2-15)$$

$$\nabla^2 \mathbf{H}(\mathbf{r}) + k_o^2 n^2(\mathbf{r}) \mathbf{H}(\mathbf{r}) = 0 \quad (2-16)$$

where k_o is the wave number in the vacuum, and it is

$$k_o = \frac{\omega}{c} = \frac{2\pi}{\lambda_o} \quad (2-17)$$

and here, λ_o is the wavelength in the vacuum.

2.2.3 Boundary Condition for Electromagnetic Waves

In a homogeneous medium, all components of the fields \mathbf{E} , \mathbf{H} , \mathbf{B} , and \mathbf{D} are continuous functions of position. At the boundary between two dielectric media, in the absence of free electric charges and currents, the tangential components of the electric and magnetic fields \mathbf{E} and \mathbf{H} and the normal components of the electric and magnetic flux densities \mathbf{D} and \mathbf{B} must be continuous [44], as shown in Fig. 2.1.

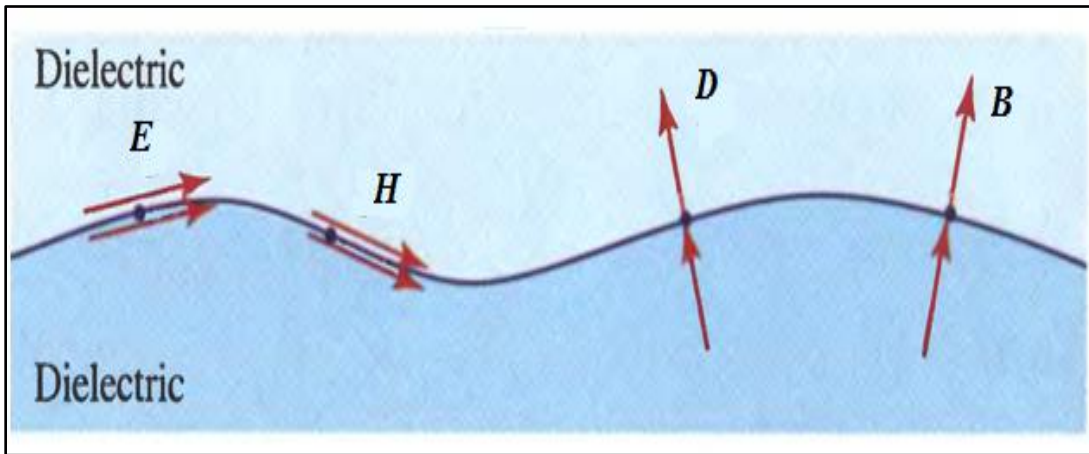


Fig. 2.1 Boundary conditions at the interface between two dielectric media [44].

These boundary conditions are an integral part of Maxwell's equations. They are used to determine the reflectance and transmittance of waves at various boundaries, and the propagation of waves in periodic structures and waveguides.

2.3 Basics of Optical Waveguides

The optical waveguide is the fundamental part that interconnects the various devices of a photonic integrated circuit, just as a metallic strip does in an electrical integrated circuit. However, unlike electrical current that flows through a metal strip according to Ohm's law, optical waves travel in the waveguide in distinct optical modes. A *mode*, in this sense, is a spatial distribution of optical energy in one or more dimensions that remains constant in time [45].

2.3.1 The Basic Waveguide's Structure

In general, the basic structure of a dielectric optical waveguide consists of a *core* which is high-index optical medium extended longitudinally and transversely surrounded by the *cladding* which is low-index media same as a conventional optical fiber structure. A guided optical wave propagates in the waveguide along its longitudinal direction z . The characteristics of a waveguide are determined by the transverse profile of its relative permittivity $\epsilon_r = \epsilon(x, y) / \epsilon_0$, which is independent of the z coordinate [40]. A waveguide made of optically isotropic media can be simply characterized with a single spatially dependent transverse profile of the index of refraction, $n(x, y)$. If the core of a waveguide is surrounded or sandwiched by a same cladding layer the waveguide is known as a

symmetric waveguide, and if there are different cladding layers then the upper, or the upper and sides, cladding layer is called *cover* while the lower cladding layer is called the *substrate* and the waveguide in this case is known as an asymmetric waveguide. A waveguide in which index profile has abrupt changes between the core and the cladding is called a step-index waveguide, while one in which the index profile varies gradually is called a *graded-index waveguide*. Figure 2.2 shows the index profiles of step-index and graded-index waveguides [40].

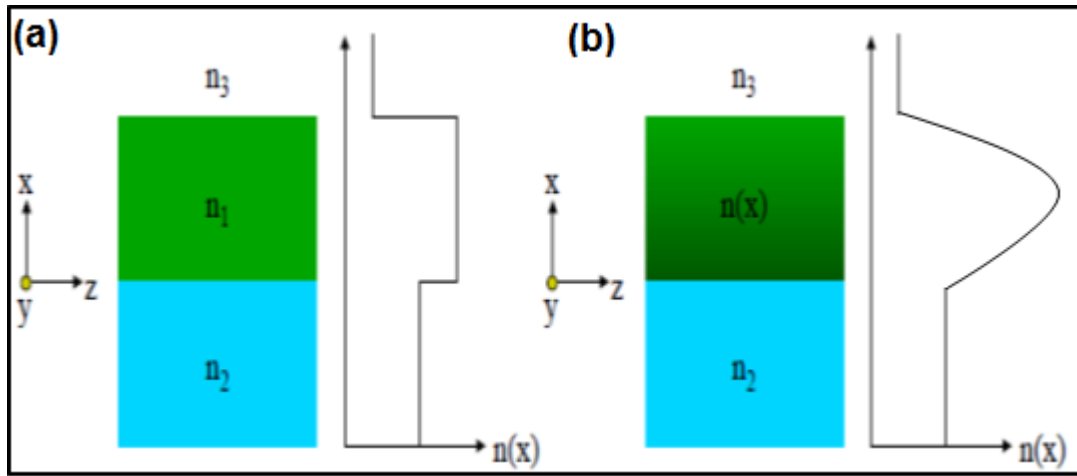


Fig. 2.2 Index profiles of an asymmetric (a) step-index planar waveguide and (b) graded-index planar waveguide [40].

Furthermore, the waveguide is considered a *planar* if it has an optical confinement in only one transverse direction, i.e. its core is sandwiched by the cladding in one direction only, as shown in Fig. 2.3 (a). In fact, this is not practical kind, especially in integrated photonics circuits, and it is almost used for theoretical description. On other hand, the more practical one which has an optical confinement in two transverse directions is known as a nonplanar or rectangular waveguide, as shown in Fig. 2.3 (b). There are several geometries of the rectangular waveguide such as; strip, ridge, and slot waveguides, which will be shown later in this chapter.

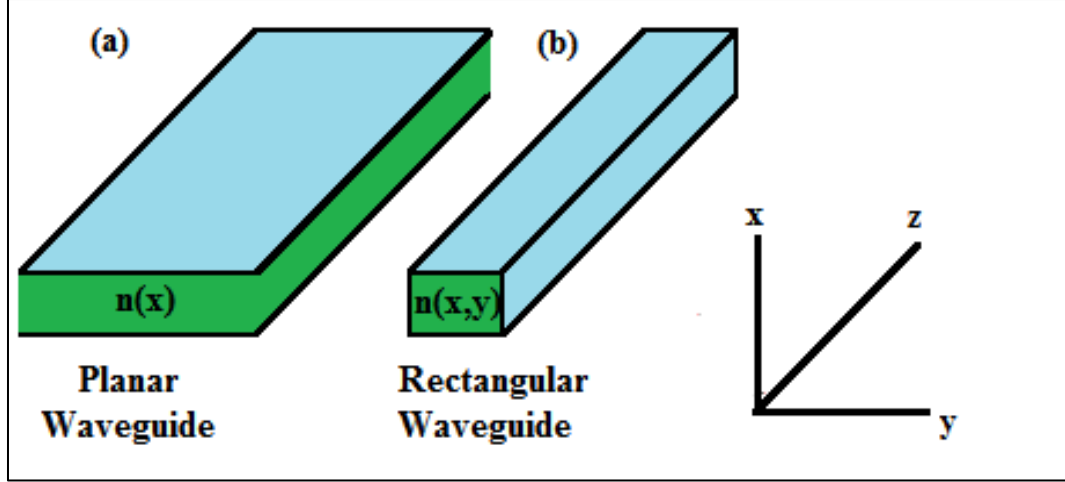


Fig. 2.3 (a) A planar waveguide and (b) a rectangular waveguide.

2.3.2 Optical Propagating in Asymmetric Waveguides

If an optical field is assumed, for convenience, to propagate in a waveguide whose structure is lossless and uniform in its optical axis or propagation direction, i.e. z -direction, the variation of this electromagnetic field with respect to z coordinate is constant such as [45]

$$\frac{\partial}{\partial z} = -j\beta, \quad (2-18)$$

β is the propagation constant and is the other face of the wave number, where it represents the z component of the wave number in this waveguide. Hence the optical field's vectors, which are still as mentioned previously constant with time, will be [45]

$$\mathbf{E}(\mathbf{r}) = \mathbf{E}(x, y)e^{-j\beta z} \quad (2-19)$$

$$\mathbf{H}(\mathbf{r}) = \mathbf{H}(x, y)e^{-j\beta z} \quad (2-20)$$

The ratio between the propagation constant in the waveguide and the wave number in the vacuum is called the *effective index* [46]

$$n_{eff} = \frac{\beta}{k_0}, \quad (2-21)$$

$$\beta = \frac{2\pi}{\lambda_0} n_{eff} = \frac{2\pi}{\lambda_0/n_{eff}} = \frac{2\pi}{\lambda_{eff}}, \quad (2-22)$$

where λ_{eff} is the z component of the wavelength in the waveguide. The physical meaning of the propagation constant is the angular spatial frequency. Hence, the effective index is the ratio between the wavelength in the waveguide to the wavelength in the vacuum or the ratio between the spatial frequency in the waveguide to its counterpart in the vacuum. Now the Helmholtz equations (in p. 16) can be rewritten as [45]

$$\nabla_{xy}^2 \mathbf{E}(x, y) + (k_0^2 n^2(\mathbf{r}) - \beta^2) \mathbf{E}(x, y) = 0 \quad (2-23)$$

$$\nabla_{xy}^2 \mathbf{H}(x, y) + (k_0^2 n^2(\mathbf{r}) - \beta^2) \mathbf{H}(x, y) = 0 \quad (2-24)$$

$\nabla_{xy}^2 \mathbf{E}(x, y)$, $\mathbf{E}(x, y)$ and $\nabla_{xy}^2 \mathbf{H}(x, y)$, $\mathbf{H}(x, y)$ are the solutions of (2-23 and 24) respectively. They represent the mathematical definition of the spatial energy distribution of an optical field in the medium, which then will be called “modes”. These modes are either sinusoidal or exponential functions with respect to (x,y) in each region depending on whether $(k_0^2 n_i^2 - \beta^2)$ is greater than zero or not, where $i=1, 2$, and 3 represents the cover, the core, and the substrate region respectively. Definitely, these modes are continuous at interface between regions therefore the possible modes, as shown in Fig. 2.4, are limited to,

i. Guided Modes in Asymmetric Waveguides

By considering; the mode shape changes as a function of β , a constant radian frequency ω , and $n_2 > n_3 > n_1$. When β is between $k_0 n_2$ and $k_0 n_3$, i.e. $k_0 n_2 > \beta > k_0 n_3$, modes will be confined and guided into the core region, as shown in Fig. 2.4 (a) and (b). They represent the zeroth order and first order mode respectively. This limitation on β can be visualized quite conveniently using the ray-optic approach; as the wave is reflected back and forth between the two interfaces, it interferes with itself. A guided mode can exist only when a transverse resonance condition is satisfied so that the repeatedly reflected wave has constructive interference with itself. In the core region, the x component of the wavevector is $k_0 n_2 \cos \theta$ for a ray with an angle of incidence θ , while the z component is $\beta = k_0 n_2 \sin \theta$. The phase shift in the optical field caused by a round-trip transverse passage in the core of thickness d is $2k_0 n_2 d \cos \theta$. In addition, there are phase shifts φ_1 and φ_3 associated with the internal reflections at the lower and upper interfaces, respectively. Because φ_1 and φ_3 are functions of θ , the transverse resonance condition for constructive interference in a round-trip transverse passage is [40]

$$2k_0 n_2 d \cos \theta + \varphi_1(\theta) + \varphi_3(\theta) = 2m\pi, \quad (2-25)$$

where m is an integer. Because m can assume only integral values, only certain discrete values of θ can satisfy (2-25). This results in discrete values of the propagation constant β_m for guided modes identified by the mode number m . The guided mode with $m = 0$ is called the *fundamental mode*, and those with $m \neq 0$ are *high-order modes*.

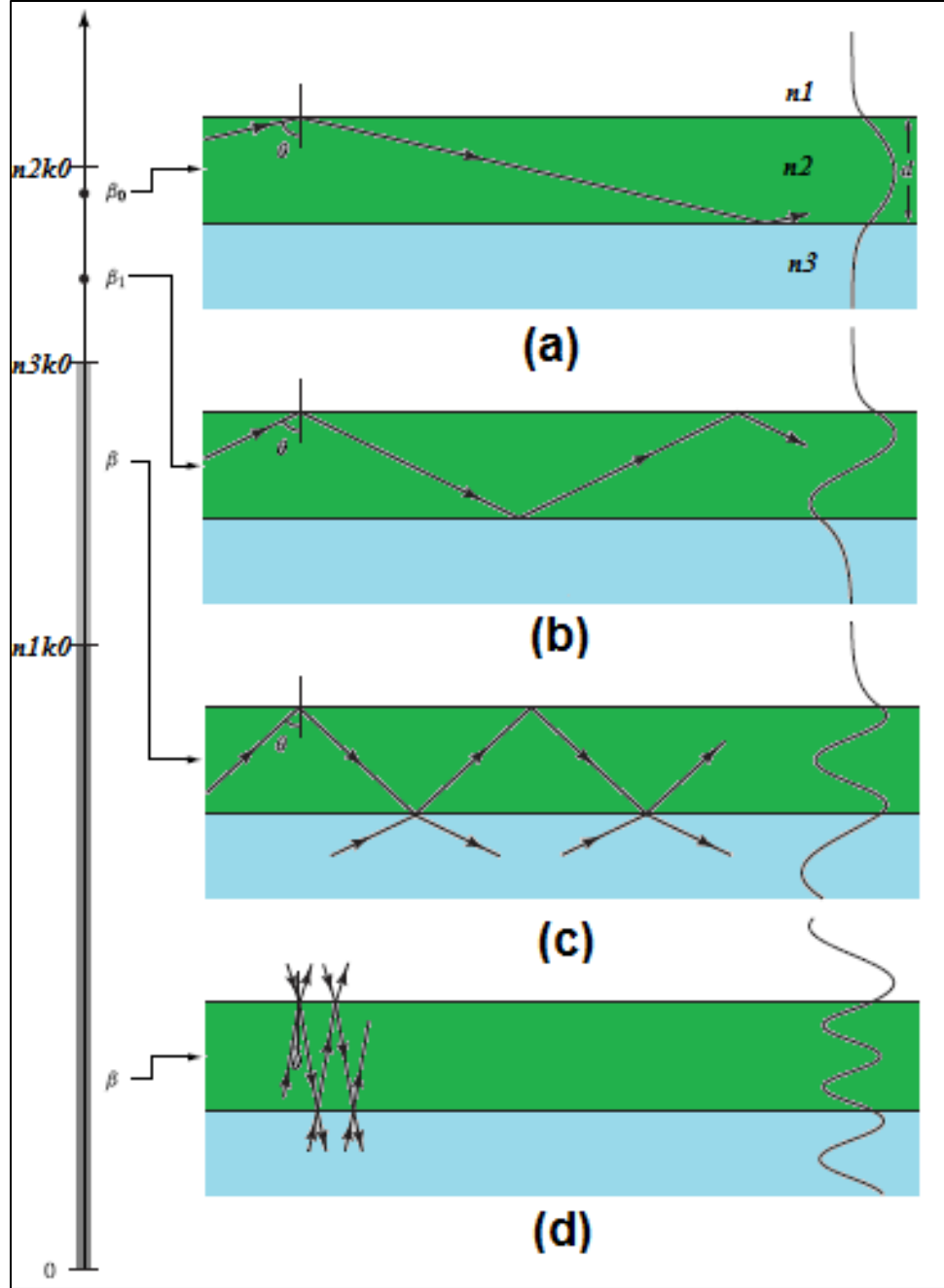


Fig. 2.4 Modes of an asymmetric planar step-index waveguide where $n_2 > n_3 > n_1$. The range of the propagation constants, the zig-zag ray pictures, and the field patterns are shown correspondingly for (a) the guided fundamental mode, (b) the guided first high-order mode, (c) a substrate radiation mode, and (d) a substrate–cover radiation mode. The waveguide structure is chosen so that it supports only two guided modes. The mode field profiles are calculated mode field distributions that are normalized to their respective peak values [40].

ii. Substrate Radiation Modes in Asymmetric Waveguides

This type of mode is not confined at the core but transversely extended to infinity the substrate, hence it is not discrete [40]. These modes are produced when β is greater than $k_0 n_1$ but still less than $k_0 n_3$. It can be supported by the waveguide structure, as shown in Fig. 2.4 (c), but because it is continuously losing energy from the core region to the substrate region as it propagates, it tends to be decayed out over at short distance. Hence it is not very useful in signal transmission, but, in fact, it may be very useful in coupler applications such as the tapered coupler [45].

iii. Cover-Substrate Radiation Modes in Asymmetric Waveguides

If β is less than $k_0 n_1$, the mode is oscillatory in all three regions of the waveguide structure. These modes are not guided modes because the energy is free to spread out of the core region. They are generally referred to as the air radiation modes of the waveguide structure. Of course, radiation is also occurring at the substrate interface. It is illustrated in Fig. 2.4(d).

In addition to the three types of modes discussed above, there are also *evanescent radiation modes*, which have purely imaginary values of β that are not discrete. Their fields decay exponentially along the z direction. In case of lossless waveguides which do not absorb energy, the energy of an evanescent mode radiates away from the waveguide transversely. A lossless waveguide cannot generate energy, either. Therefore, the evanescent modes do not exist in perfect, longitudinally infinite waveguides. They exist at the longitudinal junctions or imperfections of a waveguide, as well as at the terminations of a realistic waveguide of finite length. In comparison, a substrate radiation mode or a substrate–cover radiation mode has a real β ;

hence, its energy does not decay as it propagates. In such a radiation mode, the power flowing away from the center of the waveguide in the transverse direction is equal to that flowing toward the center [40].

2.3.3 The Cutoff Conditions

As shown previously, the number of modes that can be supported depends on the thickness d of the core layer and on ω , n_1 , n_2 and n_3 . For given d , n_1 , n_2 and n_3 there is a cutoff frequency ω_c below which waveguiding cannot occur. This ω_c corresponds to a long wavelength cutoff λ_c . Since wavelength is often a fixed parameter in a given application, the cutoff problem is for a given wavelength, so certain indices of refraction must be chosen in the three layers to permit waveguiding of a given mode. For the special case of the so-called asymmetric waveguide, in which n_1 is very much less than n_2 , it can be shown that the required indices of refraction are related by [45]

$$\Delta n = n_2 - n_3 > (2m + 1)^2 \lambda_0^2 / (32n_2 d^2), \quad (2 - 26)$$

where the mode number $m = 0, 1, 2, \dots$, and λ_0 is the vacuum wavelength. The change in index of refraction required for waveguiding of the lower-order modes is surprisingly small. Because only a small change in index is needed, a great many different methods of waveguide fabrication have proven effective in a variety of substrate materials.

2.3.4 Polarization

In the waveguide applications, the polarization state of the propagating mode usually has to be known. Polarization of light is determined by the direction of the electric field in time. The paraxial

electric-field vector propagates sinusoidal with different amplitude and phase at each vector position. When the waves are approximately transverse electromagnetic to the optical axis (z-axis) and the electric field lies in the transverse plane (x-y-plane), the wave is said to be elliptically polarized. The polarization state of the wave depends on the ratio of the magnitudes between x- and y-components, and the phase difference of the x- and y components. When the magnitude ratio is one and the phase difference is $\pm\pi/2$, the light is circularly polarized. The light is linearly polarized if the magnitude of the x- or y-component is zero, or if the phase difference between x- and y-components is either 0 or π . The waveguide modes, having an electric field transverse to the optical axis and parallel to the surface, are called transverse electric TE-modes. When the magnetic field is transverse to the optical axis, the mode is called transverse magnetic TM-mode. Figure 2.5 shows the field direction of TE and TM modes in planar waveguide.

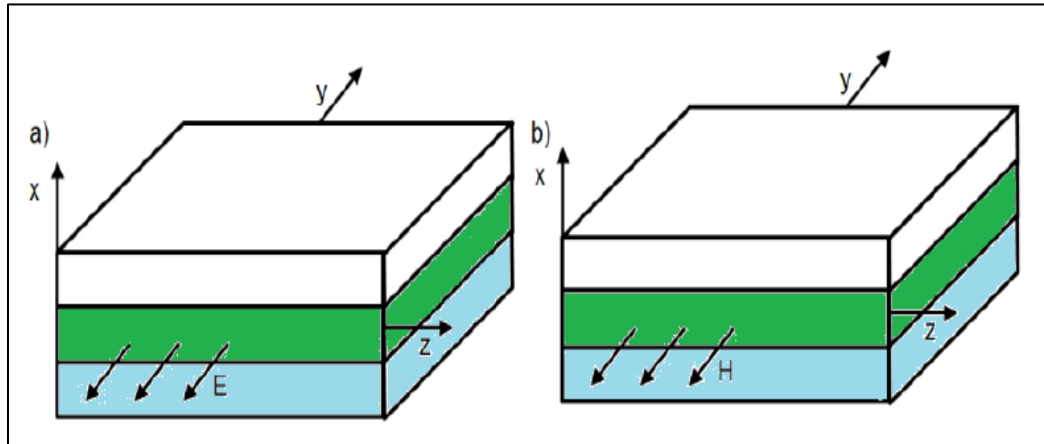


Fig. 2.5 (a) TE field and (b) TM field of propagating light [47].

In practice, the fields that propagate through a waveguide will not exactly be TE or TM modes, that is, they will also have field distribution in the direction perpendicular to the direction in which they are polarized. So, if

considering electrical fields, TE modes is in the x direction and has some field energy in the y direction, and TM modes are normally in the y direction but have some energy in the x direction. Therefore, a criterion has to be chosen to be able to differentiate between modes. This is the following:

For TE modes: if $\text{Re}(E_y) \gg \text{Re}(E_x)$, the mode is said to be quasi-TE or directly TE. For TM modes: if $\text{Re}(E_y) \ll \text{Re}(E_x)$, the mode is said to be quasi-TM or TM [48].

2.3.5 Modes in a Three-Layer Slab Waveguide

The planar slab waveguide structure forms the starting point of all theoretical developments of wave propagation in waveguides where it has a fundamental geometry that has been considered as the basis for more sophisticated waveguide structure. Figure 2.6 shows the structure of the three-layer slab waveguide, where n_1 , n_2 , and n_3 are refractive indices of the cover, the core, and the substrate regions. This structure is assumed to be uniform in the y and z directions and infinite in y direction. Since that the Helmholtz equations (2-23 and 24) for the electric and magnetic fields respectively can be recalled as

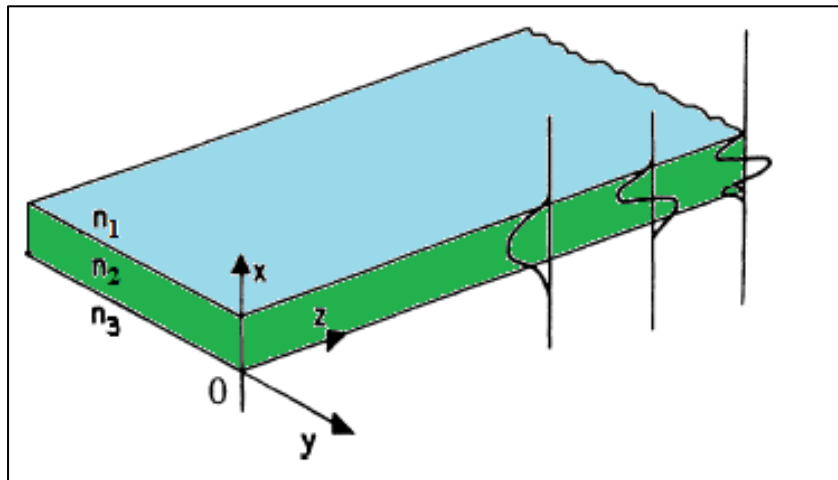


Fig. 2.6 Diagram of a planar waveguide structure [45].

$$\frac{\partial^2 \mathbf{E}(x)}{\partial x^2} + (k_o^2 n_i^2 - \beta^2) \mathbf{E}(x) = 0 \quad (2-27)$$

$$\frac{\partial^2 \mathbf{H}(x)}{\partial x^2} + (k_o^2 n_i^2 - \beta^2) \mathbf{H}(x) = 0 \quad (2-28)$$

where $\frac{\partial}{\partial y}=0$. Now, the two modes; TE and TM, which propagate through the three-layer slab optical waveguide, will be discussed by re-deriving the wave equation from Maxwell's equation for an optical waveguide

$$\nabla \times \mathbf{E} = -j\omega\mu_o \mathbf{H} \quad (2-29)$$

$$\nabla \times \mathbf{H} = j\omega\epsilon_o\epsilon_r \mathbf{E} \quad (2-30)$$

whose components representation are [46]

$$\frac{\partial E_z}{\partial y} - \frac{\partial E_y}{\partial z} = -j\omega\mu_o H_x \quad (2-31)$$

$$\frac{\partial E_x}{\partial z} - \frac{\partial E_z}{\partial x} = -j\omega\mu_o H_y \quad (2-32)$$

$$\frac{\partial E_y}{\partial x} - \frac{\partial E_x}{\partial y} = -j\omega\mu_o H_z \quad (2-33)$$

$$\frac{\partial H_z}{\partial y} - \frac{\partial H_y}{\partial z} = j\omega\epsilon_r\epsilon_o E_x \quad (2-34)$$

$$\frac{\partial H_z}{\partial y} - \frac{\partial H_y}{\partial z} = j\omega\epsilon_r\epsilon_o E_x \quad (2-35)$$

$$\frac{\partial H_z}{\partial y} - \frac{\partial H_y}{\partial z} = j\omega\epsilon_r\epsilon_o E_x \quad (2-36)$$

where $\frac{\partial}{\partial t} = j\omega$, the relative permeability is assumed to be equal to one, $\mu_r = 1$, so $\mu = \mu_r\mu_o = \mu_o$, and as mentioned before the derivative with respect to z direction $\frac{\partial}{\partial z}$ can be replaced with $(-j\beta)$.

In case of TE mode, the electric field is not in the longitudinal direction ($E_z=0$), it is in the transverse direction ($E_y \neq 0$) but since the uniform structure with y direction the variation with respect to it will be zero, $\frac{\partial}{\partial y}=0$. By using all these relations in the above set equations, TE mode components will be

$$E_z = E_x = H_y = 0 \quad (2-37)$$

$$H_x = -(\beta/\omega\mu_0)E_y \quad (2-38)$$

$$H_z = (j/\omega\mu_0)\frac{\partial E_y}{\partial x} \quad (2-39)$$

while the wave equation of the principle electric component E_y is

$$\frac{\partial^2 E_y}{\partial x^2} + (k_0^2 n_i^2 - \beta^2)E_y = 0 \quad (2-40)$$

and this component, E_y , in each of the three layers is

$$E_y(x) = A \exp(\gamma_3 x) \quad 0 \geq x \quad (2-41)$$

$$= B \cos(\gamma_2 x + \delta) \quad d \geq x \geq 0 \quad (2-42)$$

$$= C \exp[-\gamma_1(x-d)] \quad \infty \geq x \geq d \quad (2-43)$$

where A , B , and C are arbitrary constants, d is the thickness of the core region, γ_1 , γ_2 , γ_3 , and δ can be expressed as [46]

$$\gamma_3 = (\beta^2 - n_1^2 k_0^2)^{1/2}, \quad (2-44)$$

$$\gamma_2 = (n_2^2 k_0^2 - \beta^2)^{1/2}, \quad (2-45)$$

$$\gamma_1 = (\beta^2 - n_3^2 k_0^2)^{1/2}, \quad (2-46)$$

$$\tan(\delta) = -\left(\frac{\gamma_3}{\gamma_2}\right) + i\pi \quad i = 1, 2, 3 \dots \quad (2-47).$$

In the case of TM mode, the magnetic field is not in the longitudinal direction ($H_z=0$), it is in the transverse direction ($H_y \neq 0$) but since the uniform structure with y direction the variation with respect to it will be zero, $\frac{\partial}{\partial y}=0$. So the TM mode components are [46]

$$H_z = H_x = E_y = 0 \quad (2-48)$$

$$E_x = (\beta / \omega \epsilon_0 \epsilon_r) H_y \quad (2-49)$$

$$E_z = -(j / \omega \epsilon_0 \epsilon_r) \frac{\partial H_y}{\partial x} \quad (2-50)$$

and the wave equation for the TM mode principle component, H_y , is

$$\frac{\partial^2 H_y}{\partial x^2} + (k_0^2 n_i^2 - \beta^2) H_y = 0 \quad (2-51)$$

while this component in the three layer will take the same expressions as in Eqs.(2-41 to 43).

2.3.6 The Confinement Factor

As seen from the field profiles, the power propagating along the guide is not totally confined *inside* the core of the guide, but rather a part of the power leaks into the two cladding layers. A useful parameter describing the light-guiding property of the waveguide is the mode confinement factor (Γ) defined as follows [49]:

$$\Gamma = \frac{\int_0^d E_y^2(x)}{\int_{-\infty}^{\infty} E_y^2(x)} dx \quad (2-52)$$

This factor quantifies how much fraction of the total power belonging to the particular mode is confined within the guide layer. It is a function of

polarization, of the refractive index difference, of the thickness of the guide, and of the mode number.

2.3.7 Waveguides Geometries

The simplest waveguide structure is a slab waveguide as illustrated in Fig. 2.7(a). It consists of parallel planar layers, which are infinite in lateral directions. This kind of waveguide structure is not very practical in many applications, since the light is confined only in vertical direction [40]. In order to confine the light in two directions, several other geometries are exploited. These useful structures are illustrated in Fig. 2.7(b-f), in which the darker color expresses the higher refractive index. In the strip waveguide, Fig. 2.7 (b), the light is confined in the strip of higher refractive index material than the substrate and cover. The light is confined laterally by including a locally higher volume of core material in a vertical direction in a ridge (Fig. 2.7 (c)), and an inverted ridge (Fig. 2.7(d)) waveguide geometry. In these two geometries, the height and the width of the ridge together with the slab thickness and the refractive indices determine the shapes and the number of guiding modes. In silicon photonic applications, a strip and a ridge waveguides are usually exploited. A ridge or inverted ridge geometries are commonly used for polymer waveguides [47]. The effective index in the high refractive index slab layer is locally higher under a lower refractive index strip than in the adjacent regions in a strip-loaded waveguide structure (Fig. 2.7(e)). Strip-loaded waveguides have been fabricated, for instance, as an SOI structure [35]. In the slot waveguide geometry, the light is confined in the low refractive index material between the higher refractive index rails. The slot waveguide (Fig. 2.7(f)) geometry is discussed in detail in later paragraph that follow.

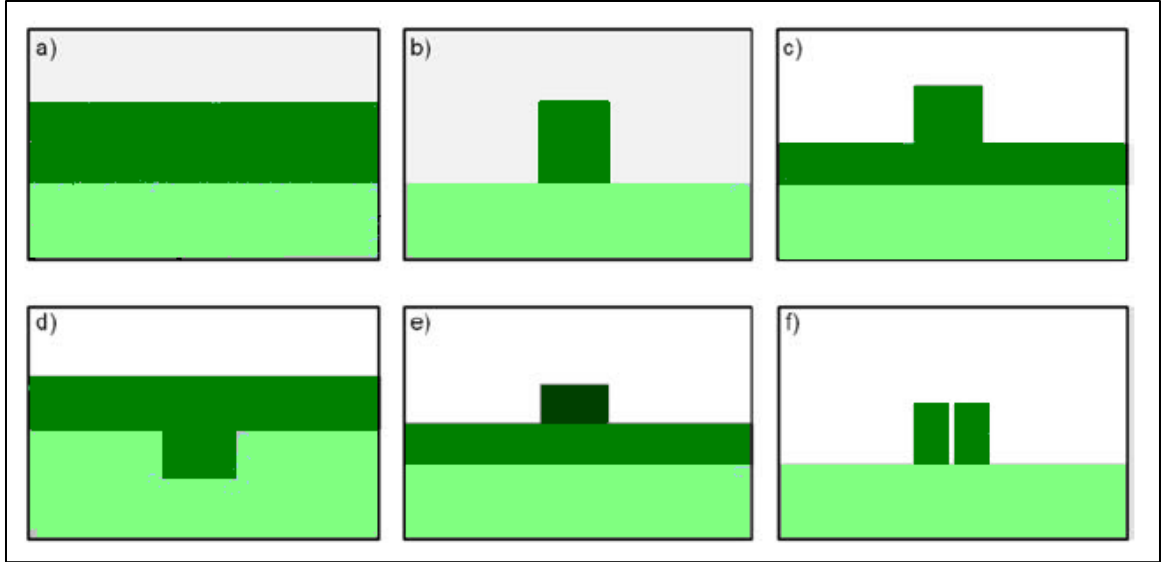


Fig. 2.7 Cross-section image of different waveguide geometries a) slab waveguide; b) rib waveguide; c) ridge waveguide; d) inverted ridge waveguide; e) strip-loaded waveguide; f) slot waveguide [50].

2.3.8 SOI Waveguides

The SOI waveguide uses silicon as a substrate as well as the waveguiding core material. The configuration of an SOI wafer is shown in Fig. 2.8. The silicon guiding layer and the buried silicon dioxide are varied for each individual design. The purpose of the buried oxide layer is to act as the lower cladding layer, and hence prevent the field associated with the optical fields (modes) from penetrating the silicon substrate below. The SOI material system has a number of distinct advantages over the other commonly used platforms such as the III-V semiconductor compounds and polymers. First, the high refractive index contrast between the silica cladding and the silicon waveguide core facilitates the confinement and guiding of light in structures within submicron dimensions [48]. In addition, the mature silicon micro-fabrication technology establishes a firm foundation for making low-cost and compact integrated photonic devices.

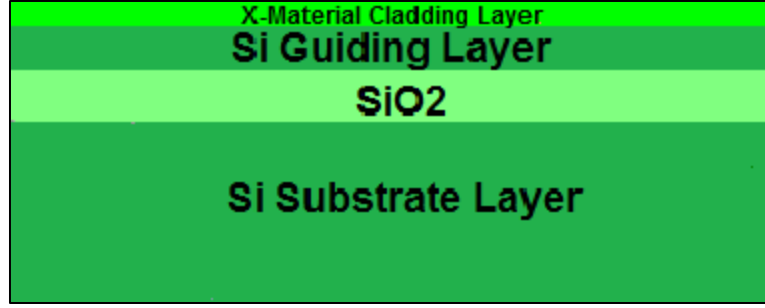


Fig. 2.8 SOI planar waveguide [48].

2.4 Slot Waveguides

Slot waveguides typically consist of two ribs of high-index material that enclose a subwavelength low-index slot region, as shown in Fig. 2.9. It is fully compatible with highly- integrated photonics technology, retaining most of its important properties such as nanometersized cross-section dimensions and small minimum bend radius.

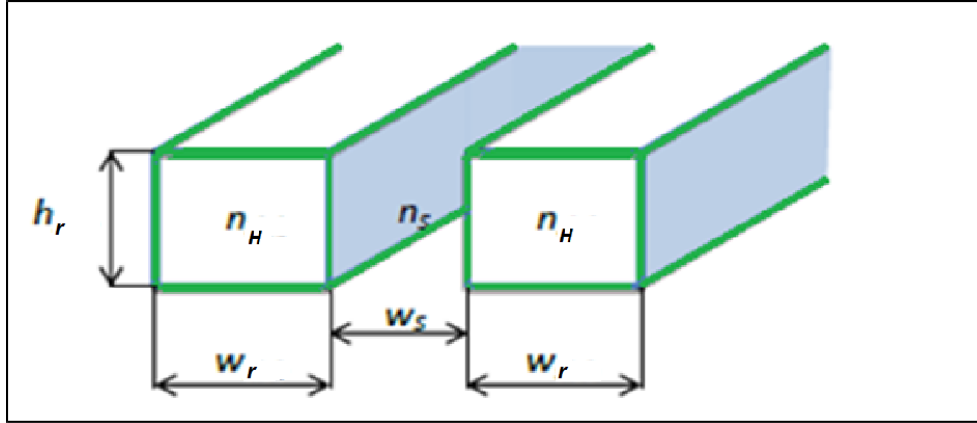


Fig. 2.9 Schematic diagram of the slot waveguide geometry. Rib width w_r , rib height h_r , rib refractive index n_H , slot width w_s and slot refractive index n_s are defined [2, 3].

Potential applications for the slot-waveguide include host for active materials, sensing, non-linear optics, optical modulators and switches, near-field optical microscopy, and efficient coupling to nanometer-sized waveguides and structures [51-52].

2.4.1 The Principle of Operation

The principle of operation of the slot-waveguide is based on the discontinuity of the normal component of the electrical field \mathbf{E} at the high-index-contrast interface. From Maxwell's equations, the normal component of the electric flux density \mathbf{D} is continuous at the interface of two dielectric materials. Since $\mathbf{D} = \epsilon_r \epsilon_0 \mathbf{E} = n^2 \epsilon_0 \mathbf{E}$, where n , ϵ_r and ϵ_0 are the refractive index, dielectric constant and vacuum permittivity, respectively, the normal component of \mathbf{E} shows discontinuity if n is different at opposite sides of the interface. The electrical field is then higher at the low-index side and lower at the high-index side, with the ratio equal to the square of the index contrast $(n_{High}/n_{Low})^2$. This discontinuity has usually been overlooked because most of the investigated photonic structures rely on low-index-contrast. However, for high-index-contrast structures, this discontinuity is significant. The optical intensity in the slot is also much higher than that in the high-index region, since the magnetic field \mathbf{H} is continuous at the interface and varies slowly across the structure. On the other hand, the major electric field component of the quasi-TM mode is parallel to the interface of index contrast, resulting in an electrical field that is continuous at the walls of the slot. As a result, the presence of the slot does not affect the quasi-TM mode as strongly as it affects the quasi-TE mode [2, 3].

2.4.2 The Analysis of Operation

The slot waveguide layout considered is given in Fig. 2.10 [3]. The waveguide is considered to be infinite along x direction. The advantage of considering this layout is that it can be analyzed from first principles without resorting to any FEM techniques. If the waveguide is finite in x direction it

will correspond to a ridge waveguide. The quasi TE mode of the ridge waveguide will qualitatively (and to some extent quantitatively) correspond to TM mode supported by slot waveguide shown in Fig. 2.10.

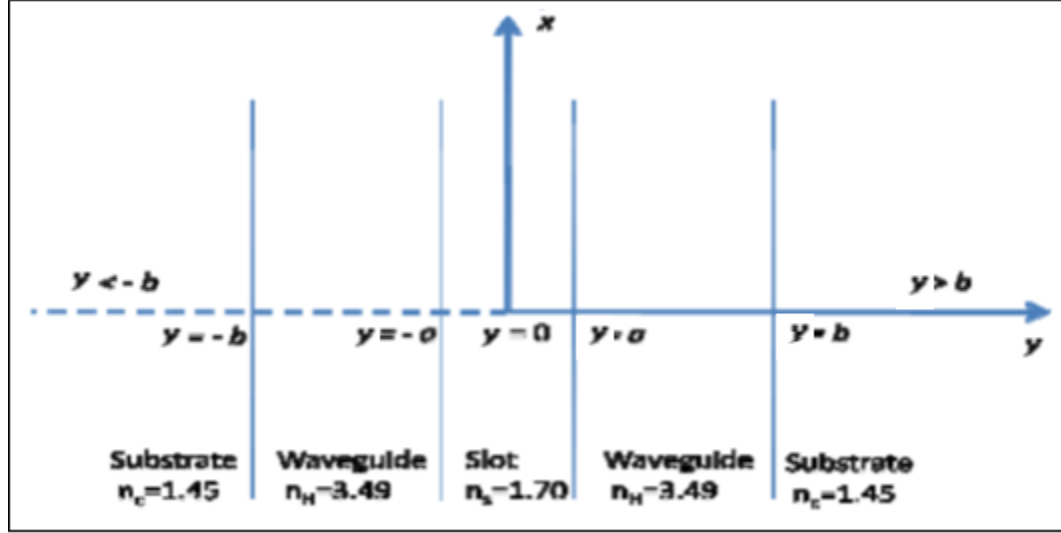


Fig. 2.10 The planar slot waveguide layout, with slot width $w_s=2a$, slot refractive index, $n_s=1.7$, rib width $w_r=b-a$, rib refractive index $n_H=3.49$, and substrate refractive index, $n_c=1.45$ [3]

Now, to find the eigen equation and guided field without loss of any ambiguity, following are assumed [2,3]

$$\frac{\partial}{\partial x} = 0, \quad \frac{\partial}{\partial z} = -j\beta, \quad \frac{\partial}{\partial t} = +j\omega. \quad (2-53)$$

By applying the above condition in Maxwell's curl equations (2-5 to 2-8) and solving the following can be gotten

I. In slot ($|y| < a$) [2,3]

$$H_x = A \cosh(\gamma_s |y|) \quad (2-54a)$$

$$E_y = \left(\frac{\beta}{\omega \varepsilon_0 n_s^2} \right) A \cosh(\gamma_s |y|) \quad (2-54b)$$

with A as arbitrary constant and

$$\gamma_s = k_0 \sqrt{n_{eff}^2 - n_s^2} \quad (2-55)$$

II. In waveguide ($a < |y| < b$) [2,3]

After applying the boundary conditions of continuity of H_x and E_z at $y = a$, the following are obtained

$$H_x = A \left[\cosh(\gamma_s a) \cos K_H(|y| - a) + \left(\frac{n_H^2}{n_s^2} \right) \left(\frac{\gamma_s}{K_H} \right) \sinh(\gamma_s a) \sin K_H(|y| - a) \right] \quad (2-56a)$$

$$E_y = \left(\frac{\beta}{\omega \varepsilon_0 n_H^2} \right) A \left[\cosh(\gamma_s a) \cos K_H(|y| - a) + \left(\frac{n_H^2}{n_s^2} \right) \left(\frac{\gamma_s}{K_H} \right) \sinh(\gamma_s a) \sin K_H(|y| - a) \right] \quad (2-56b)$$

with

$$K_H = k_0 \sqrt{n_H^2 - n_{eff}^2} \quad (2-57)$$

III. In cladding ($|y| > b$) [2,3]

After applying the boundary conditions of continuity of H_x and E_z at $y = b$, the following are obtained

$$H_x = A \left[\frac{\cosh(\gamma_s a) \cos K_H(|y| - a) + \left(\frac{n_H^2}{n_s^2}\right) \left(\frac{\gamma_s}{K_H}\right) \sinh(\gamma_s a) \sin K_H(|y| - a)}{\left(\frac{n_H^2}{n_s^2}\right) \left(\frac{\gamma_s}{K_H}\right) \sinh(\gamma_s a) \sin K_H(|y| - a)} \right] e^{-\gamma_c(|y| - b)} \quad (2 - 58a)$$

$$E_y = \left(\frac{\beta}{\omega \epsilon_0 n_H^2} \right) A \left[\frac{\cosh(\gamma_s a) \cos K_H(|y| - a) + \left(\frac{n_H^2}{n_s^2}\right) \left(\frac{\gamma_s}{K_H}\right) \sinh(\gamma_s a) \sin K_H(|y| - a)}{\left(\frac{n_H^2}{n_s^2}\right) \left(\frac{\gamma_s}{K_H}\right) \sinh(\gamma_s a) \sin K_H(|y| - a)} \right] e^{-\gamma_c(|y| - b)} \quad (2 - 58b)$$

with

$$\gamma_c = k_0 \sqrt{n_{eff}^2 - n_c^2} \quad (2 - 59)$$

The boundary conditions at $y = b$ also yields eigen value equation, given as

$$\tan[K_H(b - a) - \phi] = \left(\frac{n_H^2}{n_s^2}\right) \left(\frac{\gamma_s}{K_H}\right) \tanh(\gamma_s a) \quad (2 - 60)$$

with

$$\phi = \text{atan} \left(\left(\frac{n_H^2}{n_s^2}\right) \left(\frac{\gamma_s}{K_H}\right) \right) \quad (2 - 61)$$

2.4.3 SOI Slot Waveguides

A typical cross section of a silicon-on-insulator (SOI) slot waveguide is depicted in Fig. 2.11 (a). The waveguide core consists of two high-index Si ribs with height h and width w_r that are embedded into a low-index PI cladding.

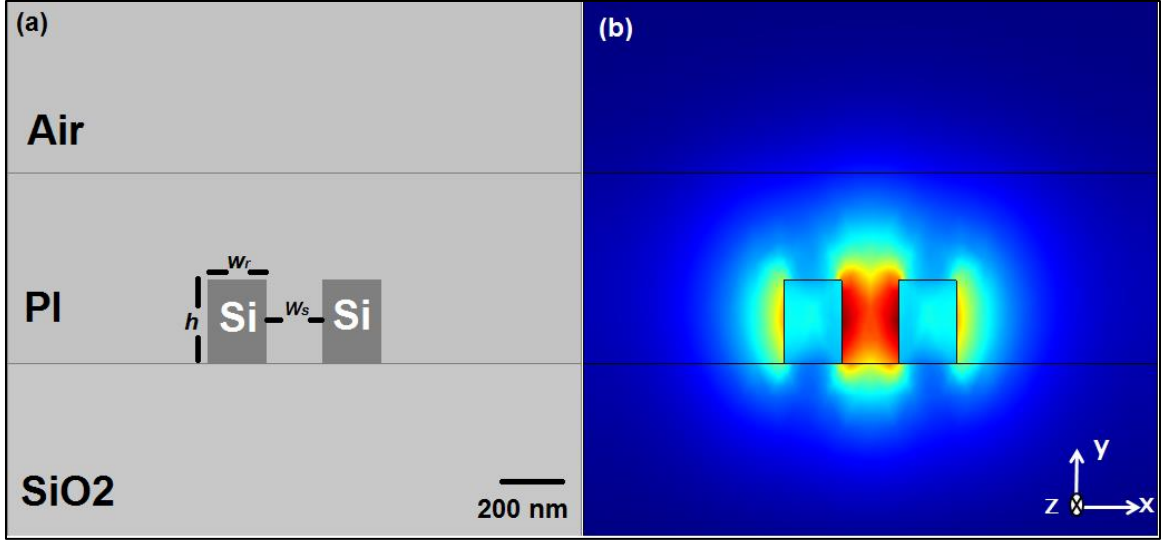


Fig. 2.11(a) Schematic cross section of an SOI slot waveguide, coated by Polymide (PI, $n=1.7$), with Si rib height h , Si rib width w_r , and a slot width w_s . (b) Dominant electric field component (E_x) of the fundamental TE mode field cross the slot waveguide at $\lambda = 1550$ nm.

Discontinuities of the horizontal electric field component E_x at the high index contrast interfaces lead to strong field enhancement in the slot region. The transverse electric profile for the quasi-TE mode is shown in Fig 2.11 (b) is simulated with the refractive indices $n_1 = 1.7$, $n_2 = 3.49$, and $n_3 = 1.45$, for Polymide PI, Si, and SiO₂ respectively, at $\lambda = 1550$ nm. As in standard SOI waveguides, the buried oxide of the SOI wafer acts as a buffer region that optically isolates the waveguide from the bulk silicon handle wafer. In a slot waveguide, this effect is exploited at both sidewalls to obtain an electric mode field that is strongly confined to the slot region. Slot widths are much smaller than the penetration depths of the evanescent field leading to large intensities throughout the slot region.

2.5 Propagation Losses in Optical Waveguides

Losses in an optical waveguide originate from three sources: scattering, absorption and radiation. Within each category are further subdivisions of the contribution to the loss, although the relative contribution of each of these effects is dependent upon the waveguide design and the quality of the material in which the waveguide is fabricated. Each of the contributions to loss will be discussed in turn.

I. Scattering Surface Loss

Scattering in an optical waveguide can be of two types: volume scattering and interface scattering. Volume scattering is caused by imperfections in the bulk waveguide material, such as voids, contaminant atoms, or crystalline defects. Interface scattering is due to roughness at the interface between the core and the claddings of the waveguide. Usually, in a well-established waveguide technology, volume scattering is negligible, because the material has been improved to a sufficient level prior to fabrication of the waveguide. For new or experimental material systems, however, volume scattering should always be considered. Interface scattering may not be negligible, even for a relatively well developed material system, because losses can be significant even for relatively smooth interfaces. It has been shown that the contribution to volume scattering is related to the number of defects, their size with respect to the wavelength of propagation, and the correlation length along the waveguide. In bulk media, Rayleigh scattering is the dominant loss mechanism [53], which exhibits λ^{-4} dependence. However, for confined waves the

wavelength dependence is related to the axial correlation length of the defects [54]. For correlation lengths shorter than or of the order of the wavelength, the scattering loss exhibits a λ^{-3} dependence, because the reduction of confinement for longer wavelengths partially counters the λ^{-4} relation. For long correlation lengths compared to the wavelength, radiation losses dominate and λ^{-1} dependence is observed.

Interface scattering has been studied by number of authors, who have published a range of expressions for approximating the scattering from the surface or interface of an optical waveguide. However, since many of these models are very complex, an approximate technique will be introduced here, which is attractive owing to its simplicity. The theory of this technique was first introduced by Tien in 1971 [55], and is based upon the specular reflection of power from a surface. This condition holds for long correlation lengths, which is a reasonable assumption in most cases. By considering the total power flow over a given distance, together with the loss at both waveguide interfaces, Tien produced the following expression for the loss coefficient due to interface scattering [20]:

$$\alpha_{scatt.}(\mu m^{-1}) = \frac{4\pi^2\sigma^2}{\lambda_o^2} \sqrt{n_H^2 - n_{eff}^2} \frac{E_s^2}{\int E^2 dx} \Delta n^2 \quad (2 - 62)$$

where, σ is the amount of the roughness on the sidewalls in μm , n_{eff} is the effective index of the fundamental quasi-TE mode, Δn is the refractive index contrast between the waveguide ribs and coating layer

(cladding), and $\frac{E_s^2}{\int E^2 dx}$ (μm^{-1}) is the normalized electric field intensity at the side interfaces of core/cladding. For strip waveguide, the electric field intensity and interface roughness of two etched sidewalls are both identical and symmetrical. Thus, Eq. (2-62) covers the scattering of both the two etched sidewalls. Different to typical strip waveguide, there are two interfaces in slot waveguide contributing to the scattering, where the electric field intensity (E_{s1} and E_{s2}) has obvious disparities the total field intensity is calculated as ($E_s^2 = E_{s1}^2 + E_{s2}^2$) [10]. Also the loss in dB/cm can be calculated by [45]

$$\mathcal{L}_{scattering}(dB/\mu m) = 4.3 * \alpha_{scatt.}(\mu m^{-1}) \quad (2 - 63)$$

II. Absorption Loss

The two main potential sources of absorption loss for semiconductor waveguides are band edge absorption (or interband absorption), and free carrier absorption. Interband absorption occurs when photons with energy greater than the band gap are absorbed to excite electrons from the valence band to the conduction band. Therefore to avoid interband absorption, a wavelength must be used that is longer than the absorption edge wavelength of the waveguide material. Silicon is an excellent example material to demonstrate this point. The band edge wavelength of silicon is approximately $1.1\mu m$, above which silicon is used as a waveguide material. For wavelengths shorter than $1.1\mu m$, silicon absorbs very strongly, and it is one of the most common materials used for photodetectors in the visible wavelength range, and at very short infrared wavelengths. The band

edge absorption of a material does not mark an abrupt transition from strong absorbance to transparency, so care must be taken when selecting a wavelength for a given technology. Free carrier absorption, however, may be significant in semiconductor waveguides. The concentration of free carriers will affect both the real and imaginary refractive indices. Changes in absorption in semiconductors can be described by the well-known Drude–Lorenz equation [56]:

$$\Delta\alpha = \frac{e^3\lambda_0^2}{4\pi^2n\varepsilon_0c_0^3} \left(\frac{N_e}{\mu_e(m_{cc}^*)^2} + \frac{N_h}{\mu_h(m_{ch}^*)^2} \right) \quad (2-64)$$

where c_0 is the velocity of light in vacuum; e is the electron charge; μ_e is the electron mobility; μ_h is the hole mobility; m_{cc}^* is the effective mass of free electrons; m_{ch}^* is the effective mass of holes; N_e is the free electron concentration; N_h is the free hole concentration; ε_0 is the permittivity of free space; and λ_0 is the free space wavelength. Some of the parameters in Eq. (2-64) are interdependent, so care must be taken when evaluating the effect of free carrier absorption.

III. Radiation Loss

Radiation loss from a straight optical waveguide should ideally be negligible. This type of loss implies leakage from the waveguide into the surrounding media, typically the upper or lower cladding, or for a rib waveguide, into the planar region adjacent to the guide. If the waveguide is well designed this loss will not normally be significant, although unwanted perturbations in the waveguide due to, for example, a slightly damaged fabrication mask may cause scattering of light from one mode to another. The second mode may in turn result

in some radiative loss if that mode is leaky. Another situation that may result in some radiative loss is curvature of the waveguide, as this will change the angle of incidence at the waveguide wall, which may in turn result in some radiative loss [49].

According to all above, it can be concluded that the propagation losses in an optical waveguide, especially in a slot waveguide, will be dominated by interface scattering losses.

2.6 Waveguide Input and Output Couplers

One of the challenging tasks in optical systems is efficiently coupling light into and out of the optical waveguides. In general, light from a standard optical fiber or an external light source needs to be coupled to a silicon waveguide. A single-mode fiber core usually has a diameter of about 8 μm with a symmetric mode, while a silicon waveguide is typically a few μms wide with an asymmetrical mode [49]. To overcome these large differences in effective index, core size, and symmetry, various techniques are developed for efficiently coupling light from fiber to the guide. In the end-fire and butt-coupling schemes, light is simply allowed to shine onto the end faces of the waveguide.

These techniques are shown schematically in Fig. 2.12. In taper coupling, the two devices are simply butted, such that the mode field of the transmitting device falls onto the end face of the receiving device. In end-fire coupling, a lens is employed to focus the light beam onto the end face of the collecting device where the input light beam can excite all the modes of the waveguide. In the prism coupling and grating coupling, the input beam impinges on the guide at a specific angle, as shown in Fig. 2.12.

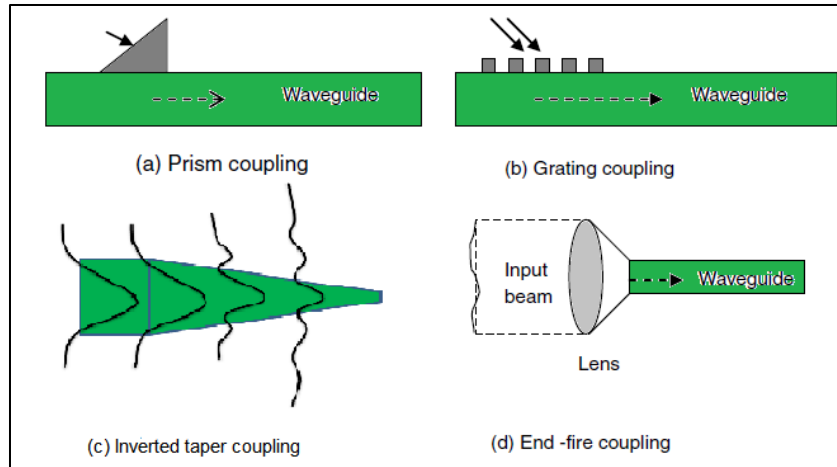


Fig. 2.12 Various methods of coupling light from the fiber to waveguides: (a) prism coupling; (b) grating coupling; (c) butt coupling; and (d) end-fire coupling [49].

2.6.1 Grating Couplers

The most common solution to the coupling problem is the grating coupler: a diffraction grating is designed such that all the scattered contributions interfere constructively in a vertically radiated wave that is as much as possible fiber-matched. This is shown in Fig. 2.13.

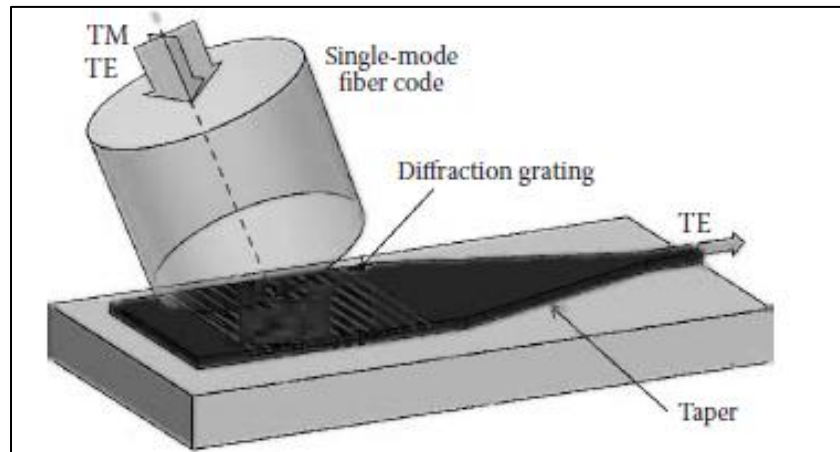


Fig. 2.13 Light from a semi-vertical optical fiber is diffracted by a grating coupler into an optical waveguide [57].

A grating coupler consists of a periodic refractive index modulation in or close to the waveguide core. Grating couplers are most often implemented as etched grooves in the silicon waveguide core [58,59]. Every such groove acts as a scatterer. Other ways to implement a refractive index grating is by adding metal lines [60] or etching subwavelength features that act as an effective medium [61,62]. When light is incident from the waveguide on the chip, some combinations of wavelength, grating period, and off-chip angle will cause all scattered contributions to be in phase, and thus a coherent phase front radiates away from the chip. This condition called the *Bragg* condition, illustrated in Fig. 2.14a, occurs when the phase delay between the diffraction of two adjacent grating teeth is exactly 2π (or a multiple thereof). For the directions where this phase condition is not met, the contributions of all the grating grooves will interfere destructively. An alternative way of calculating the operating condition for a grating coupler is in k-space, shown in Fig. 2.14b. A periodic structure like a diffraction grating carries its own impulse $K = 2\pi/\Lambda$, which can be transferred to the photons in the waveguide. The conservation of momentum in the z -direction therefore dictates that $k_z = \beta + mK$ ($m = 0, \pm 1, \pm 2 \dots$).

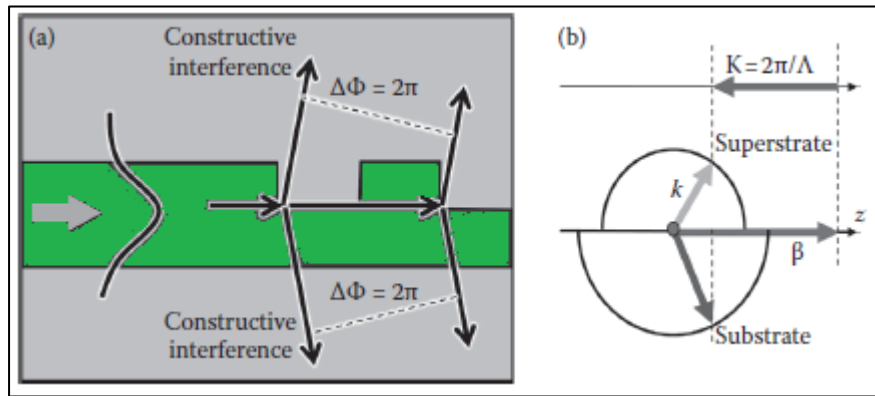


Fig. 2.14 Operational principle of a grating coupler. (a) Phase fronts in real space and (b) k-vector diagram [57]

As shown in Fig. 2.14b, there is a solution for $m = 1$. While in the out-of-plane direction, the nonperiodic structure of the waveguide does not pose any restrictions, except that the magnitude of the k -vector in the top and bottom cladding should match $k = n_{cl}k_0$. For light from the waveguide, there are in general two solutions: an upward and a downward radiating wave. The respective angles of these waves depend entirely on the material index of the top and bottom cladding material. The fact that there are two solutions poses a problem for the coupling efficiency: somehow, the light must be forced into the direction of the fiber, and not the substrate.

2.6.2 The Taper Coupler

The taper coupler is based on the principle that a waveguide which is below cutoff transfers energy into radiation modes. Because of the large mode mismatch between a strip mode and a slot mode, the two cannot be directly coupled. A strip-to-slot waveguide taper coupler must therefore be used to inject and extract light into and out of a slot waveguide. Tapers reduce the coupling loss by an adiabatic modal transformation. Essentially there is a gradual, smooth, and lossless transition from a large cross-sectional waveguide area to a smaller one. The angle of the taper should be very small to achieve the smooth transition, and the surface roughness should also be as small as possible. Specifically, the fundamental TE mode of the strip waveguide couples into the TE slot waveguide mode adiabatically [63]. It is necessary that there should not be any coupling between the fundamental mode and higher order modes, if any, and between the propagating fundamental mode and the radiation modes into the substrate. The usual design approach is to obtain the pattern of the

propagating fundamental mode as a function of the taper length L_T using a beam propagation tool. For the taper to be adiabatic, the length scale over which its width varies should be long compared to the beat length between the fundamental mode and the nearest mode in the effective index, to which the fundamental mode can couple [64]. The condition can be derived by considering Fig. 2.15.

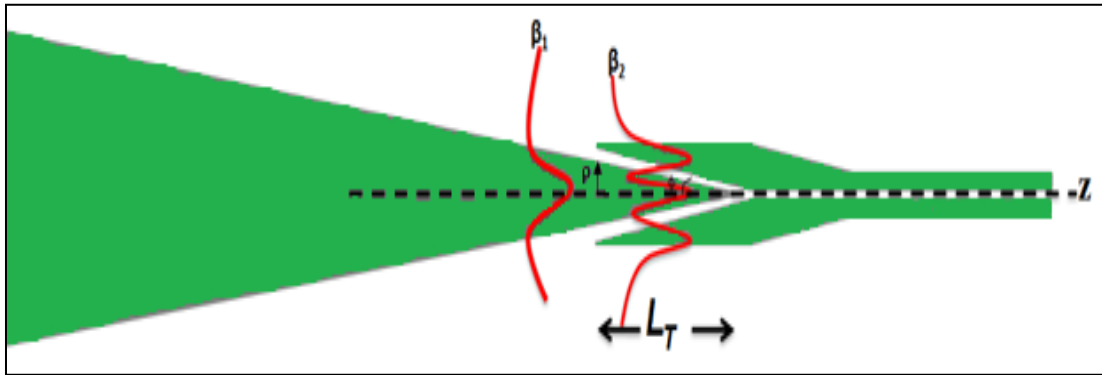


Fig. 2.15 A strip-slot waveguide taper coupler

The waveguide half width at a point z along the taper is denoted by $\rho(z)$; the propagation constants for the fundamental and unwanted modes, that may be coupled, are respectively, β_1 and β_2 . The beat length between the modes is given by [49]

$$L_B = 2\pi / (\beta_1 - \beta_2) \quad (2-65)$$

The length scale over which the taper width is changing is $[\rho / (d\rho/dz)]$, and to satisfy the condition for achieving an adiabatic taper, this length scale should be much larger than the beat length. Therefore [49]

$$\rho / (d\rho/dz) \gg L_B \quad (2-66)$$

The local taper angle must satisfy the relation [49]

$$\Phi = d\rho/dz \ll \rho/L_B \quad (2-67)$$

In the region of the strip-slot waveguide taper coupler, which is shown in Fig. 2.15, light propagates along the taper from the strip to the slot waveguide; the optical mode will spread out of the strip waveguide, forming a similar mode profile of the slot waveguide in the two gaps between the two complementary tapers. Since these two gaps and the slot waveguide form a slot Y branch, which is helpful for mode converting, it is important to optimize the fabrication process to make sure that the Y branch is well shaped [65]. For example, the electric field distribution of the TE fundamental mode propagating along the taper is shown in Fig. 2.16, for $\lambda=1.55 \mu\text{m}$. At the origin ($z = 0$), the optical mode is well confined in the core of the taper. At a certain position for which the taper width is $\rho(z)$, the optical mode starts to be less confined in the core of taper, and a major part of the energy of the mode is localized in the cladding of taper. The mechanism is as a result of decreasing the width of the inverted taper along its length, the actual effective index of the TE fundamental mode is shifted lower than the effective index of the TE fundamental mode at the origin of the core of the taper. In other word, it becomes close to refractive index of the cladding and more close when the width is keeping decrease. So, the optical mode is expanding evenescently from core along the propagation direction. If the taper is sufficiently adiabatic (L_T large enough), it is achieved 100% efficient conversion between the optical mode at the origin and the optical mode at the inverted taper tip w_t [66].

The keys are to choose both optimal tip width (w_t) and taper length (L_T) for which the optical mode at the inverted taper tip is matching enough to the new mode, assuring that the mode conversion along the taper length is achieved efficiently.

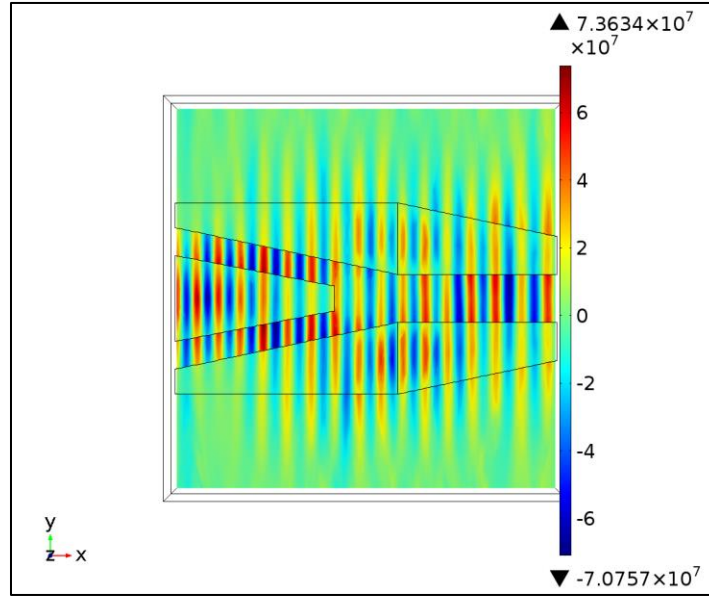


Fig. 2.16 E-field distribution (V/m) of the TE fundamental mode propagating through the SOI inverted taper shown in Fig. 2.15 for $\lambda=1.55 \mu\text{m}$.

2.6.3 The Coupling Efficiency

The principal characteristics of any coupler are its efficiency and its mode selectivity. Coupling efficiency is usually given as the fraction of total power in the optical beam, which is coupled into (or out of) the waveguide. Alternatively, it may be specified in terms of a coupling loss in dB. For a mode-selective coupler, efficiency can be determined independently for each mode, while multimode couplers are usually described by an overall efficiency. However, in some cases it is possible to determine the relative

efficiencies for the various modes of a multimode coupler. Thus, the basic definition of coupling efficiency is given by [45]

$$\eta_{cm} \equiv \frac{\text{power coupled into (out of) the } m\text{th order mode}}{\text{total power of optical mode prior coupling}} \quad (2 - 68)$$

If the power in each mode cannot be separately determined, overall values of η_{cm} is used. Coupling efficiency depends most strongly on the degree of matching between the fields of the optical coupled modes.

Chapter Three

Practice and Simulation in Silicon-on-Insulator Slot Devices

3.1 Introduction

An array of 200 SOI slot waveguide devices of varying slot widths, ribs widths, taper lengths and slot lengths were fabricated in each cell of a wafer fabricated at a commercial foundry. The cells were cleaved into individual chips after fabrication. Some chips were coated with thin films of polymers that fully infiltrated the slots. Measurements that consisted of spectral loss were made on the grating coupler waveguide devices of both coated and uncoated chips. Several SOI ridge devices were tested in purpose of de-embedding the effect of the grating couplers. A commercial software program was used to simulate each of the structures that was included in the 200 device test in order to describe the parameters which contribute in specifying the performance of each device or structure. In this chapter, the layouts of slot and ridge devices structures, some details about the fabrication process, as well as to the measuring setup are explained. Then the simulation methods which for modes solving and simulation the propagation light through the slot devices in 2D and 3D are given.

3.2 Structures Layouts

Figure 3.1a shows a general layout for the grating coupler waveguides devices which were used in order to test SOI slot devices in this work. Each of these devices starts and ends with grating couplers due to couple light from and into single-mode fibers. Next the input grating coupler, there is a short strip waveguide, 25 μm length, of Si ($n=3.49$) with $(10 \times 0.22) \mu\text{m}^2$ cross section to keep the mode size compatible between the fiber and a guiding element in PICs. Then the strip waveguide tapers in linear inverse shape to form a taper mode convertor that works to reduce the mode size from $(10 \times 0.22) \mu\text{m}^2$ to $(0.45 \times 0.22) \mu\text{m}^2$ cross section along 500 μm . Here, a strip-slot taper coupler region [8], or an overlap region between strip and slot, starts where the waveguide keeps tapering from $(0.45 \times 0.22) \mu\text{m}^2$ to $(0.13 \times 0.22) \mu\text{m}^2$ width along a taper coupler length L_T and it is sandwiched between two Si ribs in (V) shape with small gap between the tapered waveguide and each rib. In the geometry of the taper coupler, as shown in Fig. 3.1b, and for more efficient coupling, the Si ribs extend along L_T with increasing in their width by the inner side only, trying to couple all light in Si ribs, and beyond a few μm s from L_T their width is decreased by the outer side along 30 μm in order to couple all light in the slot, as will be shown later. Then they continue with constant size at each rib, $(0.22 \times w_r) \mu\text{m}^2$, to configure the slot waveguide with slot size $(0.22 \times w_s) \mu\text{m}^2$, and slot length L_s . Since all devices are symmetric, all these sections are repeated in opposite direction at the output end, as shown in Fig 3.1. All these segments in all structures have been made on SiO_2 layer ($n=1.44$) with height $h_{\text{SiO}_2} = 2 \mu\text{m}$. Furthermore, some of the SOI devices are uncoated and some of them coated with Polyimide (PI) polymer layer ($n=1.7$) with height $h_{\text{PI}} = 0.5 \mu\text{m}$.

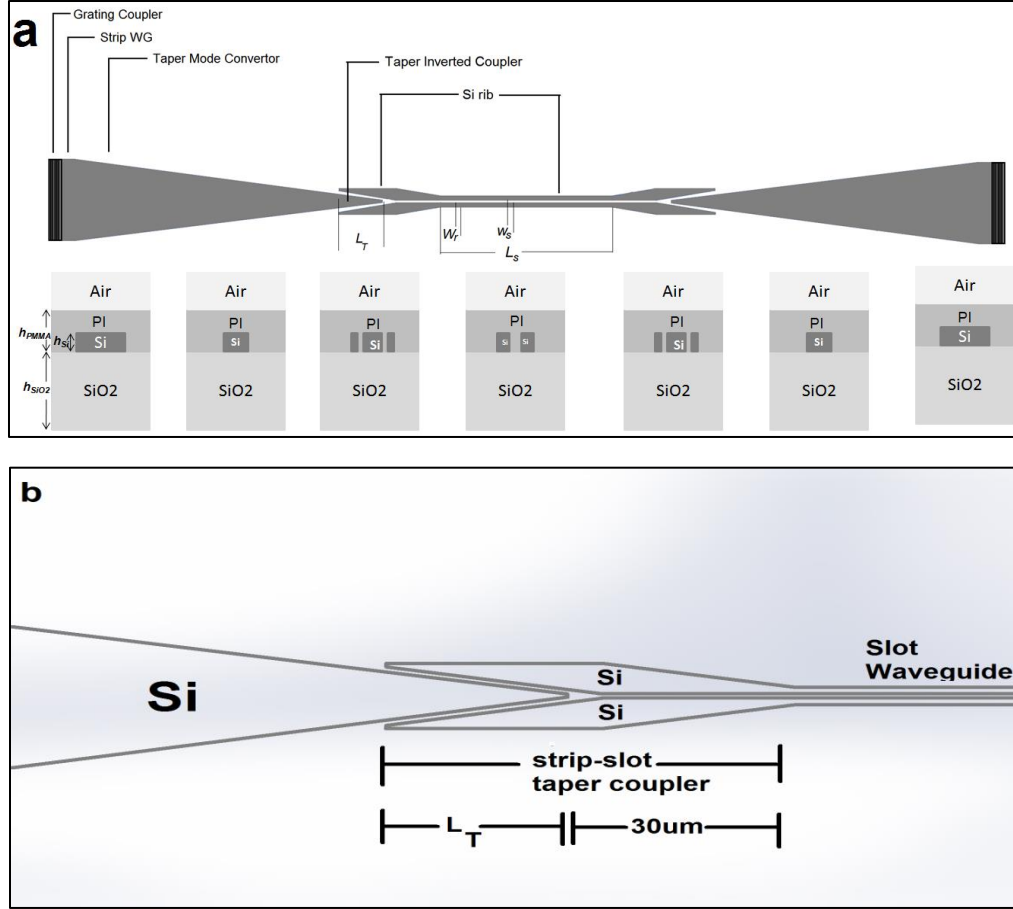


Fig. 3.1. (a) The layout of the slot device from the input grating coupler to the output one and cross sections for the structure at different points (b) geometry of strip-slot taper coupler

Several of SOI ridge devices, with size $0.45 \times 0.22 \mu m^2$ and different lengths, are designed, as shown in Fig. 3.2, fabricated and tested. These ridge devices have been tested using the grating couplers waveguides configuration same as slot devices. The size of the ridge waveguide were made in order to keep the single-mode guiding through it without radiation and with loss as low as possible. The measurements of these devices were used to de-embedding the influence of the grating coupler, as will be shown in a later section. As in slot devices, there are coated ridge devices, with polymer.

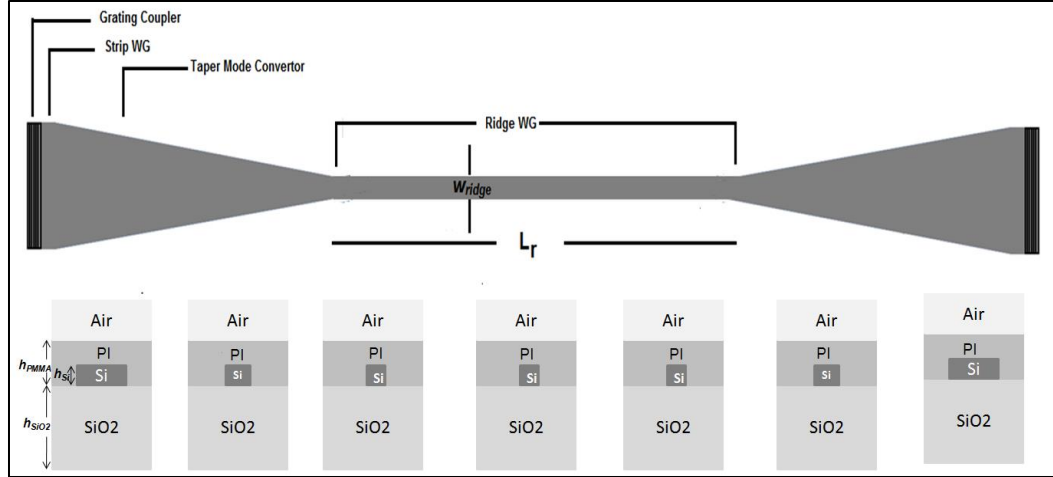


Fig. 3.2. The layout of the ridge device from the input grating coupler to the output one and cross sections for the structure at different points.

3.3 Fabrication

All slots and ridges devices used in this study are fabricated on a 200-mm-diameter SOI wafer with an IMEC 193 nm deep ultra-violet (UV) lithography process. The functional layers of the wafer are comprised of a 220 (± 3.5) nm crystalline silicon layer on top of a 2 μm buried silicon oxide layer. The silicon oxide layer is sufficiently thick to reduce optical leakage through the substrate. A 500 nm polymer coating is deposited after the wafer is fabricated. The polymer used is a photo-definable polyimide (HD-8820) from MicroSystems. Scanning electron microscopic (SEM) images of sections of fabricated devices are shown in Fig. 3.3. As can be seen in this figure, a little roughness appears on the sidewalls of each Si rib whatever its width is. Their sizes are estimated about 5 nm. The roughness sizes are small compared to slot dimensions; but its effects on guiding properties and propagation loss might be significant.

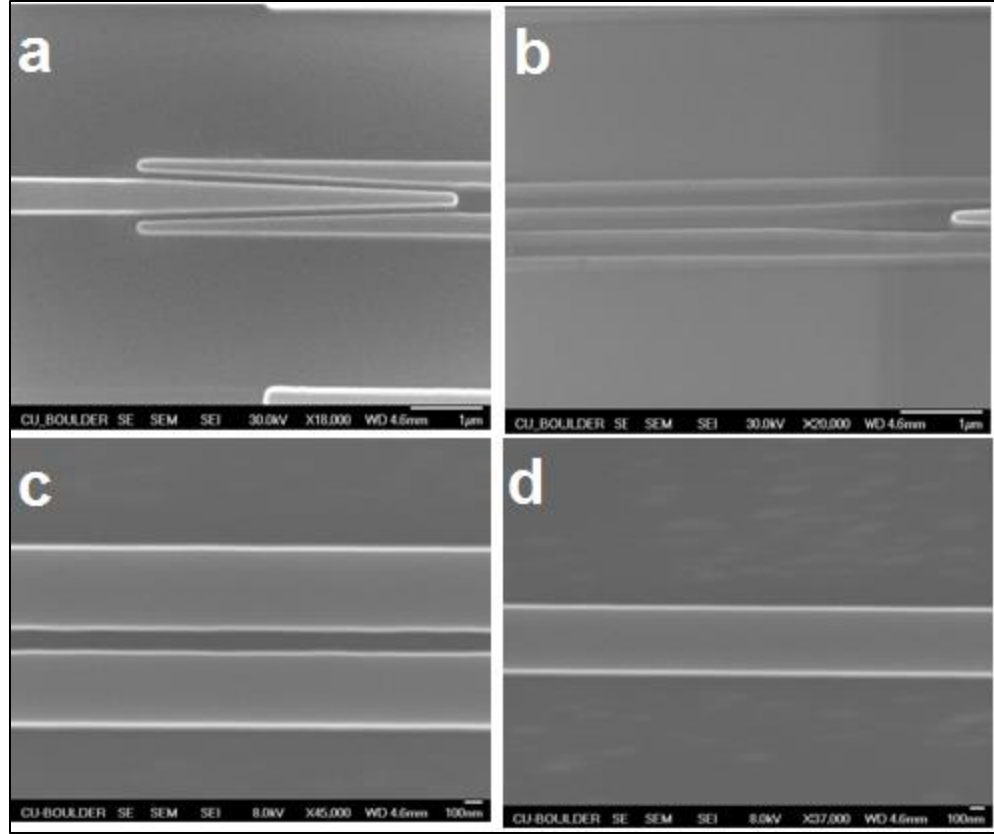


Fig 3.3 SEM images for (a) the strip-slot taper coupling region (b) a tip of taper in face of a slot waveguide (c) a slot waveguide (d) a ridge waveguide

3.4 Measuring setup

All the device measurements were carried out in-house using the apparatus depicted in Fig. 3.4. The system employs a broadband SLED light source whose wavelength range is 1500-1600 nm. The photonic chip is placed on a temperature controlled sample stage. A single mode fiber delivers the light signal to the photonic chip where light is coupled into device through a grating coupler located at one end of each device. The grating coupler is optimized for passing TE modes where E-field is parallel to the grating grooves.

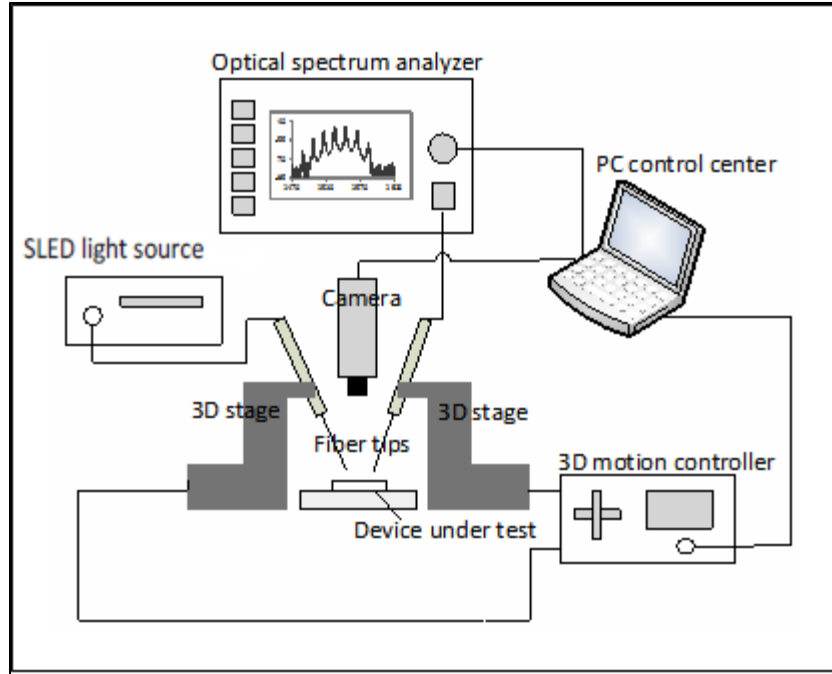


Fig 3.4 Schematic of the in-house measurement setup. The setup is comprised of a SLED light source, an optical spectrum analyzer, two single mode fibers that couple light to and from the photonic chips, two sub-micron accurate 3D motion controllers, a visible camera that monitors the fiber movement and a temperature controlled sample stage.

After passing through the device, light is coupled out through another TE-mode grating coupler into an optical spectrum analyzer (OSA) via the second single mode fiber. The maximum resolution of the OSA is 80 pm throughout the wavelength range of 600-1700 nm. The fiber movements are precisely controlled by two 3D motion controllers which are capable of sub-micrometer adjustment. A visible camera is used to monitor the movement of the two fiber tips. Two probes are used to apply electrical signals to the photonic chip where necessary. Figures 3.5 and 3.6 display the physical image of the setup in the lab. All 200 slot devices with varied slot width, slot length, taper length, and overlap length were tested. Measurements were taken with polymer coatings and without. Calibration ridge waveguides were used to de-embed the effect of the grating coupler and ridge sections from the slot section measurements.

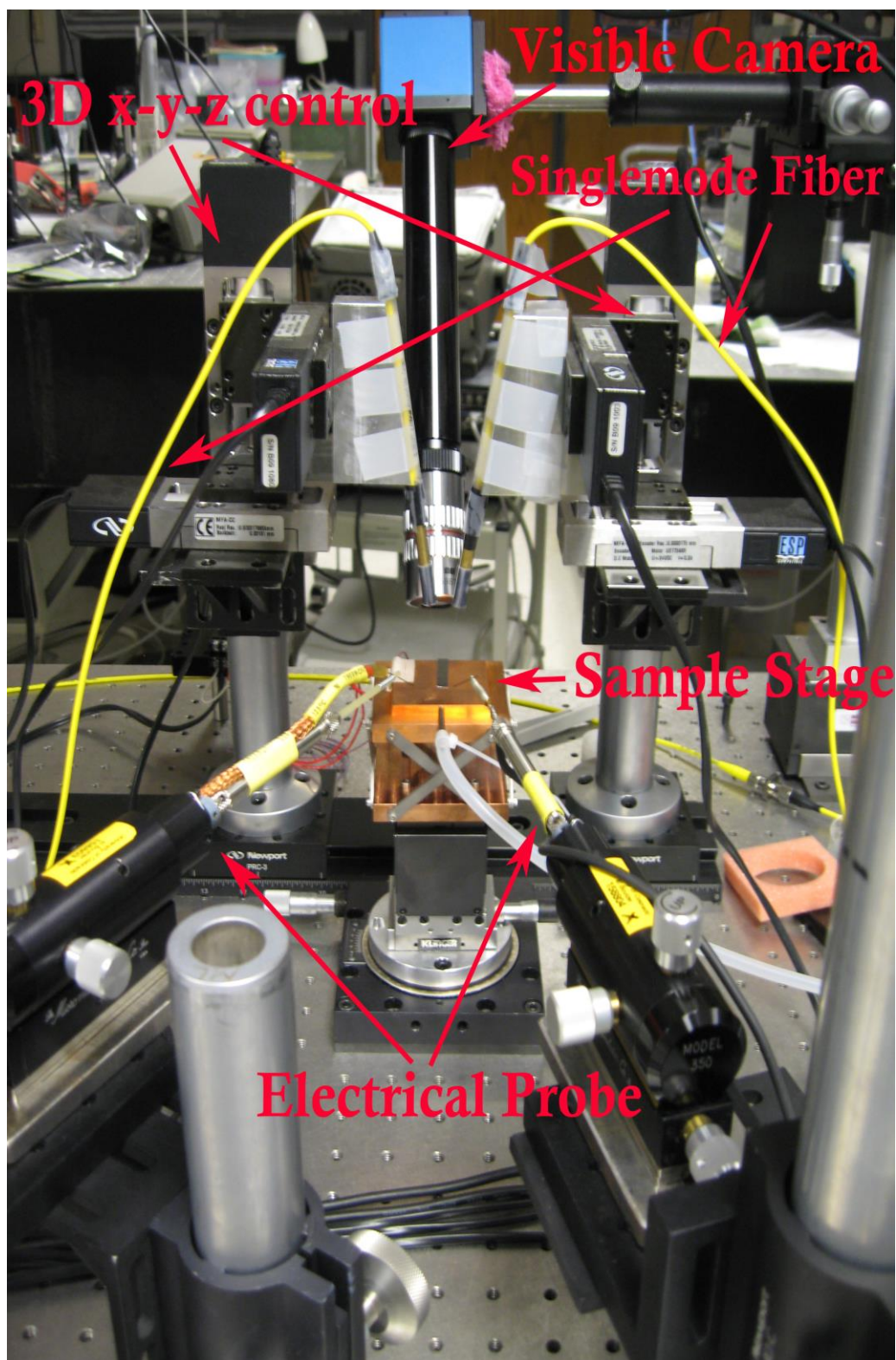


Fig. 3.5 Image of the experimental setup.

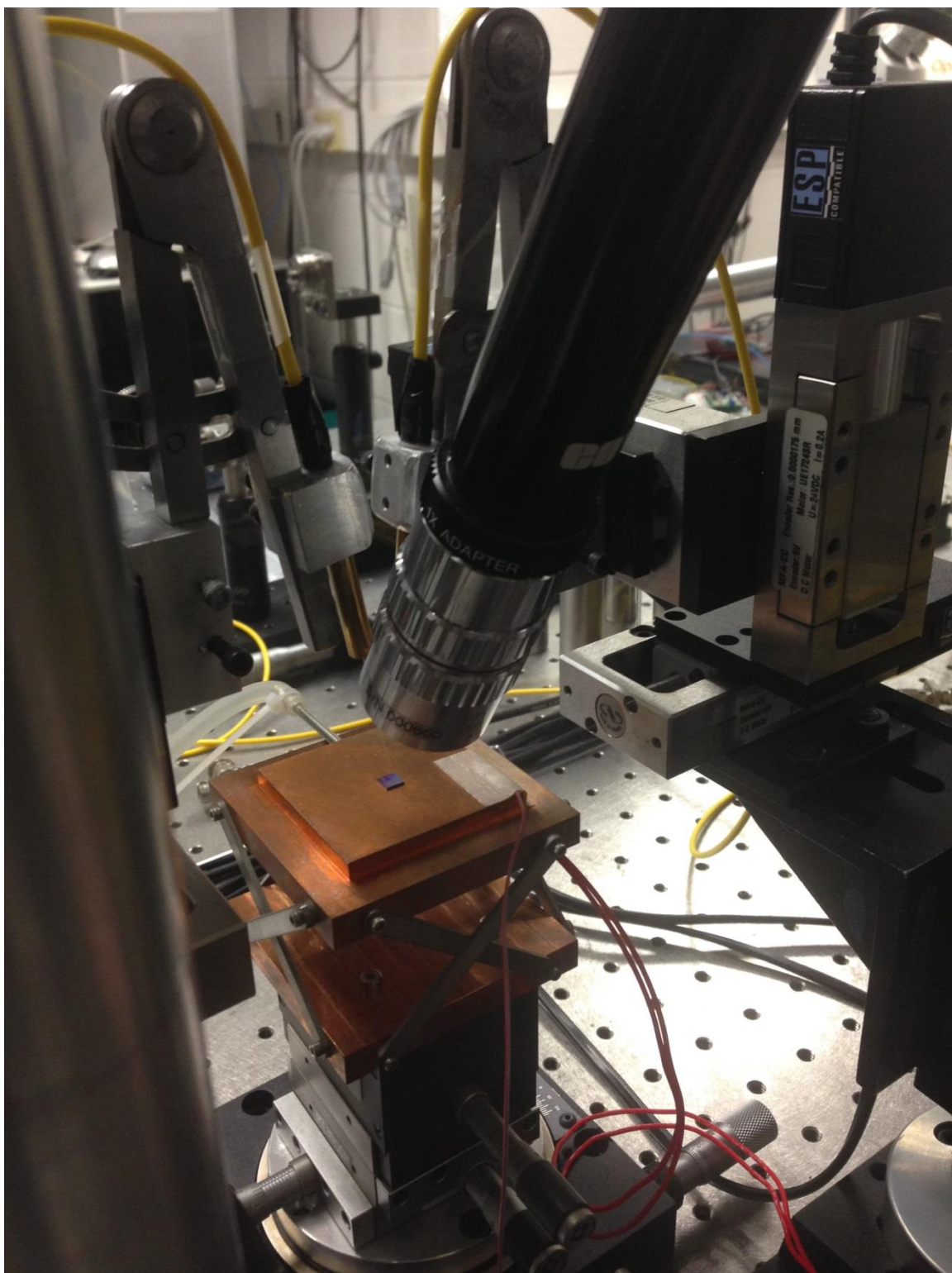


Fig. 3.6 An image of the experimental setup with more focus on the sample stage, coupling fibers, and monitor camera.

3.5 De-embedding Measurements

The transmission light, at a given wavelength and polarization, through the whole device in Fig. 3.1 suffers losses which can be contributed by three regions; grating couplers regions, tapered coupler regions, and a slot waveguide region. The effect of grating couplers and mode convertors is de-embedded experimentally by compare the transmission of each slot device with the transmission of an ultra-low losses ridge device with identical grating couplers and tapered mode convertors with slot devices as shown in Fig. 3.7.

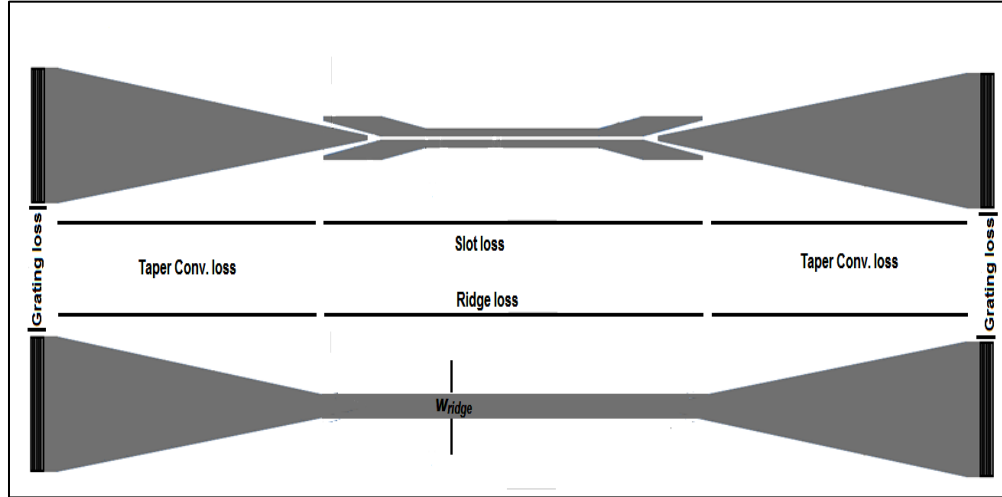


Fig. 3.7 Losses regions along slot (up) and ridge (down) devices.

Both of slot and ridge are passive devices and there is no gain energy can be obtained by the propagation through them [57]. Therefore, the output power of the slot devices in Fig. 3.1 can be estimated as

$$P_{out} [\text{dBm}] = P_{in} [\text{dBm}] - (2 \int_{grating} [\text{dB}] + \int_{slot} [\text{dB}]) \quad (3-1)$$

where P_{in} is the incident power on the grating coupler from a single-mode fiber, $\int_{grating}$ is all losses at each grating coupler, and \int_{slot} is all losses along the slot waveguide region. While the output power of the ridge device is

$$P'_{out} [\text{dBm}] = P_{in} [\text{dBm}] - (2\int_{grating} [\text{dB}] + \int_{ridge} [\text{dB}]) \quad (3-2)$$

where \int_{ridge} is the loss along the ridge waveguide that can be estimated by finding the propagation losses through the ridge which is expected to be very low, it is about 1- 2 (dB/cm) [20]. According to that, Eq.(3-1) and (3-2) can be solved instantaneously and the loss of the slot waveguide region can be obtained. Furthermore, transmission measurements for many ridge devices with different ridge length (L_r) is compared in order to evaluate the ridge loss and if it may add some values. Figure 3.8 shows the measured transmission of three ridge devices with three different lengths over spectral width 100 nm.

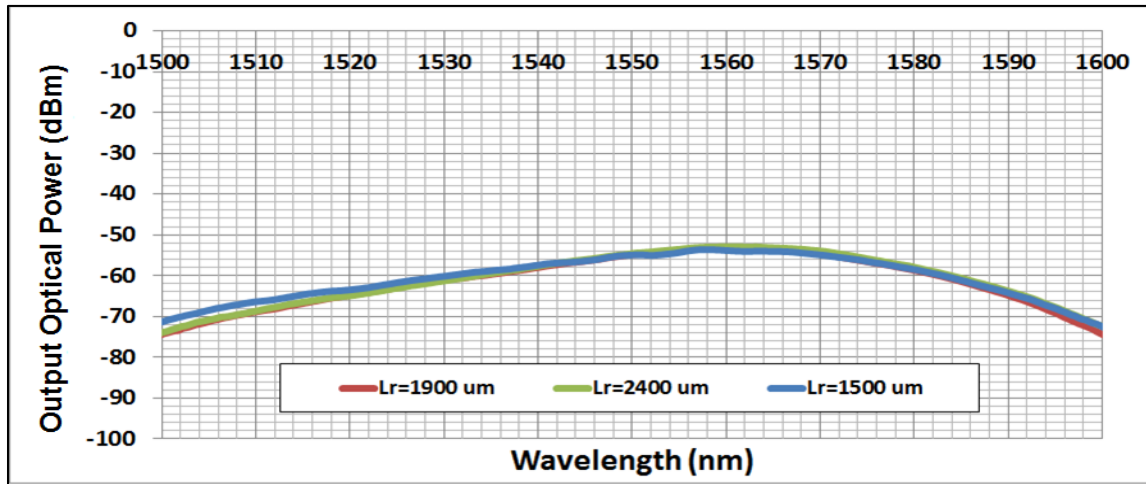


Fig. 3.8 The measured output optical power of three ridge waveguide devices with cross section $0.45 \times 0.22 \mu\text{m}^2$ and ridge length $L_r = 1500$ (blue), 1900 (red), and $2400 \mu\text{m}$ (green).

The slot waveguide losses involve the coupling loss and the propagation loss. Whereas the coupling loss represents the fraction of the total power in the fundamental mode which is not coupled into (or out of) the slot waveguide, the propagation loss is resulted from the absorbed, scattered or radiated power through the slot waveguide.

3.5 Simulation method

In the simulation part, a commercial software program, FimmWaveTM (from PhotonDesign, UK) has been used to simulate each of the structures that was included in the 200 devices test. The simulation was done for each of the structures as strip-slot-strip waveguides without involving the grating couplers. The impossibility of simulating the whole structure results from incompatibility of 2D simulation, which is required for grating couplers, with 3D one which is used for the waveguides devices. For this reason the measurement results were calibrated by using transmission results of ridge waveguides. This tool aims to solve modes across any section of the slot or ridge device, as well as to simulate the optical wave propagation in waveguides. In all simulation cases, whether it is mode solving or optical propagation, the wavelength is set at 1550 nm with a quasi-TE polarization.

3.5.1 Mode Solving

This tool is using a fully vectorial solver based on the Film Mode Matching (FMM) analysis, which is perfect solver for both slot and ridge waveguide with rectangular geometry. The FMM method models an arbitrary waveguide by a list of vertical slices, each uniform laterally, but

composed vertically of a number of layers. FMM solver is used to find the modes of a polarization-independent structure. The mode profiles for the fundamental quasi-TE and quasi-TM modes are plotted below in Fig. 3.9.

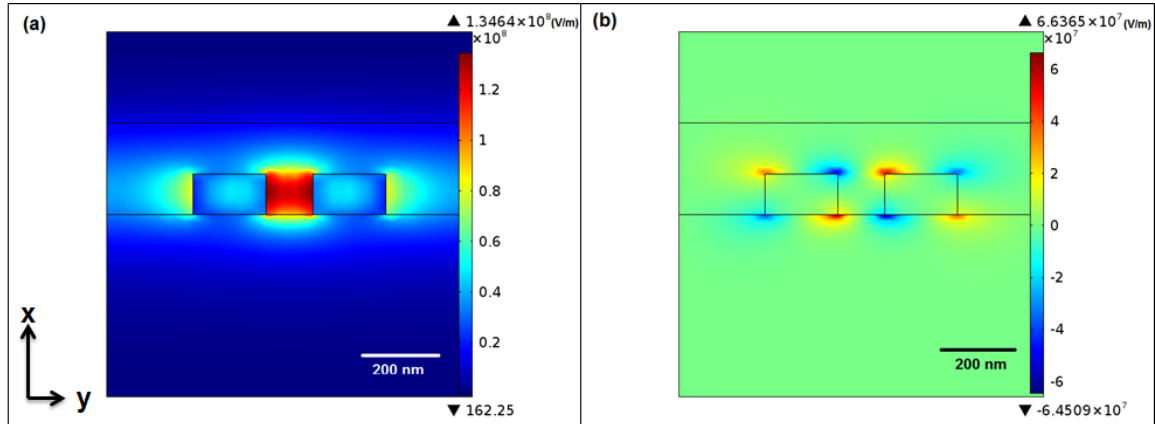


Fig. 3.9 The electric field profile of (a) the fundamental quasi-TE mode (b) the fundamental quasi-TM mode across SOI slot waveguide with $w_s=0.13\mu\text{m}$, $h=0.22\mu\text{m}$, $w_r=0.2\mu\text{m}$ at 1550 nm.

A wide range of parameters can be calculated for each mode, including the effective index, group index, mode dispersion and confinement factor. All these parameters can be scanned with varying geometry of the waveguide, allowing fine-tuning the design of the SOI devices for specific purposes. Mode profiles can be taken across any section along any simulated SOI device, as shown in Fig. 3.10, thus coupling and propagating modes can be monitored along the slot device. Also, 1D plots of quasi-TE modes across ridge and slot waveguides, which represent profiles for the set equations which were presented in Chapter Two, can be done by the simulation and they can be used to analyze the single mode condition and the relation between the confinement factor and device dimensions, as shown in Fig. 3.11.

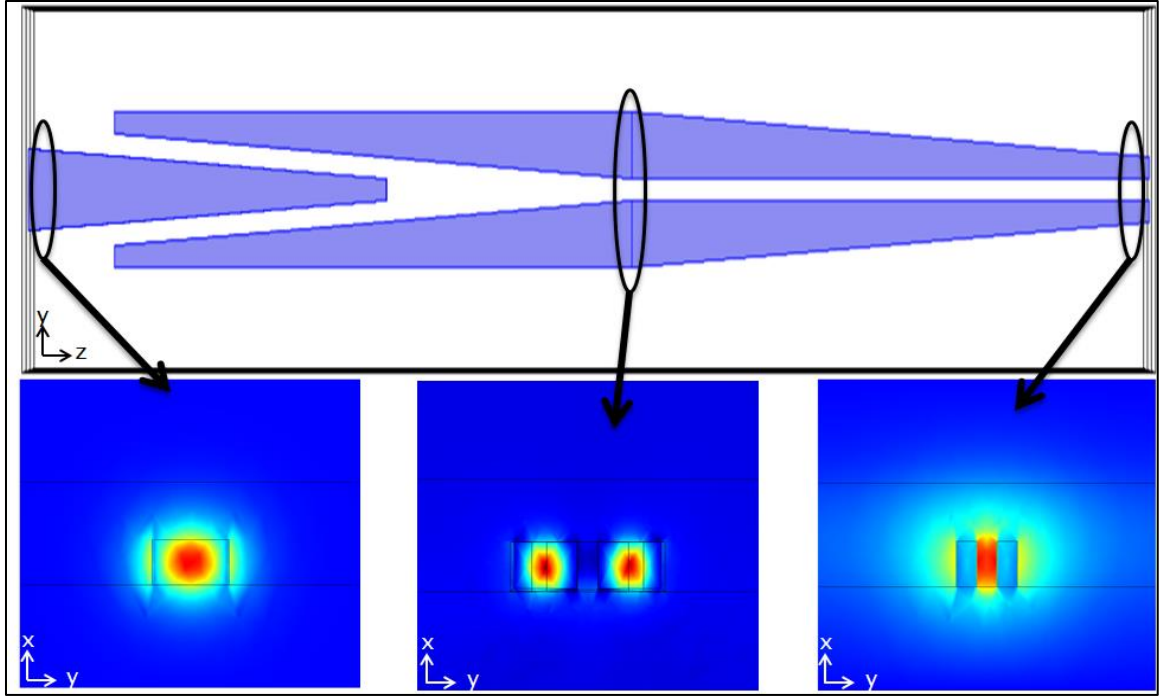


Fig. 3.10 The electric field norm profile of a quasi-TE mode along a strip-slot coupling regions at 1550 nm wavelength.

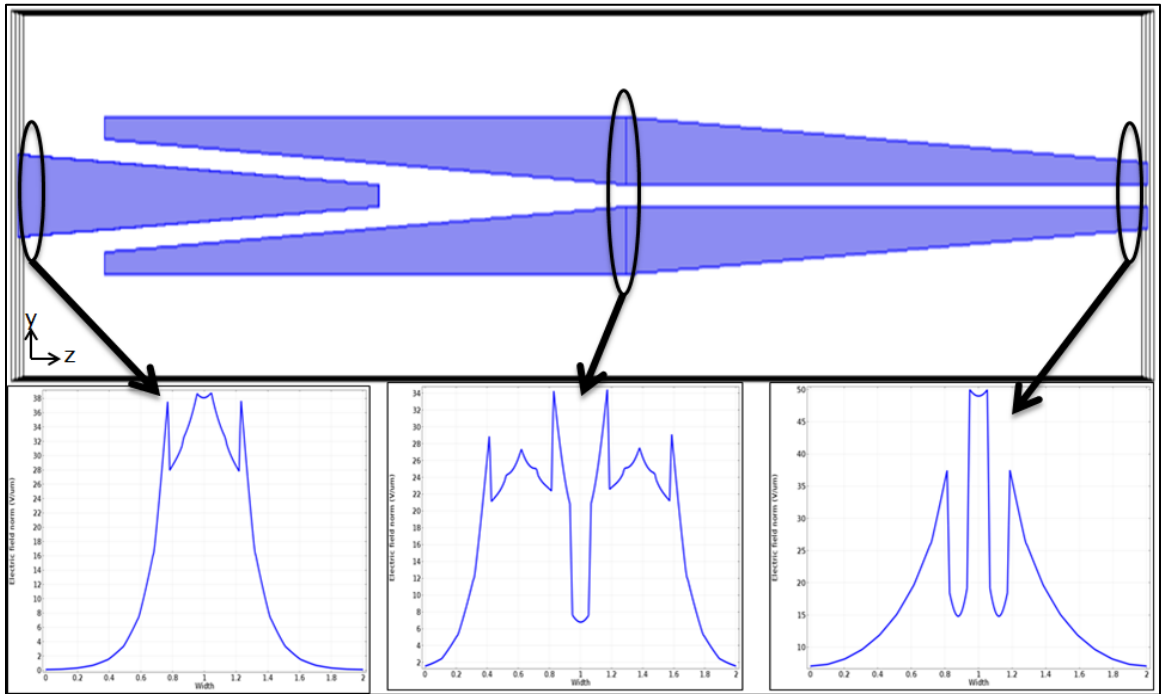
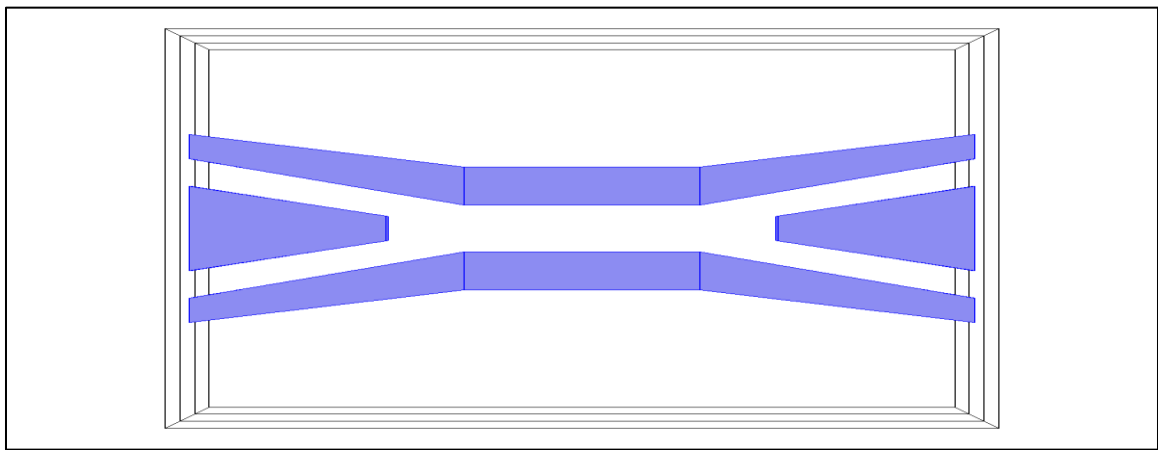


Fig. 3.11 Electric field norm, of quasi-TE mode, distribution along width of the structure across strip-slot coupling regions at 1550 nm.

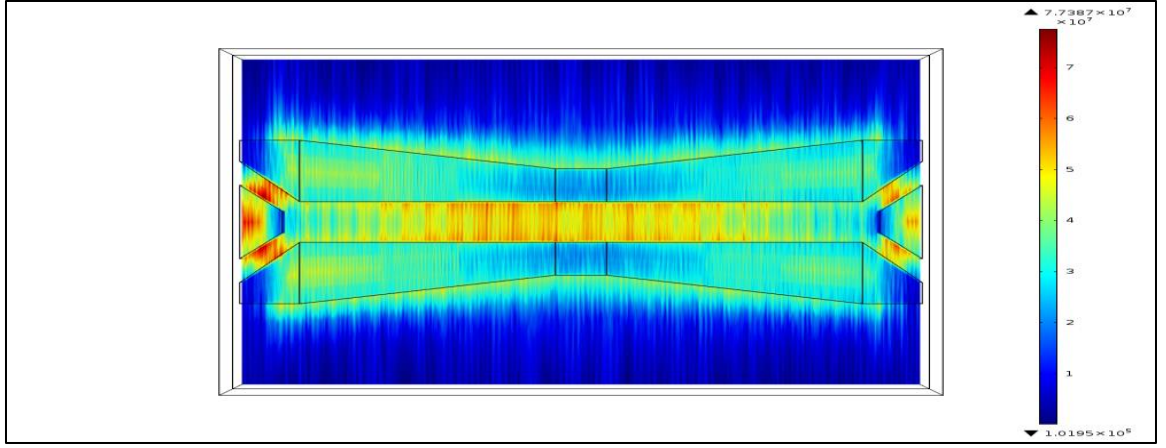
3.5.2 Optical wave propagation

On the other hand, the same software program is used for simulating the optical propagation in waveguides devices in 3D and it is fully integrated with the mode solver where it relies on the Eigen Mode Expansion (EME) which is a rigorous and highly efficient method [67, 68]. The transmission loss of any simulated device which is reported by simulation includes the inherent loss along the device and the insertion, or coupling loss, at the input and output of the slot assuming ideal smooth surfaces. Figure 3.13 shows a simulated optical propagation via an SOI slot device. In case of optical propagation under effect of the surface roughness, the scattering loss, which is caused by surface roughness, is estimated by Eq(2-63) and involved in the simulation. Notice that the scattering loss is estimated for surface roughness magnitude about 5nm whereas the required effective indices are found by FMM solver. As an example, Fig. 3.12 shows the optical propagation of the electric field norm of quasi-TE mode through a slot device with different slot width $w_s = 0.13, 0.2$, and $0.25 \mu\text{m}$ and Si rib width $w_r = 0.2 \mu\text{m}$ at 1550 nm wavelength.

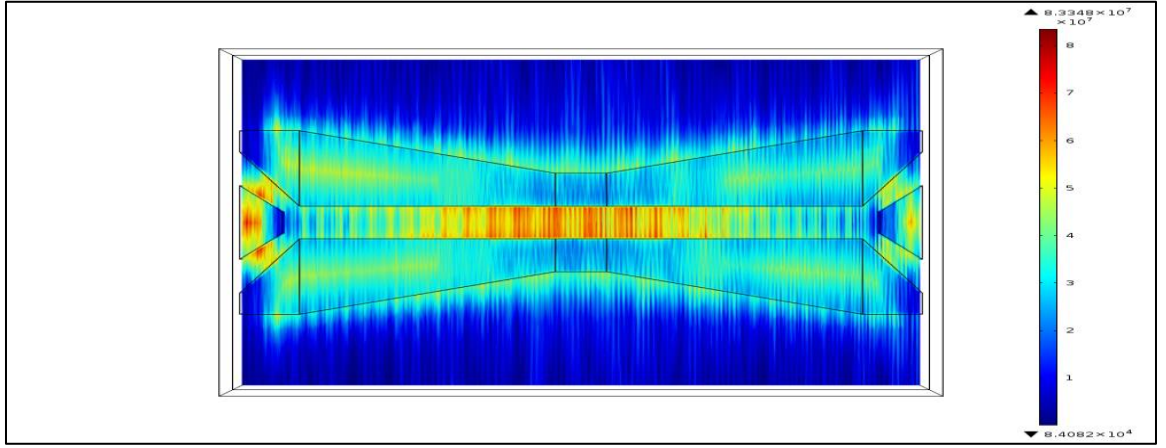


(a)

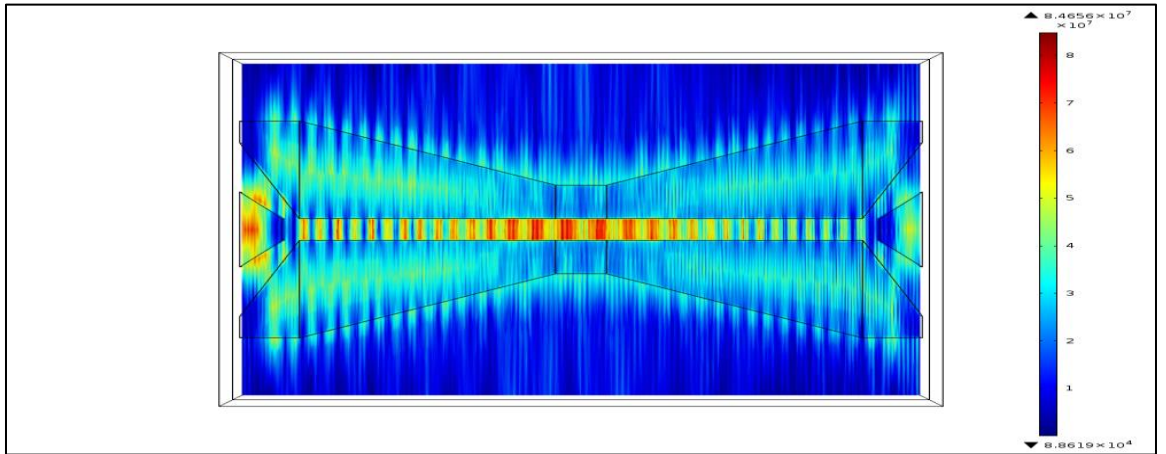
Fig. 3.12 to be continued



(b)



(c)



(d)

Fig. 3.12 (a) A general structure of a slot waveguide device with the simulation of the optical wave propagation through it at different slot width w_s ; (b) 0.13, (c) 0.2, and (d) 0.25 μm , at 1550 nm wavelength and TE polarization.

Chapter Four

Measurements, Results, and Discussion

4.1 Introduction

In this chapter, the room temperature measurements of the transmission of slot devices are presented. Analysis of these measurements and their simulated counterparts indicates that the transmission of a slot waveguide is controlled by; how much light will be coupled and uncoupled into and from a slot waveguide, or coupling loss, and how much light will be lost through it, or propagation loss. Regarding the coupling loss, although the high coupling efficiency of the strip-slot inverted taper coupler, that is used in this work, and beside the effected factors which were reported in [8], important roles may be played by other factors like; the slot waveguide geometry and the coating layer where they could affect the performance of the slot. On the other hand, due to the low absorption of Si strip and ribs [20] and the straight geometry of the slot device, the interface scattering loss is dominating the propagation loss more than the absorption and bending radiation losses. So several effective factors control the transmission losses, coupling and propagation, of the slot such as; the coating layer, slot

geometry, as well as the length of the taper coupler and the width of the taper width [8]. Here each of these factors will be discussed as an attempt to put a comprehensive analysis that explains the amount of effect of each these factors, and paves the way to an optimum design for a slot device whether as a guiding device or a functional device; modulator or switch.

4.2 Effects of The Coating Layer

As mentioned before, some chips were coated by a thin polymer layer with about 500 nm thickness whereas other chips were kept without coating. Experimentally, the transmission of each device has been measured as a grating coupler waveguide, as shown in Fig. 3.1, using measuring setup which was shown in Chapter 3, Fig.3.4 and 3.5. Each device has been tested over spectral width between 1500 and 1600 nm. Figure 4.1 shows the measured out optical power of coated and uncoated identical slot waveguides. Although that the coupling efficiency of the strip-slot taper coupler is wavelength independent [8] and same approach was reported regarding the out power of the slot waveguide in [3], an observed variation in the measured transmission with the operating wavelength is caused by the effect of the grating couplers where the measurements accuracy is limited mainly by fabrication non-uniformities of the grating couplers. Comparison the measurements of the devices with each other one shows that the coating layer enhanced the transmission by about $20\pm0.5\text{dB}$ at 1550 nm wavelength.

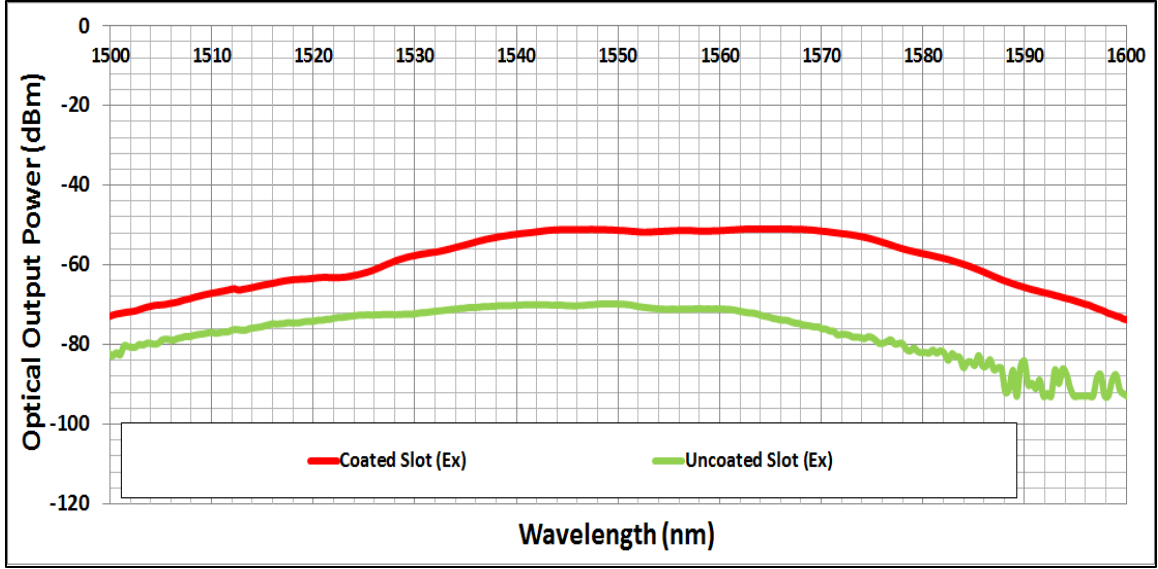


Fig. 4.1 The measured output optical power over 100 nm spectral width of coated (red) and uncoated (green), slot devices with 100 μm slot length, 0.12 μm slot width, and 0.12 μm each of Si ribs width

Theoretically, the propagation and coupling losses have been calculated by Eq. (2-62, 63, and 68) respectively. The FMM analysis based Fimmwave simulation was used for; (1) solve the quasi-TE mode, (2) find the effective index of this mode, and (3) the profile of its electric field component. The simulation and calculations found that the polymer coating layer enhanced the transmission of the tested slot devices by mainly decreasing the coupling loss and an observed change in the propagation losses, as shown in Fig. 4.2. The coupling loss decrease by 14.8 dB whereas the propagation loss decrease by 4.7 dB, at 1550 nm wavelength.

Table 4.1 shows the measured output optical power, the simulated scattering loss, and the simulated coupling loss of both coated and uncoated devices at 1550 nm wavelength.

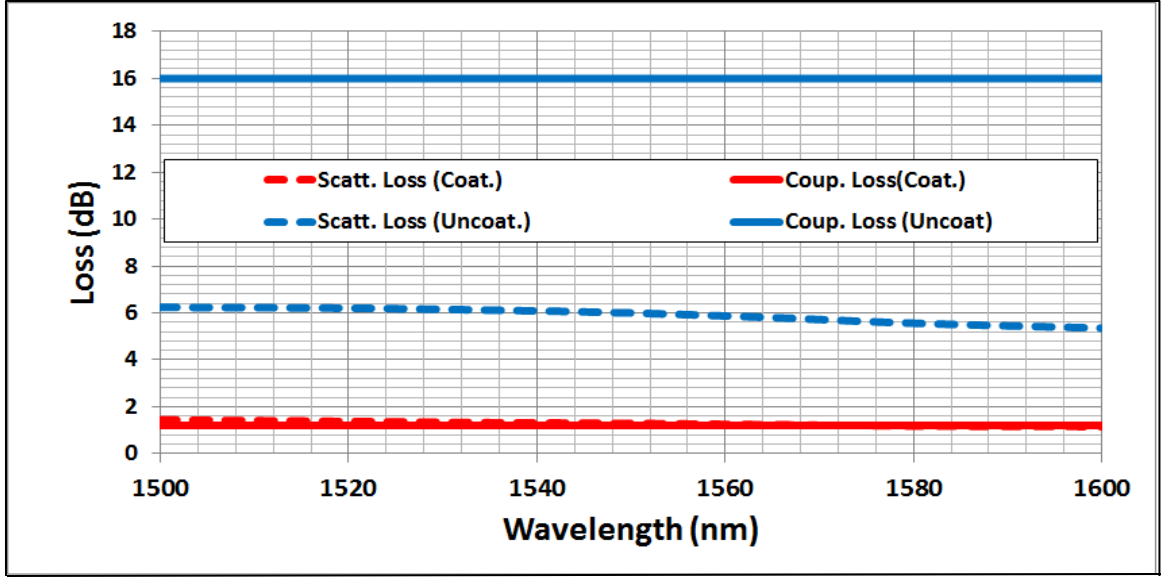


Fig. 4.2 The simulated scattering losses (Dashed), and coupling losses (Solid), for coated (red) and uncoated (blue) slot devices over 100 nm spectral width, 100 μm slot length, 0.12 μm slot width, and 0.12 μm each of Si ribs width.

Table 4.1 The measured output optical power, simulated coupling, and simulated scattering loss for coated and uncoated slot devices in Figs. 2.1 and 2, at 1550 nm wavelength.

	Measured Output Optical Power (dBm)	Simulated Scattering Loss (dB)	Simulated Coupling Loss (dB)
Coated Slot	-51 \pm 0.3	1.3	1.2
Uncoated Slot	-70 \pm 0.8	6	16

The propagation losses in optical waveguides include; the absorption loss, the interface scattering loss, and the bending radiation loss [43]. Both of the straight structure of the slot and the low absorption of coefficients of Si and Polymer [4] limit the bending and absorption losses while the scattering loss by the roughness of the sidewalls of the ribs becomes more dominated. According to Eq. (2-62), the scattering attenuation coefficient of a slot waveguide which is proportional with the square of the surface

roughness, the square of the difference between refractive indices of high and low-index regions, and the normalized electric field intensity at the waveguide sidewalls [54]. Increasing the index-contrast interfaces between the slot and ribs (as in case of air coated device) leads to increase the transverse electric field component, which is normal on the sidewalls, according to the discontinuity principle [3], as shown in Fig. 4.3a. This increasing means increase the normalized electric field intensity at interfaces, as shown in Fig. 4.3b, then increase the scattering loss coefficient.

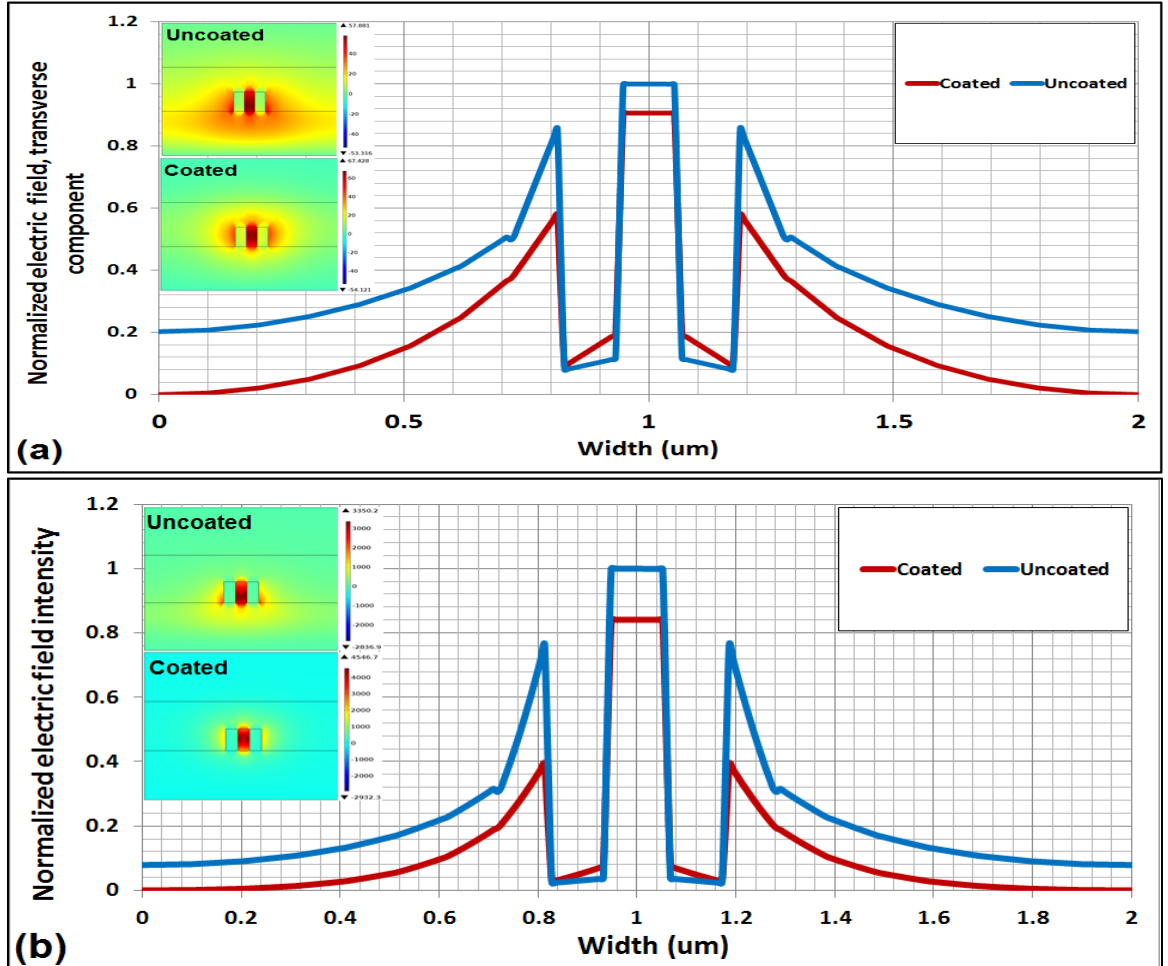


Fig. 4.3 The normalized (a) transverse electric field component (b) electric field intensity of the quasi-TE fundamental mode, for coated (red) and uncoated (blue) slot devices with slot width, $w_s=0.12 \mu\text{m}$ and Si rib width, $w_r=0.12 \mu\text{m}$, at 1550 nm wavelength.

It's clear from Eq. (2-62) that the scattering loss is decreased with long operation wavelengths in both case; coated and uncoated slots, where the surface roughness be less effect when its size amount be small compare with the operating wavelength. In the same time, the wavelength has other effect on the scattering coefficient through the effective index. Where the coefficient is increased with decreasing the effective index, also according to Eq. (2-62), as a result of increase the operation wavelength, according to Eqs. (2-60 & 61) as shown in Fig. 4.4. So the variation of scattering loss with the operation wavelength is very low.

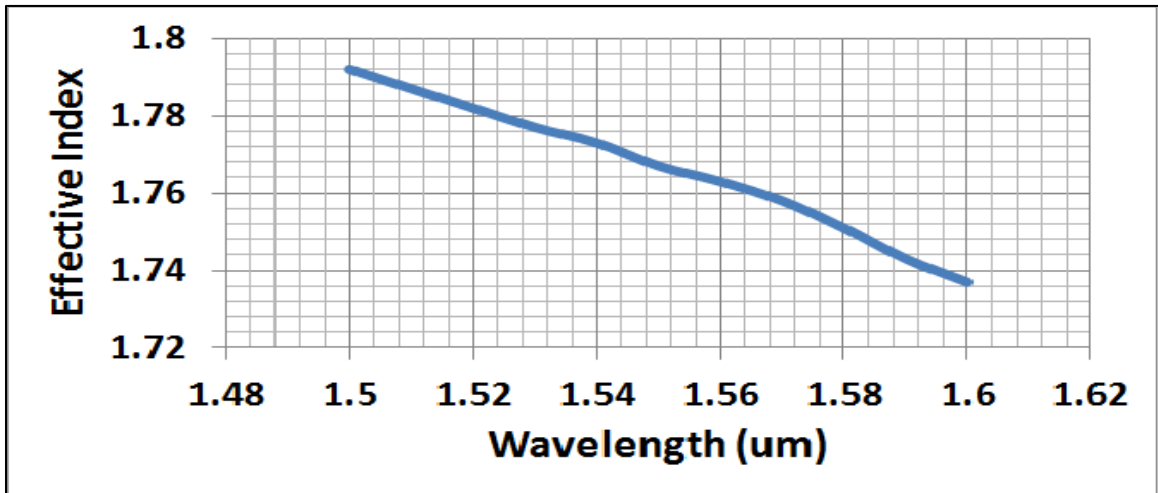


Fig. 4.4 The effective index of the quasi-TE fundamental mode vs. operation wavelength in slot waveguide with slot width, $w_s=0.2 \mu\text{m}$, Si rib width, $w_r=0.25 \mu\text{m}$ and thin film of polymer.

On the coupling side, though the increasing of the electric field inside the slot compare with Si ribs a large amount of this component will be gone outside the waveguide structure. Beside that and according to Eqs.(2-54, 56, and 58) the magnetic field component varies very slowly across the waveguide and parallel to the interfaces. With uncoated device, the magnetic

field dissipated in all waveguide regions so it will be decreased in the waveguide cross section as shown in Fig. 4.5.

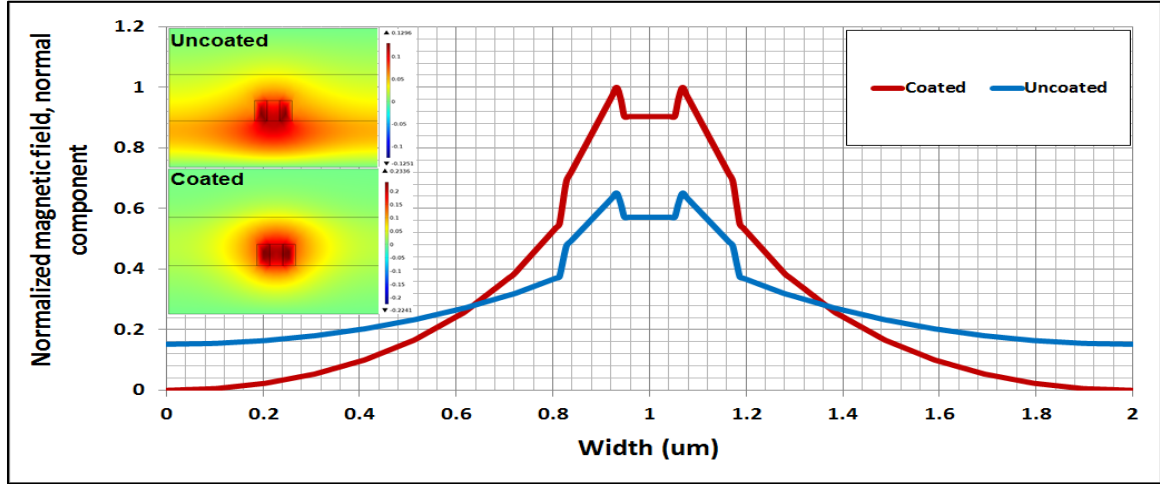


Fig. 4.5 The normalized magnetic field normal component of the quasi-TE fundamental mode, for coated (red) and uncoated (blue) slot devices with slot width, $w_s=0.12 \mu\text{m}$ and Si rib width, $w_r=0.12 \mu\text{m}$, at 1550 nm wavelength.

According to all that the coupled mode from the strip to the slot extend to oscillate in all regions of the waveguide structure results what is called substrate radiation mode [40]. The resultant effective index is between air and substrate refractive indices, so non-small fractions of the quasi-TE mode dissipates in the substrate and air. Figure 4.6 shows the coupling process of the optical power intensity of the quasi-TE mode via strip-slot taper coupler for both coated and uncoated cases, at 1550 nm wavelength. Also the coupling loss can be estimated at each side of the slot waveguide by Eq. (2-69). The difference of the coupled energy into coated and uncoated slot devices can be noticed in Fig. 4.7 that shows the optical power intensity distribution of the quasi-TE mode along device width, before and after coating.

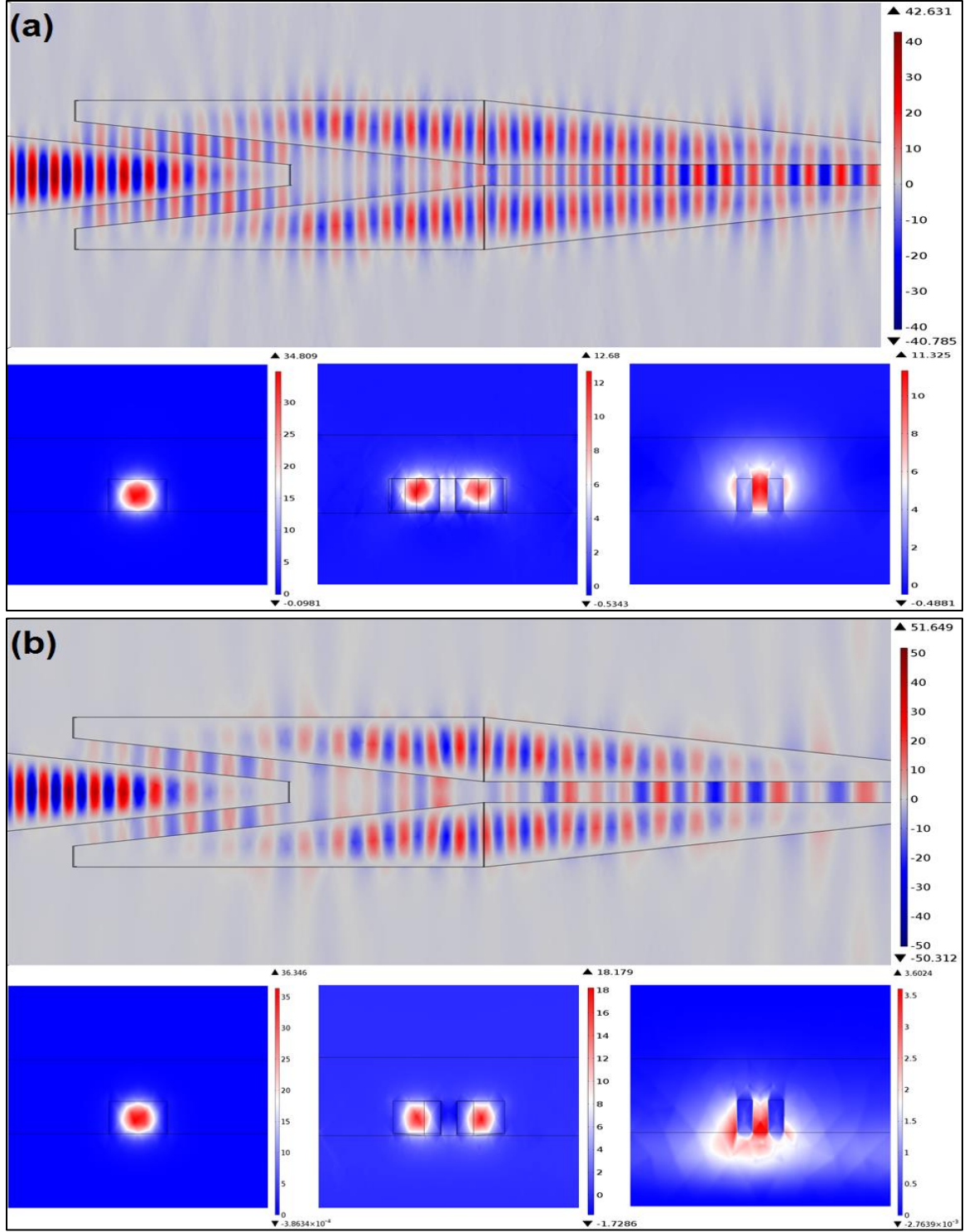


Fig. 4.6 The optical power intensity (W/um²) of quasi-TE mode, at 1550 nm wavelength, through a strip-slot taper coupler between a strip waveguide, 0.45x0.22um², and a slot waveguide, 0.22x(0.12+0.12+0.12) um², in both (a) coated, and (b) uncoated cases.

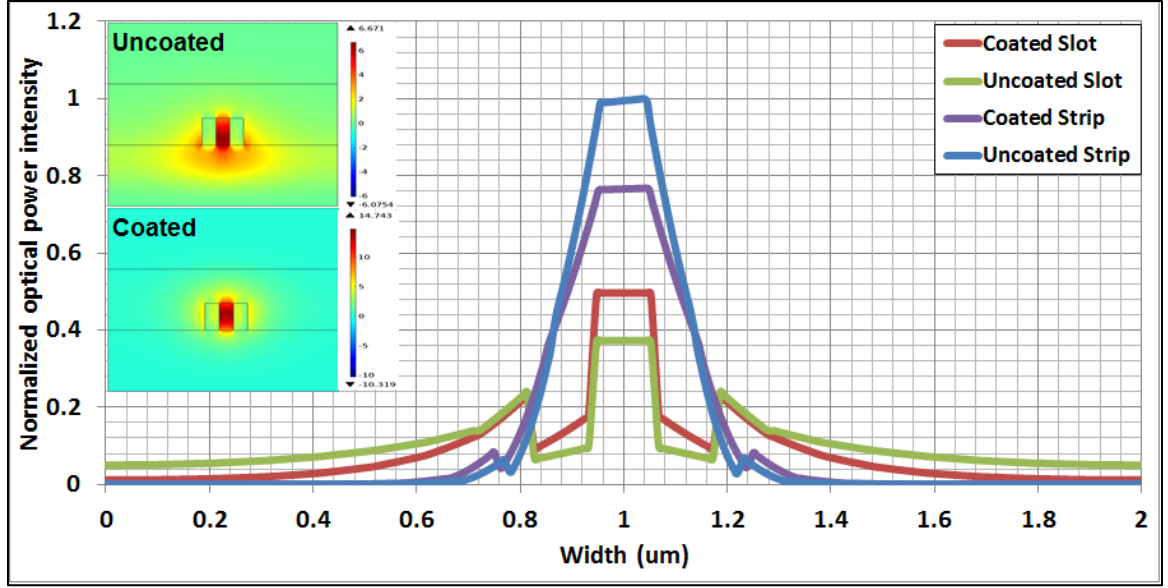


Fig. 4.7 The input and output optical power intensity distribution of the quasi-TE mode at 1550 nm wavelength along the width of (a) coated strip-slot coupler device, and (b) uncoated strip-slot coupler device.

It can be said that increasing the refractive index of the cladding layer, or coating layer, will lead to an increase in the effective index. That takes the propagating mode to oscillate in the guiding region and decrease the dissipated energy through the air or substrate regions. At same time it decreases the ratio of the electric field intensity at the interfaces surface and the electric field intensity over whole structure.

Finally all that can explain why almost the uncoated devices have failed in test, especially those with long slot lengths where they suffer from high scattering loss as well as the high coupling loss.

4.3 Effects of The Slot Width

The width of the slot region, or the low index region between two high index regions, has clear effect on the transmission of the slot device as a result of its effect on the scattering and coupling losses. Experimentally slot devices with three different slot widths, $w_s = 0.13, 0.2, 0.25 \mu\text{m}$ were tested. The transmission spectra of these devices have been compared with the transmission spectrum of a ridge waveguide for de-embedding issues, as stated in Chapter Three. Figure 4.8 shows the measured output optical power of three slot devices with three different slot widths and the transmission of a ridge waveguide over 100 nm spectral width (from 1500 nm to 1600 nm).

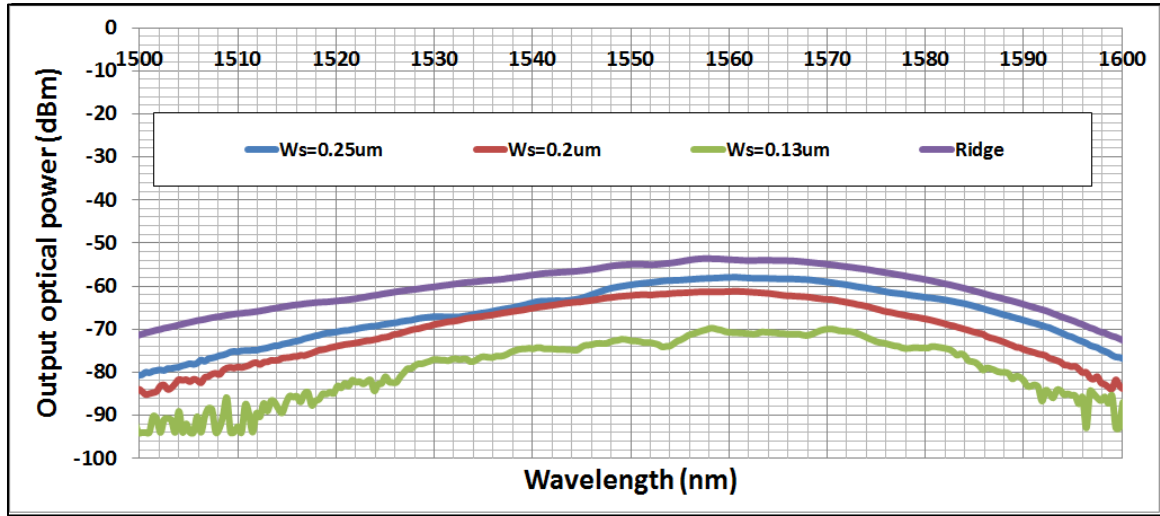


Fig. 4.8 The measured output optical power of slot devices with different slot width, $w_s = 0.13, 0.2, \text{ and } 0.25 \mu\text{m}$, with Si rib width, $w_r = 0.2 \mu\text{m}$, slot length $L_s = 1868 \mu\text{m}$ and taper length, $L_T = 5 \mu\text{m}$, all slots are coated with 500 nm thickness of polymer ($n = 1.7$). Also the measured output optical power of ridge waveguide $0.45 \times 0.22 \mu\text{m}^2$ and 1868 μm length.

It can be seen that the transmission is increased, over the given spectral width, when the slot width is increased from 0.13 μm to 0.2 μm whereas it is very close between 0.2 and 0.25 μm slot width. So it's expected that this increasing in slot width reflects on the propagation and coupling losses.

Theoretically, and as in previous section (3.2), the scattering and coupling losses were calculated by Eqs. (2-62, 63, and 68) with simulation assisting in mode solving. Figure 4.9 shows the measured de-embedded transmission of the three slot devices with the calculated scattering and coupling losses of the simulation of these devices.

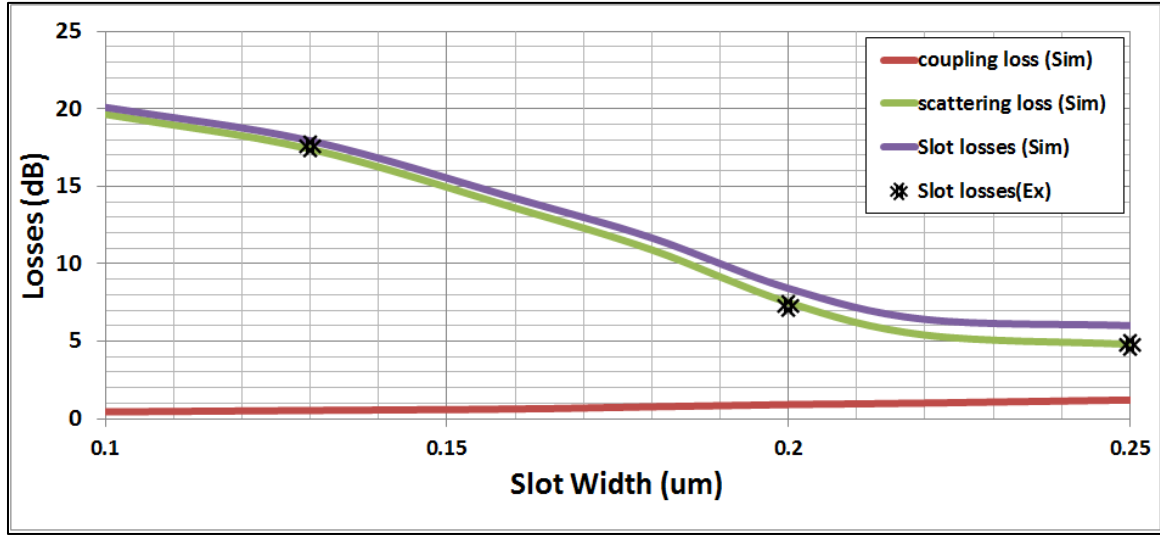


Fig. 4.9 The measured de-embedded losses of the three slot devices in (4.8) and the simulated losses of these devices, which include; coupling loss and scattering loss, at 1550 nm wavelength.

It can be noticed that the total losses is decreased when the slot width is increased. In fact, the influence of the slot width almost appears in the scattering loss clearly more than the coupling loss, especially when it is changed from very tight widths (less than 0.1 um) up to 0.2um. The coupling loss varies very slow with the slot width and it is kept less than 1 dB for the three different slot widths. For more clearance, Table 4.2 shows the variation in the losses values when the slot width is changed in three values. Again these values under operation wavelength 1550 nm, quasi-TE polarization, 0.2um rib width, and 1854 um as slot length.

Table 4.2 The measured de-embedded loss and simulated coupling and scattering loss of the three slot devices in Fig. 4.9 with different slot width, at 1550 nm wavelength

Slot Width (um)	Measured Loss (dB)	Simulated Coupling loss (dB)	Calculated Scattering Loss (dB)
0.13	17.58±0.05	0.54	17.4
0.2	7.25±0.05	0.915	7.4
0.25	4.8±0.05	1.2	5.12

So for scattering loss, the parameter that has been effected by the slot width and effects on the scattering loss is the effective index. Figure 4.10 shows how the effective index of the fundamental mode is decreased when the slot width becomes more wider.

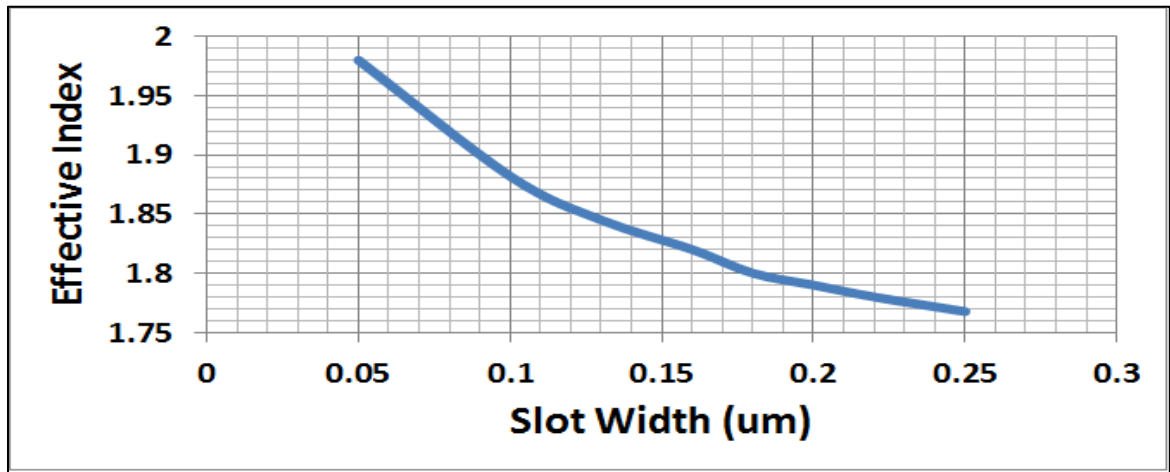


Fig. 4.10 The effective index of the quasi-TE fundamental mode vs. the slot width with Si rib width, $w_r=0.2\mu\text{m}$ at 1550 nm wavelength.

Mathematically and according to Eq. (2-62), it looks that any increasing in the effective index will decrease the scattering loss. But numerically the effective index changes very slightly so its mathematical influence on Eq. (2-62) is very low.

This slow variation of the effective index has clear effect on the strength of the electric field intensity inside the slot. So increase the effective index with decreasing the slot width and constant ribs width leads to increase the normalized electric field intensity at the interfaces walls, as shown in Fig. 4.11 a and b, then increase the scattering loss.

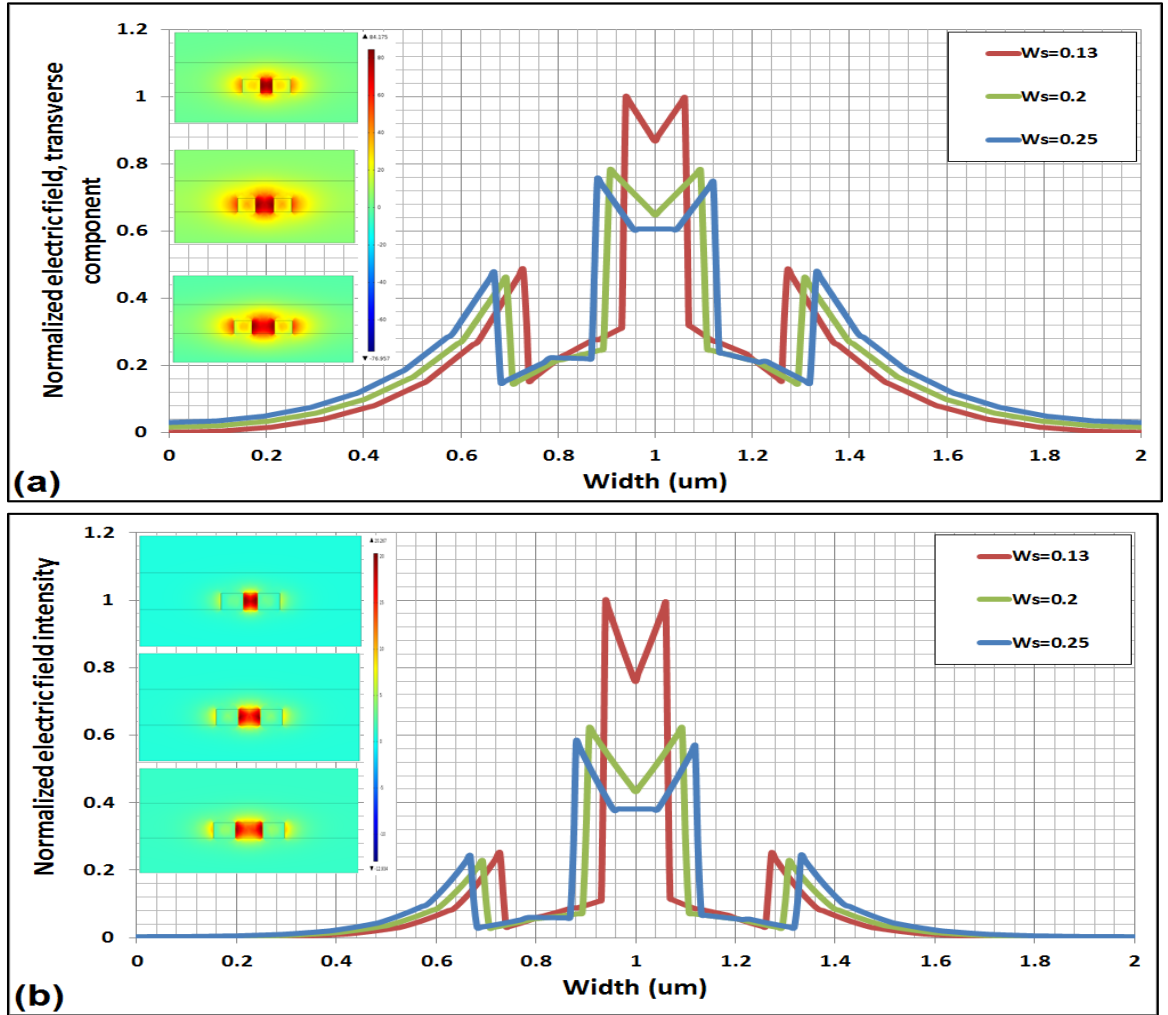


Fig. 4.11 (a) Electric field, transverse-component of the TE-quasi mode across coated slot waveguide with three different slot width, $w_s=0.13$ (red), 0.2(green), and 0.25 um(blue), rib width $w_r=0.2$ um and (b) intensity profiles.

On the other hand, the magnetic field normal component which is parallel with the waveguide sidewalls varies very slot across the whole section. Decreasing the slot width with constant ribs width will increase the effective index of the fundamental guided mode in the slot to be more close to the refractive index of the ribs. So the magnetic field which is continuous between the slot and ribs will be very close in these regions. While increasing the slot width will increase the ratio between the magnetic fields in slot and ribs regions where it will be decreased in the slot compare to ribs, as shown in Fig. 4.12 a. This variation of the normal component of the magnetic field with the slot and the increasing of the electric field transverse component inside the slot with tight widths and keeping it constant inside ribs lead to very close coupled intensities at different slot widths with slight increasing at the tight widths as shown in Fig. 4.12 b.

For more explanation, Fig. 4.13 shows the optical intensity across the strip-slot taper couplers in three slot widths, 0.13, 0.2, and 0.25 μm .

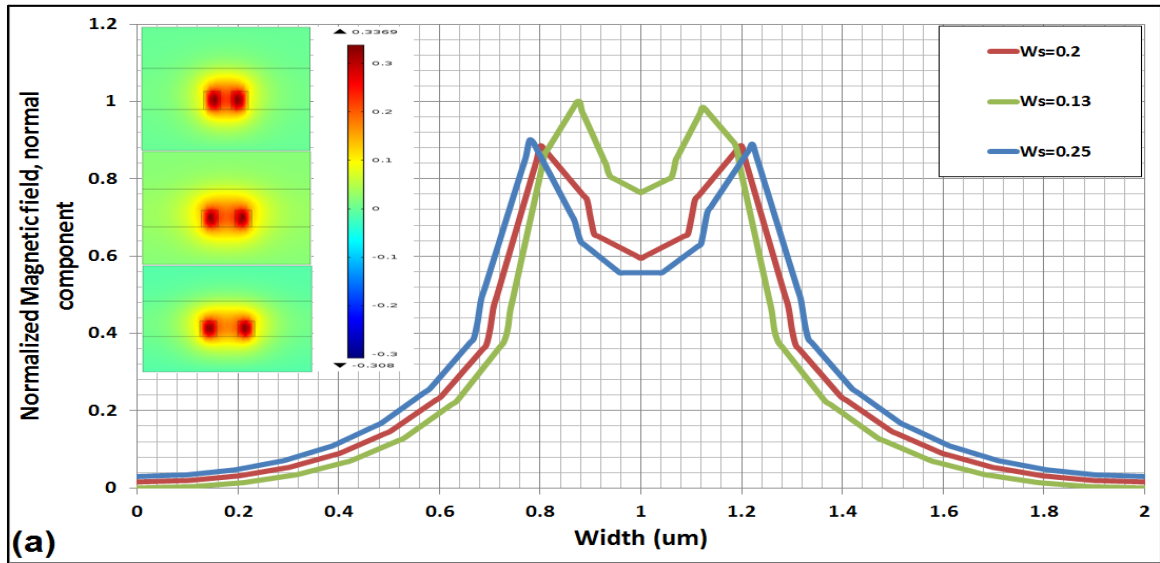


Fig.4.12 to be continued

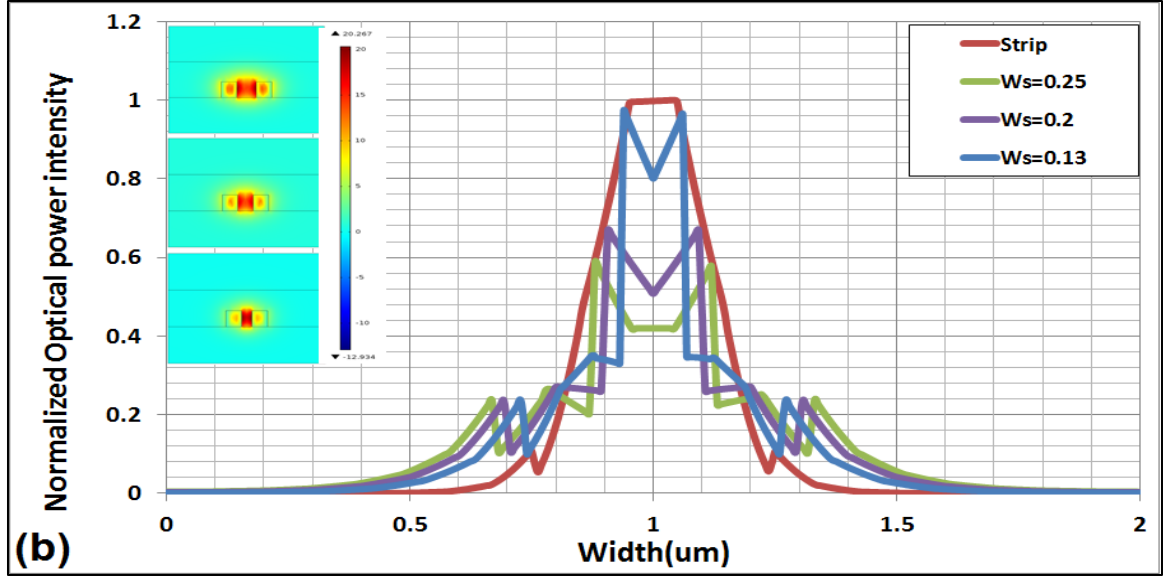


Fig. 4.12 (a) Magnetic field, normal-component, and (b) intensity profiles. of the TE-quasi mode across coated slot waveguide with three different slot width, $w_s=0.13$ (red), 0.2(green), and 0.25 μm (blue), rib width $w_r=0.2 \mu\text{m}$

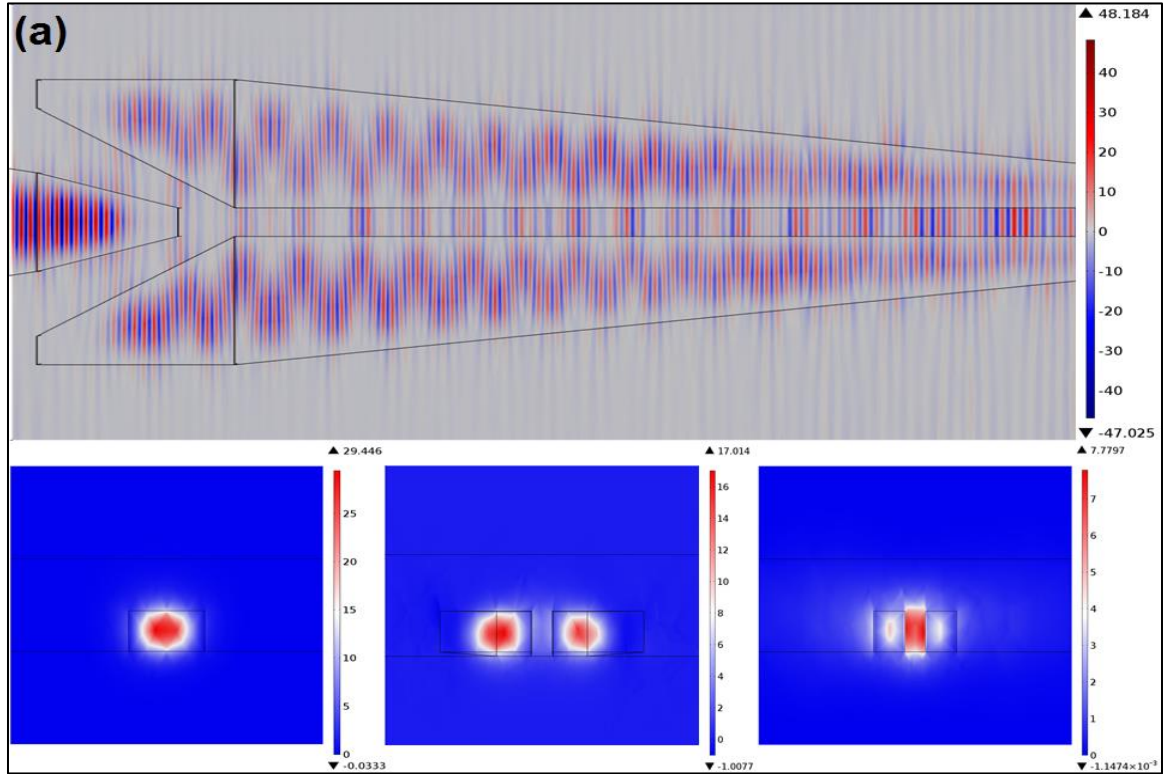


Fig. 4.13 to be continued

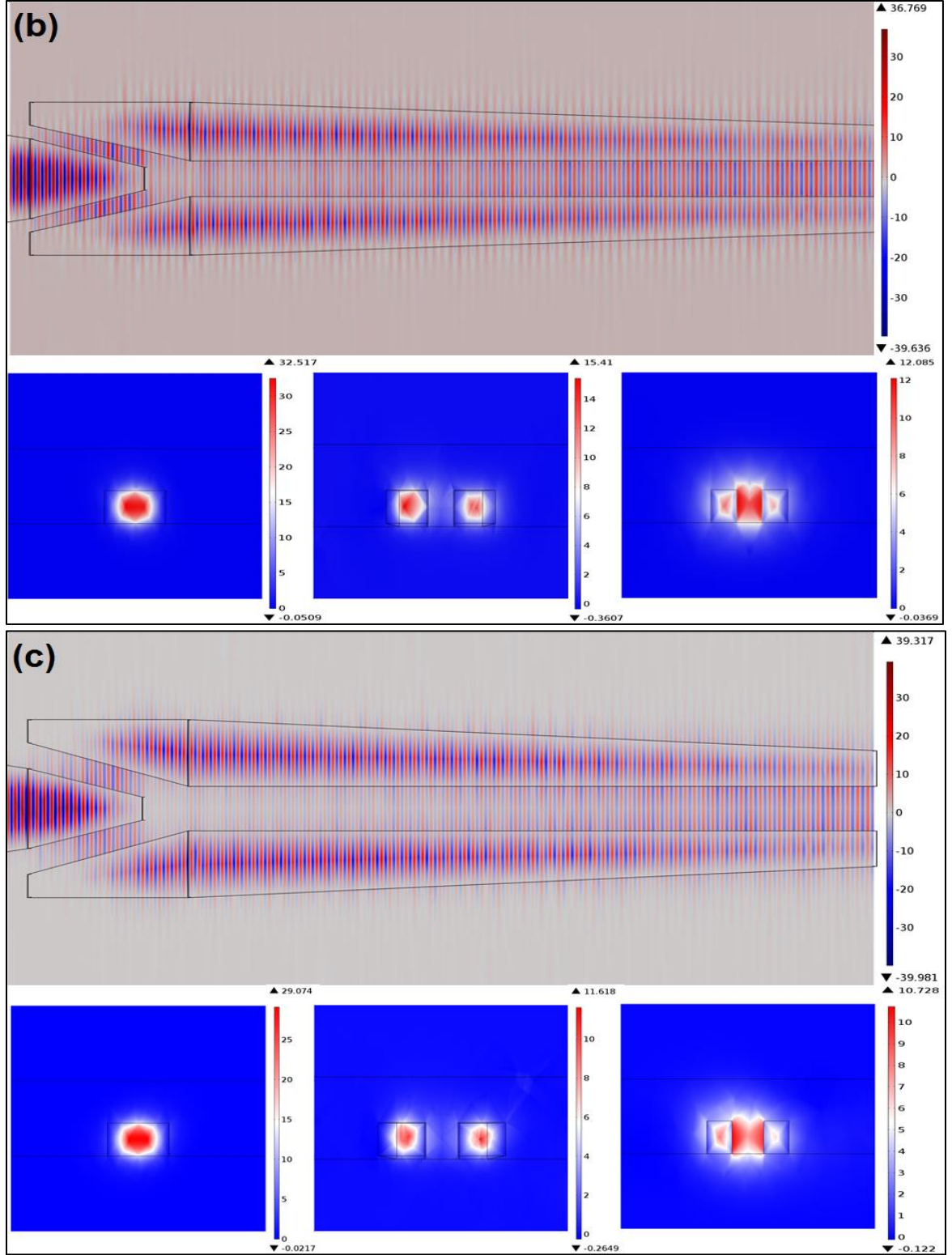


Fig. 4.13 The simulated strip-slot coupler structures with different slot width, w_s ; a) 0.25 μm , b) 0.2 μm , and c) 0.13 μm with Si rib width, $w_r = 0.2 \mu\text{m}$ and taper length $L_T = 5 \mu\text{m}$, at 1550 nm wavelength and TE-polarization.

It's clear now, that the variation of the slot width, with constant ribs width, manages the transmission of slot devices via the scattering loss more than the coupling loss. According to experimental measurements, the minimum slot width that had a response was 0.13 μm , with 0.2 μm ribs width and 2414 μm slot length. The output power of this coated device was 75 ± 5 dBm over 60 nm spectral width (1520-1580 nm). All the devices with same characteristics and longer than this, failed in the test.

4.4 Effects of Si Ribs Width

The variation of the width of the Si rib, with constant slot width, plays an important role by controlling the effective index of the fundamental guided mode. This relation between the effective index and the width of Si rib makes the last the main parameter that controls the distribution of the energy across the whole waveguide, or what is called "Confinement factor", Eq.(2-52). Figure 4.14 shows the effective index of the fundamental guided mode in slot devices with different slot widths as a function of Si ribs width. So with constant slot width, when the rib width is very narrow the effective index of the fundamental mode will be less than the refractive index of the slot. That makes light propagate out the waveguide structure and results in high coupling loss. When this narrow ribs width starts increase, with constant slot width, the effective index is increased to be close to the refractive index of the slot. At this range of increasing of the effective index light tries to be more guided in the slot and propagates at the center of the slot region. Here there is an optimum width for the rib to get more close effective index to the slot region refractive index.

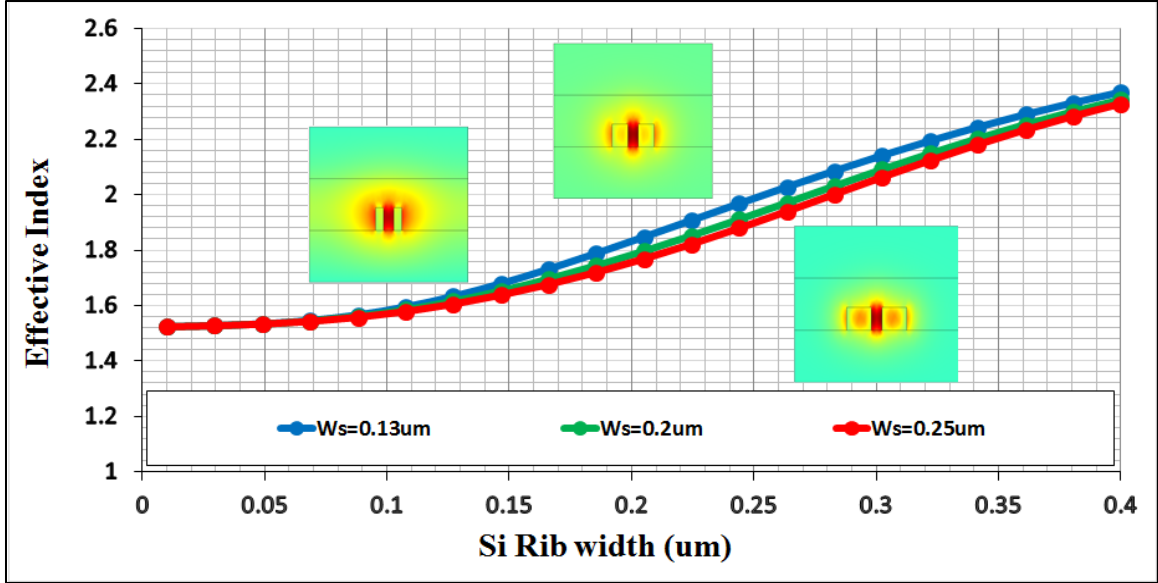


Fig. 4.14 Effective Index vs. Si rib width for three different slot width; 0.13, 0.2, and 0.25 um. Electric field profile for quasi-TE mode at 1550 wavelength for three different rib width; 0.1, 0.2, and 0.3 um and slot width 0.13 um.

When ribs width continues with increasing, the effective index goes away from the slot toward the ribs refractive index. This shifting in the effective index means that light will travel close to the interfaces between slot and ribs. With increasing the electric field intensity at the interfaces walls, the scattering interface loss via the surface roughness will be increased.

It can be seen that the variation of the effective index with the Si rib width is more than its variation with slot width, so the rib has very clear effect on the transmission of the slot device. Figure 4.15 shows the measured output optical power of slot devices with a certain slot width and different ribs widths.

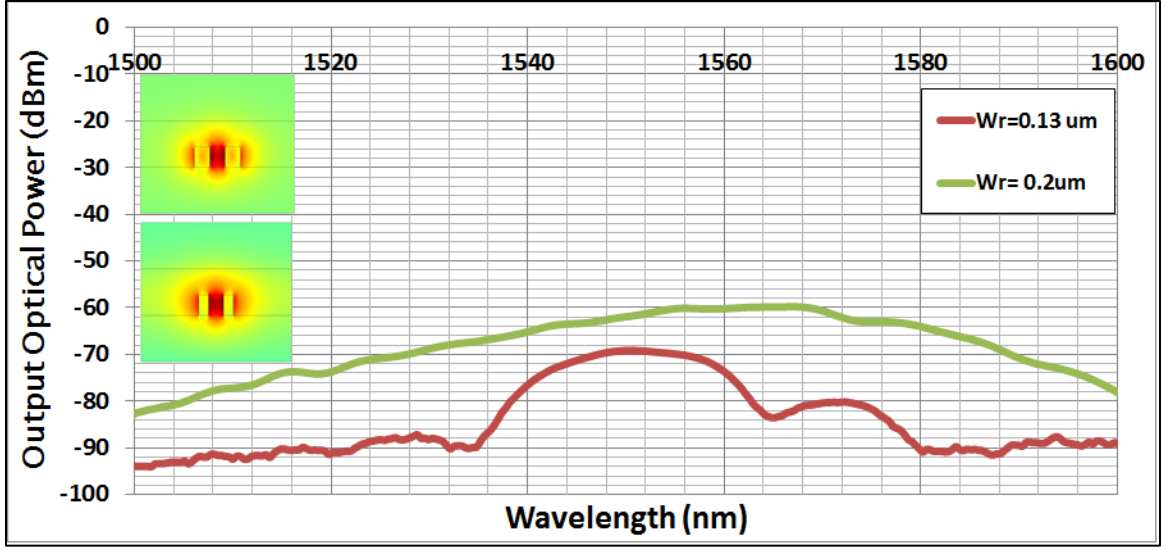


Fig. 4.15 The measured output optical power of two coated slot devices with different rib widths; $w_r = 0.2 \mu\text{m}$ (green), and $0.13 \mu\text{m}$ (red), slot width $w_s = 0.2 \mu\text{m}$, slot length $L_s = 1854 \mu\text{m}$, and height $h = 0.22 \mu\text{m}$.

Figure 4.16 shows the confinement factors, according to Eqs.(2-54, 56, and 58), versus the width of rib. It is clear from in this plot that the confinement factor, which represents the ration between the power across the slot to the power across the whole structure, is increased the rib width as long as it's still smaller than $0.2 \mu\text{m}$. Also, along this range of rib widths, the confinement factor is increased slightly by increasing the slot width. This is exactly required when the slot device is used as a functional device depends on how much power inside the slot like; electro-optic or all optical modulators, and optical switch. Beyond $0.2 \mu\text{m}$ rib width, the confinement factor will be decreased as a result of the decrease of the energy in the slot and increase in the ribs.

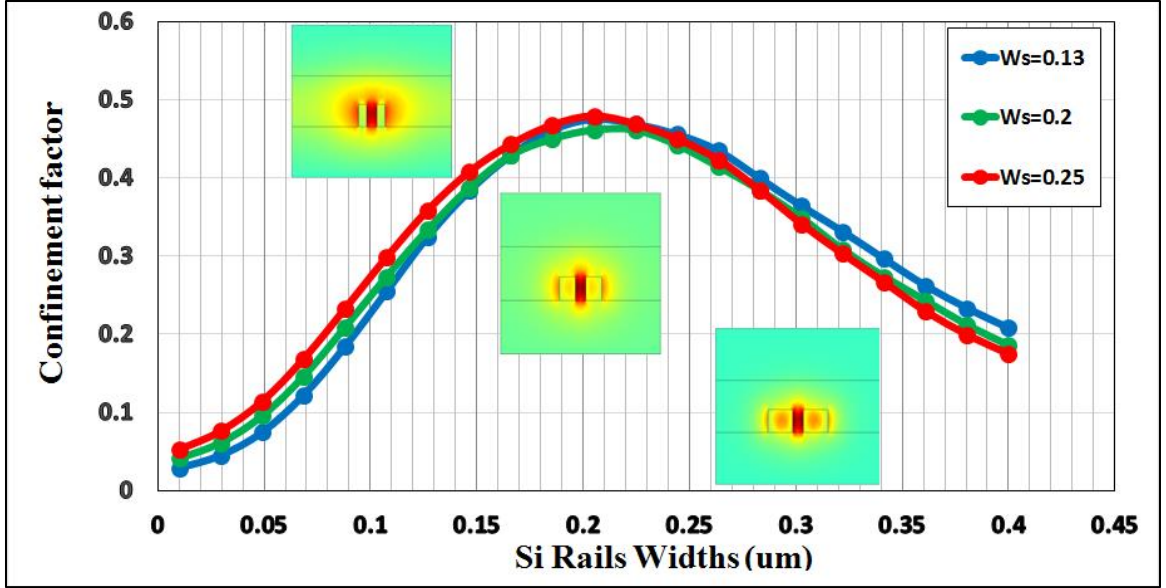


Fig 4.16 The confinement factor vs. Si rib width for three different slot width; 0.13, 0.2, and 0.25 um. Electric field profile for quasi-TE mode at 1550 wavelength for three different rib width; 0.1, 0.2, and 0.3 um and slot width 0.13 um.

4.5 Effects of Taper Length

Basically, the length of the taper coupler effect on the coupling efficiency only at each side of the waveguide. In[26], it's reported that the coupling efficiency of the taper coupler is enhanced by increasing the taper length up to 5 um and keep constant for any length more. This was at operating wavelength 1475 nm. Here, this results are repeated for operating wavelength 1550 nm, and comparing them with measurements of slot devices with different taper length, L_T , as; 5, 10, and 20 um, as shown in Fig 4.17. According to Eqs. (2-66, 67), increase the physical taper length will decrease the taper angle, which depends on the change of the width of taper to change of its length, and that leads to satisfy the condition for achieving an adiabatic taper as shown in Chapter two.

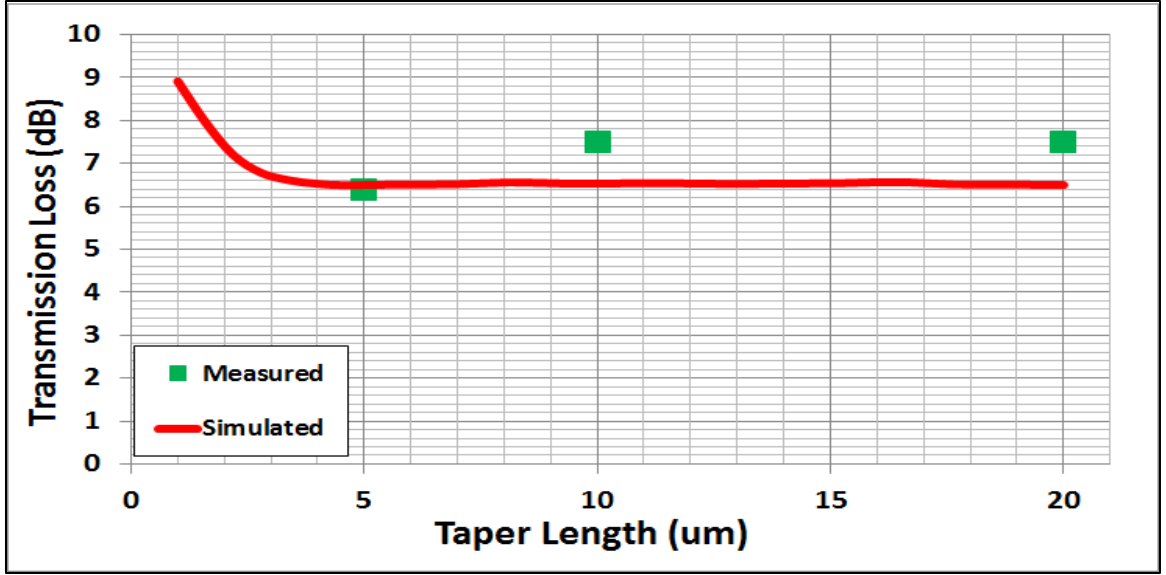


Fig 4.17 The measured and simulated transmission loss of slot devices with three different taper length, L_T ; 5, 10, and 20 μm , and with a slot width, w_s ; 0.2 μm at wavelength 1550 nm and TE-polarization.

4.6 Conclusions

From all the measurements which were done in this work for several slot devices with different specifications, and all the analysis which have been formed depending on the theoretical background, simulation results, and mathematical calculations the following conclusions are deduced;

1. The coupling efficiency of the strip-slot taper coupler is highly depended on the refractive index of the coating layer of the coupling region and slot waveguide where it can be enhanced by several dB(s) according to coating layer and operation wavelength.
2. The scattering loss by the surface roughness of the waveguide sidewalls is the dominated loss in slot waveguide compared with absorption, radiation losses. Scattering loss can be reduced effectively without an improvement in the surface roughness by decrease the

electric field intensity at the sidewalls. This can be achieved primarily by decreasing the index contrast between slot and ribs regions via coating process, and by select the proper slot and rib widths where best performance is noticed when the ratio between the rib width and slot width, w_r/w_s be unity or little bit more

3. The confining light inside the slot, which is measured by confinement factor, is fully depended on the effective index of the guided mode which is mainly controlled by the width of the ribs waveguides. There is an optimum rib waveguides width for specified conditions where there is no confinement below or above it..
4. Most of the uncoated devices have failed in the test where they suffer from high scattering and coupling losses.

4.7 Suggestions for Future Works

This work did deal with a common structure of the slot waveguide and tried to measure and calculate the linear losses of this type of waveguide by using SLED light source, with linear power range and 100 nm spectral width around the 1550 nm as a central wavelength which is more suitable for communication applications. Some suggestions for future works can be expected as;

1. Present a new slot waveguide structure by changing the shape of ribs, shape of slot, or thickness of coating layer attempting to overcome the transmission losses.
2. Measuring and analyzing the response of the slot waveguide with other operation wavelength, 1310 nm is recommended as it more suitable for data communication.

3. Measuring the nonlinear losses of the slot waveguide to study its ability to work as an optical modulator or optical switch.
4. Connecting with no.3, using the slot waveguide to study the nonlinearity of the organic material like polymer by founding χ^3 and measuring the two photon absorption of Si to know its influence on the slot device's performance when it is required as functional device, when can be used as an all optical modulator.

References

- [1] V. J. Sorger, R. F. Oulton, R. Min Ma, and X. Zhang, "Toward integrated plasmonic circuits", *MRS Bulletin*, vol. 37, 2012.
- [2] V. R. Almeida, Q. Xu, C. A. Barrios, and M. Lipson, "Guiding and confining light in void nanostructure", *Optics Letter*, vol. 29, no.11, 2004.
- [3] Q. Xu, V. R. Almeida, R. R. Panepucci, and M. Lipson, "Experimental demonstration of guiding and confining light in nanometer-size low-refractive-index material", *Optics Letter*, vol. 29, no.14, 2005.
- [4] A. Mickelson, "Silicon Photonic Slot Guides For Nonlinear Optics", *International Conference on Microwave and Photonics (ICMAP)*, 2013.
- [5] A. Martinez, J. Blasco, P. Sanchis, J. V. Galan, J. Garcia-Ruperez, E. Jordana, P. Gautier, Y. Lebour, S. Hernandez, R. Spano, R. Guider, N. Daldosso, B. Garrido, J. Fedeli, L. Pavesi, and J. Marti, "Ultrafast All-Optical Switching in a Silicon-Nano crystal-Based Silicon Slot Waveguide at Telecom Wavelengths", *Nano Letter*, vol. 1, no. 10, 2010.
- [6] C. Koos, P. Vorreau, T. Vallaitis, P. Dumon, W. Bogaerts, R. Baets, B. Esembeson, I. Biaggio, T. Michinobu, F. Diederich, W. Freude and J. Leuthold, "All-Optical High-Speed Signal Processing with Silicon–Organic Hybrid Slot Waveguides", *Nature Photonics*, vol.3, no. 25, 2009.
- [7] Y. Li, K. Cui, X. Feng, Y. Huang, F. Liu, and W Zhang, "Ultralow Propagation Loss Slot-Waveguide in High Absorption Active Material", *IEEE Photonic Journal*, vol. 6, no. 3, 2014.
- [8] Z. Wang, N. Zhu, Y. Tang, L. Wosinski, D. Dai, and S. He, "Ultracompact Low-Loss Coupler Between Strip and Slot Waveguides", *Optics Letter*, vol. 34, no. 10, 2009.
- [9] X. Li, X. Feng, K. Cui, F. Liu and Y. Huang, " Designing Low Transmission Loss Silicon Slot Waveguide at Wavelength Band of

High Material Absorption", *Optics Communication*, vol. 5, no. 42, 2013.

- [10] X. Li, X. Feng, X. Xiao, K. Cui, F. Liu, and Y. Huang, "Experimental Demonstration of Silicon Slot Waveguide with Low Transmission Loss at 1064 nm", *Optics Communications*, vol. 4, no. 85, 2014.
- [11] C. K. Kao and D. B. Hockham, "Dielectric-Fiber Surface Waveguides for Optical Frequencies," *Proceedings of the Institution of Electrical Engineers*, vol. 113, no.7, 1966.
- [12] F. P. Felix, D. B. Keck, and R. D. Maurer, "Radiation Losses in Glass Optical Waveguides," *Applied Physics Letters*, vol. 17, no.10, 1970.
- [13] R. Soref and J. P. Lorenzo, "All-Silicon Active and Passive Guided-Wave Components for 1.3 and 1.6 micron," *IEEE Journal of Quantum Electronics*, vol. 22, no. 6, 1987.
- [14] R. Soref and B. Bennett, "Electro-Optical Effects in Silicon," *IEEE Journal of Quantum Electronics*, vol. 23, no.1, 1987.
- [15] R. Soref, "Silicon-Based Optoelectronics," *Proceedings of the IEEE*, vol. 81, no. 12, 1993.
- [16] A. G. Rickman, G. T. Reed, and F. Namavar, "Silicon-on-Insulator optical Rib Waveguide Loss and Mode Characteristics," *Journal of Lightwave Technology*, vol. 12, no. 10, 1994.
- [17] P. D. Trinh, S. Yegnanarayanan, F. Coppinger, and B. Jalali, "Silicon-on-Insulator (SOI) Phased-Array Wavelength Multi/Demultiplexer with Extremely Low-Polarization Sensitivity," *IEEE Photonics Technology Letters*, vol. 9, no. 7, 1997.
- [18] K. K. Lee, D. R. Lim, H.-C. Luan, A. Agrawal, J. Foresi, and L. C. Kimmerling, "Effect of Size and Roughness on Light Transmission in a Si/SiO₂ Waveguide: Experiments and Model", *Applied Physics Letters*, vol. 77, 2000.
- [19] A. Sakai, G. Hara, and T. Baba, "Propagation Characteristics of Ultrahigh-Delta Optical Waveguide on Silicon-on-Insulator

- Substrate”, *Japanese Journal of Applied Physics*, Part 2, vol. 4B, 2001.
- [20] Y. A. Vlasov and S. J. McNab, "Losses in Single-Mode Silicon-on-Insulator Strip Waveguides and Bends", *Optics Letter*, vol. 12, no. 8, 2004.
 - [21] K. K. Lee, D. R. Kim, and L. C. Kimmerling, “Fabrication of Ultralow-Loss Si/SiO Waveguides by Roughness Reduction”, *Optics Letters*, vol. 26, 2001.
 - [22] P. A. Anderson, B. S. Schmidt, and M. Lipson, “High Confinement in Silicon Slot Waveguides with Sharp Bends”, *Optics Express*, vol. 14, no. 20, 2006.
 - [23] M. Sumetsky, “Vertically-Stacked Multi-Ring Resonator,” *Optics Express*, vol. 13, no.17, 2005.
 - [24] L. Liao, A. Liu, J. Basak, H. Nguyen, M. Paniccia, D. Rubin, Y. Chetrit, R. Cohen, and N. Izhaky, “40 Gbit/s Silicon Optical Modulator for High Speed Applications,” *Electronics Letters*, vol. 43, no. 22, 2007.
 - [25] Y. Qian, J. Song, S. Kim, and G. P. Nordin, “Compact 90° Trench-Based Splitter for Silicon-on-Insulator Rib Waveguides,” *Optics Express*, vol. 15, no.25, 2007.
 - [26] Y. Vlasov, W. M. J. Green, and F. Xia, “High-Throughput Silicon Nanophotonic Wavelength-Insensitive Switch for on-Chip Optical Networks,” *Nature Photonics*, vol. 2, no.4, 2008.
 - [27] J. Leuthold, C. Koos, and W. Freude, “Nonlinear silicon photonics,” *Nature Photonics*, vol. 4, no.8, 2010.
 - [28] Q. Deng, L. Liu, X. Li, and Z. Zhou, "Strip-Slot Waveguide Mode Converter Based on Symmetric Multimode Interference", *Optics Letter*, vol. 39, no. 19, 2014.
 - [29] M. Q. Qi, W. Wang, and M. P. Jin, "A Method of Calculating Admittance of Waveguide Slot", *Microwave Conference Proceedings, Asia Pacific Conference Proceedings*, , *IEEE*, vol. 4, p 1-3, 2005.

- [30] J. Blasco and C.A. Barrios, "Compact Slot-Waveguide/Channel-Waveguide Mode-Converter", *Conference on Lasers and Electro-Optics Europe, IEEE*, 2005.
- [31] F. Grillot, L. Vivien, S. Laval, and E. Cassan "Propagation Loss in Single-Mode Ultrasmall Square Silicon-on-Insulator Optical Waveguides", *Journal of Lightwave Technology*, vol. 24, no. 2, 2006.
- [32] R. Sun, P. Dong, N. Feng, C. Hong, J. Michel, M. Lipson, and L. Kimerling, "Horizontal Single and Multiple Slot Waveguides: Optical Transmission at $\lambda = 1550$ nm", *Optics Letter*, vol. 15, no. 26, 2007.
- [33] Y. Fu , Y. Riley , Shin , and Fauchet, "Theoretical and Experimental Demonstration of Light Confinement in a Multi-Slot Waveguide", *4th IEEE International Conference on Group IV Photonics*, 2007.
- [34] L. Yan, X. Jun, C. Wu, and Y. Zhong, " Modelling and Analysis of Modal Behaviour in SOI Slot Waveguides", *CHIN.PHYS.LETT.*, vol. 25, no. 8, 2008.
- [35] R. Ding, T. Jones, W. Kim, X. Xiong, R. Bojko, J. Fedeli, M. Fournier, and M. Hochberg, "Low-Loss Strip-Loaded Slot Waveguides in Silicon-on-Insulator", *Optics Letter*, vol. 18, no. 24, 2013.
- [36] A. Chen, H. Sun, A. Szep, S. Shi, D. Prather, Z. Lin, R. S. Kim, and D. Abeysinghe, "Achieving Higher Modulation Efficiency in Electro-Optic Polymer Modulator With Slotted Silicon Waveguide", *Journal of Lightwave Technology*, vol. 29, no. 21, 2011.
- [37] R. Palmer, L. Alloatti, D. Korn, W. Heni, P. C. Schindler, J. Bolten, M.Karl, M. Waldow, T. Wahlbrink, W. Freude, C. Koos, and J. Leuthold, "Low-Loss Silicon Strip-to-Slot Mode Converters", *IEEE Photonics Journal*, vol. 5, no.1, 2013.

- [38] Y. Xu, J. Wang, J. Xiao, and X. Sun, "Design of a Compact Silicon-Based Slot–Waveguide Crossing", *Applied Optics*, vol. 52, no. 16, 2013.
- [39] F. Li, X. Hu, J. Wu, L. Zhou, and Y. Su, "Ultra-Compact and Broadband Orthogonal Coupler Between Strip and Slot Silicon Waveguides", *SPIE-OSA-IEEE*, vol. 8307, 2011.
- [40] J. M. Liu, *Photonic Devices*, Cambridge University Press, New York, 2005.
- [41] W. H. Hayt Jr. and J. A. Buck, *Engineering Electromagnetics*, 8th edition, McGraw-Hill, New Yourk, 2006.
- [42] D. Griffiths, *Introduction to Electrodynamics*, 3rd edition, Prentice Hall, 1999.
- [43] D. Cook, *The Theory of The Electromagnetic Field*. Mineola NY: Courier Dover Publications, 2002.
- [44] B.E.A Saleh and M. C. Teich, *Fundamentals of Photonics*, 2nd edition, Wiley Series in Pure and Applied Optics, 2007.
- [45] R. G. Hunsperger, *Integrated Optics Theory and Technology*, 6th edition, Springer, 2006.
- [46] K. Kawano and T. Kitoh, *Introduction to Optical Waveguides Analysis*, John Wiley and Sons, 2001.
- [47] R.Soref, "The Past, Present and Future of Silicon Photonics", *IEEE Journal Of Selected Topics In Quantum Electronics*, vol. 12, no. 6, 2006.
- [48] G. T. Reed and A. P. Knights, *Silicon Photonics An Introduction*, John Wiley and Sons, 2004.
- [49] M. Jamal Deen and P. K. Pasu, *Silicon Photonics Fundamentals and Devices*, John Wiley and Sons, 2012.
- [50] M. Hiltunen, *Polymeric Slot Waveguide Interferometers*, PhD thesis, *University of Oulu*, 2014.

- [51] M. Yagnyukova, *Modeling, Fabrication, and Characterization of a Bragg Slot Waveguide with a Cavity*, Master thesis, University of Toronto, 2013.
- [52] P. Muller, *Fundamental Characteristics of The SOI Slot Waveguide Structure*, PhD thesis, University of Wien, 2010.
- [53] F.P. Payne, and J.P.R. Lacey, "A theoretical analysis of scattering loss from planar optical waveguides". *Opt. Quant. Electron.*, 1994.
- [54] F. Ladouceur, J. Love, and T. Senden, "Effect of sidewall roughness in buried channel waveguides.", *IEEE Proc. J.*, 1994.
- [55] P. K. Tien, " *Light Waves in Thin Films and Integrated Optics*", *APPLIED OPTICS*, vol. 10, no. 11, 1973.
- [56] T. S. Moss, G. J. Burrell and B. Ellis, *Semiconductor Optoelectronics*, Butterworth, London, 1973.
- [57] L. Vivien and L. Pavesi, *Handbook of Silicon Photonics*, CRC Press, 2013.
- [58] D. Taillaert, P. Bienstman, and R. Baets, "Compact Efficient Broadband Grating Coupler for Silicon-on-Insulator Waveguides," *Optics Letters*, vol. 29, no. 23, 2004.
- [59] A. Mekis, "A Grating-Coupler-Enabled CMOS Photonics Platform," *Selected Topics in Quantum Electronics*, no. 99, 2010.
- [60] S. Scheerlinck, J. Schrauwen, F. Van Laere, D. Taillaert, D. Van Thourhout, and R. Baets, "Efficient, Broadband and Compact Metal Grating Couplers for Silicon-on-Insulator Waveguides," *Optics Express*, vol. 15, no. 15, 2007.
- [61] R. Halir, P. Cheben, S. Janz, D.X. Xu, . Molina-Fernandez, and J. G. Wangüemert-Pérez, "Waveguide Grating Coupler with Subwavelength Microstructures," *Optics Letters*, vol. 34, no. 9, 2009.
- [62] R. Halir, "Continuously Anodized Fiber-to-Chip Surface Grating Coupler with Refractive Index Engineered Subwavelength Structure," *Optics Letters*, vol. 35, no. 19, 2010.

- [63] F.J. Love, "Application of Low Loss Criterion to Optical Waveguides and Devices.", *IEE Proc. J.*, 1989.
- [64] V.R. Almeida, "Nano Taper for Compact Mode Conversion.", *Optics Letter*, 2003.
- [65] A.K. Ghatak, and K. Thyagarajan, *Optical Electronics*, Cambridge University Press, Cambridge, UK, 1989.
- [66] <http://www.photond.com/products/fimmwave>.
- [67] A. Khanna, A. Säynätjoki, A. Tervonen and S. Honkanen, "Control of Optical Mode Properties in Cross-Slot Waveguides", *Applied Optics*, vol. 48, no.34, 2009.
- [68] M.P. Hiscocks, C. Su, B. Gibson, A.D. Greentree, L.C.L. Hollenberg, and F. Ladouceur, "Slot-Waveguide Cavities for Optical Quantum Information Applications", *Optics Express*, vol. 17, no. 9, 2009.

Publications

1. M. Salih, X. Chen, E. Jacobson, K. Janani, S. Gautam , and A. Mickelson, "Practice and Theory in Silicon-on-Insulator Slot Waveguide", IEEE Photonics Conference (IPC2014), 2014. **Contributed.**
2. M. Salih, M. Elias, X. Chen, E. Jacobson, K. Janani, S. Gautam , and A. Mickelson, "Losses in Slot Devices", Applied Optics, 2015. **To be submitted for publication**

الخلاصة

يعتبر موجه الموجة ذو الفتحة احد التركيبات السليكون فوتونيك المثيرة للاهتمام. حيث يعمل هذا المكون على حصر وتوجيه الضوء في فجوة ضيقة جداً من المواد ذات المعامل الانكسار القليل بالاعتماد على مبدأ الانعكاس الداخلي الكلي.

في هذا العمل مصفوفة من 200 جهاز موجه موجة ذو فتحة، نوع سيليكون على عازل، بأبعاد (عرض الفتحة، عرض الشرائط، طول الجهاز وطول الجزء الخاص بالاقتران) متفاوتة صُنعت على خلية من رقاقة مصنوعة تجارياً. هذه الخلايا شُطرت الى رقاقات اصغر منفردة بعد التصنيع. بعض هذه الرقائق الصغيرة صُقلت بطبقة رقيقة جداً من البوليمرات حيث تسَلَّلت الى الفتحات بشكل كامل. القياسات التي تضمنت الخسائر الطيفية أُنجزت باستخدام اجهزة موجه الموجة بين مقرنات مشبكة لكل من الرقائق المصقولة والغير مصقولة. خسائر الادراج في بعض الاجهزة الفردية تفاوتت من بعض الديسبلات الى قيم عالية جداً حيث كانت استجابتها اقل حتى من مستوى الضوضاء في محلل الطيف البصري المستخدم في القياس كمستقبل نهائي. كانت الرقائق التي فشلت في اختبار النقل منها غير المصقول في المقام الأول. اسمايا الأجهزة المتطابقة حول رقائق مختلفة أظهرت سلوكاً متطابقاً اسمياً. برنامج الكتروني تجاري استخدم لمحاكاة كل هيكل ضمن اختبار ال 200 جهاز، لوحظ ان هذه المحاكاة تتفق بشكل جيد نوعياً مع النتائج التجريبية حيث اظهرت توافقاً نوعياً لآبأس به. المقارنة بين التجربة والمحاكاة تشير الى ان الخسائر الكامنة في جهاز موجه الموجة ذو الفتحة ضعيفة جداً. كذلك خسائر الاقتران كانت قليلة جداً في حالة الاجهزة المطلية، لكن الامر يختلف بالنسبة للأجهزة بدون طلاء حيث الكثير من الطاقة تُبدد الى طبقة الركيزة. استخدام نموذج السطح الخشن يشير الى ان الخسائر الزائدة التي من الممكن ان تظهر في الفتحات اكثر من الشرائط تنشأ من تبعثر الطاقة عند السطوح بسبب خشونتها فقط. الخسائر الزائدة في حالة الموجه ذو الفتحة تنشأ من كثافة الطاقة الكهرومغناطيسية العالية على سطوح الموجه نتيجة لمبدأ

عدم استمرارية المجال الكهربائي والذي يوظف كميكانيكية توجيهه في هذا النوع من الموجات مقارنة مع نظيراتها من موجات متسلسلة تعتدت على التوجيه المعاملي. الاستنتاجات تشمل بعض التكهفات بإمكانية تحديد هذه الخسائر من خلال التباين في تصميم هذه الاجهزة دون تحسين خشونة السطح التي هي عليه من المنشأ.



وزارة التعليم العالي والبحث العلمي
جامعة بغداد
معهد الليزر للدراسات العليا

قياس وتحليل الخسائر لموجهات الموجة ذوات الفتحة المصنعة من سليكون على عازل

رسالة مقدمة إلى
معهد الليزر للدراسات العليا
جامعة بغداد
لاستكمال متطلبات نيل درجة
دكتوراه فلسفة في الليزر/ الهندسة الالكترونية والاتصالات

من قبل

ميثم نعيم صالح

بكالوريوس هندسة الليزر والالكترونيات البصرية 2005
ماجستير هندسة الليزر والالكترونيات البصرية 2009

بإشراف
أ.د. مازن مانويل ألياس